UNIVERSITY OF CALIFORNIA
SANTA CRUZ

UNDERSTANDING *KEPLER*'S SUPER-EARTHS AND SUB-NEPTUNES: INSIGHTS FROM THERMAL EVOLUTION AND PHOTO-EVAPORATION

A dissertation submitted in partial satisfaction of the
requirements for the degree of

Doctor of Philosophy

in

ASTRONOMY & ASTROPHYSICS

by

Eric David Lopez

June 2014

The Dissertation of Eric David Lopez
is approved:

Professor Jonathan Fortney, Chair

Professor Gregory Laughlin

NASA Scientist Kevin Zahnle

Dean Tyrus Miller
Vice Provost and Dean of Graduate Studies

Table of Contents

List of Figures

List of Tables

Abstract

Understanding *Kepler*'s Super-Earths and Sub-Neptunes: Insights from Thermal Evolution and Photo-Evaporation

by

Eric David Lopez

Extrasolar planet surveys have identified an abundant new population of highly irradiated planets with sizes that are in between that of the Earth and Neptune. Such planets are unlike anything found in our own Solar System, and many of their basic properties are not understood. As such, these planets provide a fundamental test for models of planets formation and evolution with important implications for the formation of the Earth and planet habitability.

In order to understand these new classes of planets, we have developed planetary structure and evolution models that can be used both to answer questions about individual planetary systems and to study populations of planets as a whole. In brief, these models allow us to follow a planet's mass, size, internal structure, and composition as it ages; from the time it finishes formation until it is detected billions of years later.

These evolution models are critical because a planet's composition can change substantially over its lifetime. Close-in planets, like most of those found so far, are bombarded by large amounts of ionizing radiation, which over time can completely strip away a planet's atmosphere; even turning a gas-rich Neptune sized planet into a barren rocky super-Earth.

Using these models, we explore the structure, composition, and evolution of sub-Neptune sized extrasolar planets found by NASA's *Kepler* mission. We examine the relation-

ships between planetary masses, radii, and compositions. We show how these compositions have been sculpted by photo-evaporation, and we examine the interplay between thermal and evaporative evolution.

To my mother and sister,

without their support this

would never have been possible.

Acknowledgments

I must begin by acknowledging the unwavering support of my thesis advisor Jonathan Fortney. I cannot possibly imagine a better advisor than Jonathan, who has been both a mentor and a friend over the last five years. His top priority is the success and well-being of his students. Throughout my graduate career Jonathan has opened doors to new opportunities, advocated and promoted my work, and provided an endless supply of encouragement and patience.

I would also like to thank my thesis committee members Greg Laughlin and Kevin Zahnle. Greg was one of the first people to encourage me to pursue research in exoplanets. Kevin has been an invaluable resource in attempting to understand atmospheric evaporation. Over the years Kevin has taught me a great deal, providing physical insight and jokes in equal measure.

Likewise, I would like to thank my many colleagues and collaborators including, but certainly not limited to, Tom Barclay, Daniel Fabrycky, Daniel Huber, Daniel Jontof-Hutter, Brian Jackson, Lisa Kaltenegger, Eliza Kempton, Doug Lin, Jack Lissauer, Rodrigo Luger, Geoff Marcy, Nadine Nettelmann, James Owen, Leslie Rogers, Megan Shabram, Lauren Weiss, Angie Wolfgang for many helpful and thought provoking conversations. I am proud to have collaborated with many of these people and I am proud to have known all of them. I am especially grateful to Jack Lissauer for bringing me into the *Kepler* scientific community and for helping me to participate in some of it's most exciting discoveries.

To paraphrase a well-known proverb, "it takes a village to complete a dissertation", and I would like to thank everyone who helped, encouraged, and inspired me to pursue a career

in academia. In particular, two people come to mind. First, I would like to thank my high school teacher and mentor Frank Panazich who first taught me what it meant to be a researcher. Second, I would like to thank Geoffrey Marcy for nearly a decade of support and encouragement. I first met Geoff as an undergraduate at UC Berkeley in his introduction to astronomy course. Geoff's boundless enthusiasm and encouragement helped convince me that I could succeed in astronomy and that I should apply to graduate school. Over the years he has continuously promoted my career and provided countless letters of recommendation.

I am fortunate to have spent my time at Santa Cruz surrounded by brilliant and amazing friends and colleagues. Over the years my fellow graduate students have become an extended family and I cannot imagine my time here without them. I'd especially like to thank Justin Brown, Jenn Burt, Judy Cheng, Edmond Cheung, Claire Dorman, Jerome Fang, Jenny Graves, Katie Hamren, Anne Medling, Neil Miller, Caroline Morley, Mark Mozena, Rosalie McGurk, and Angie Wolfgang. In particular, I would like to thank my friend and office mate Caroline Morley for years of friendship and for proofreading above and beyond the call of duty.

Above all though, I would like to thank my mother, father, and sister, who always believed in me. I am especially grateful to my mother; from the time I could speak she went out of her way to satisfy my endless curiosity and encourage my interest in science. Visiting museums and observatories with my mother are among my earliest and happiest memories. She fought and sacrificed to provide me with the best education possible and without her support this thesis could never have been written.

Finally, I would like to thank coffee for existing and the baristas at Lulu Carpenter's for serving it while providing the space where most of this work was written. Also, I would

like to thank Seabright Brewery and my fellow pint-nighters for providing me a small amount of sanity and large amount of friendship. Lastly, I would like to thank the people of Scotland for helping provide me with the next step in my life at the University of Edinburgh and for inventing scotch to celebrate that step with.

The author of this thesis was supported by the Eugene Cote-Robles fellowship and the Chancellor's Dissertation Year fellowship along with NASA grant NNX09AC22G and NSF grant AST-1010017.

Chapter 1

Introduction

Astronomy is currently in the midst of a revolution. For thousands of years philosophers and writers have speculated about the possibility of distant worlds orbiting other stars; and yet just twenty-five years ago, science did not know of a single planet outside of the Solar System. Since the first few discoveries, we have now found almost 1500 confirmed extrasolar planets (Wright *et al.*, 2011). Now we know that planets are ubiquitous and there may be as many planets as there are stars in our galaxy (Cassan *et al.*, 2012; Swift *et al.*, 2013).

In particular, NASA's *Kepler* mission has discovered almost a thousand extrasolar planets and over 3,800 planet candidates to date. In just the last five years, the *Kepler* mission discovered the first rocky extrasolar planet (Batalha *et al.*, 2011), the first potentially habitable extrasolar planet (Borucki *et al.*, 2013), the first sub-Mercury sized planet (Barclay *et al.*, 2013), and the first circumbinary planet (Doyle *et al.*, 2011). Figure 1.1, shows the radii and semi-major axes of all confirmed planets, color-coded by the date of their discovery. This highlights the enormous contribution made by the *Kepler* mission; more than half of the known planets,

and nearly all those smaller than Neptune have been found by *Kepler*.

For the first time we have a robust determination of the relative abundance of different sizes of planets stretching from Earth sized all the way up to the largest gas giants. Figure 1.2 shows the number of planets per star found by *Kepler* orbiting Sun-like stars with periods less than 85 days (Fressin *et al.*, 2013), similar to Mercury's orbital period of 88 days. We now know that hot Jupiters, while easy to detect, are actually quite rare; only $\sim$1% of Sun-like stars have such planets (Fressin *et al.*, 2013; Petigura *et al.*, 2013b,a). On the other hand planets smaller than Neptune ($\sim$4 $R_\oplus$) are commonplace, and many systems have more than one sub-Neptune sized planet.

Specifically, *Kepler* has discovered an abundant new population of close-in $\sim$3 $R_\oplus$ sub-Neptune sized planets (Fressin *et al.*, 2013; Petigura *et al.*, 2013b,a). Although smaller than Neptune, most of these planets are large enough that they must have substantial hydrogen and helium (hereafter H/He) envelopes to explain their size (Lopez and Fortney, 2013b). Yet, unlike Neptune and Uranus, these planets are on highly-irradiated orbits. Such planets are completely unlike anything found in our own Solar System and fundamental questions about their structure and formation still need to be addressed. What are these planets made of and how did they form?

The traditional core-accretion view of planet formation is that planets initially form from a proto-planetary embryo by the accumulation of nearby solid material, i.e., dust and ice grains (e.g, Pollack *et al.*, 1996; Ida and Lin, 2004; Mordasini *et al.*, 2009). These embryos then collide with each other to build up proto-planetary cores (e.g, Chambers and Wetherill, 1998). If these cores become massive enough, they can then accrete hydrogen and helium envelopes

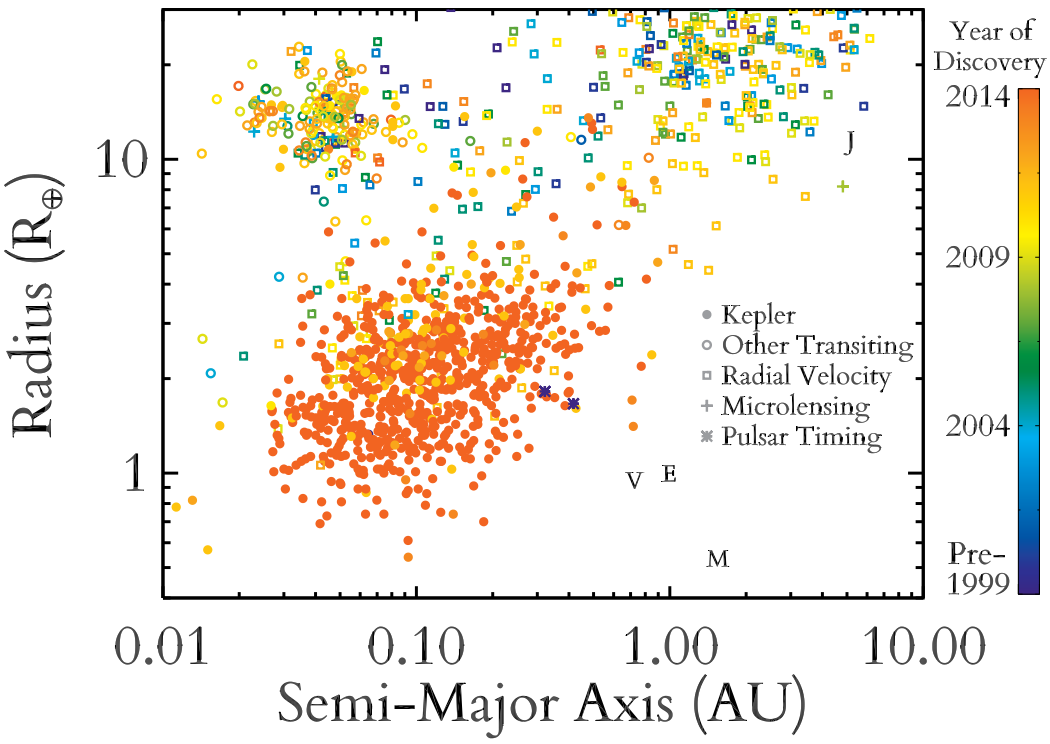

Figure 1.1 Planetary radius vs. semi-major axis. Points are color-coded by the discovery year. Symbols indicate the discovery technique: closed circles for planets found by*Kepler*, open circles for other transiting surveys, open squares for radial velocity, crosses for microlensing, and asterisks for pulsar timing. Letters correspond to Venus, Earth, Mars, and Jupiter. For planets without measured radii, we use the power-law fit to Earth and Saturn $M_{\rm p} = R_{\rm p}^{2.06}$ from (Lissauer *et al.*, 2011b). This shows the large population of increasingly Earth-like planets found by *Kepler*.

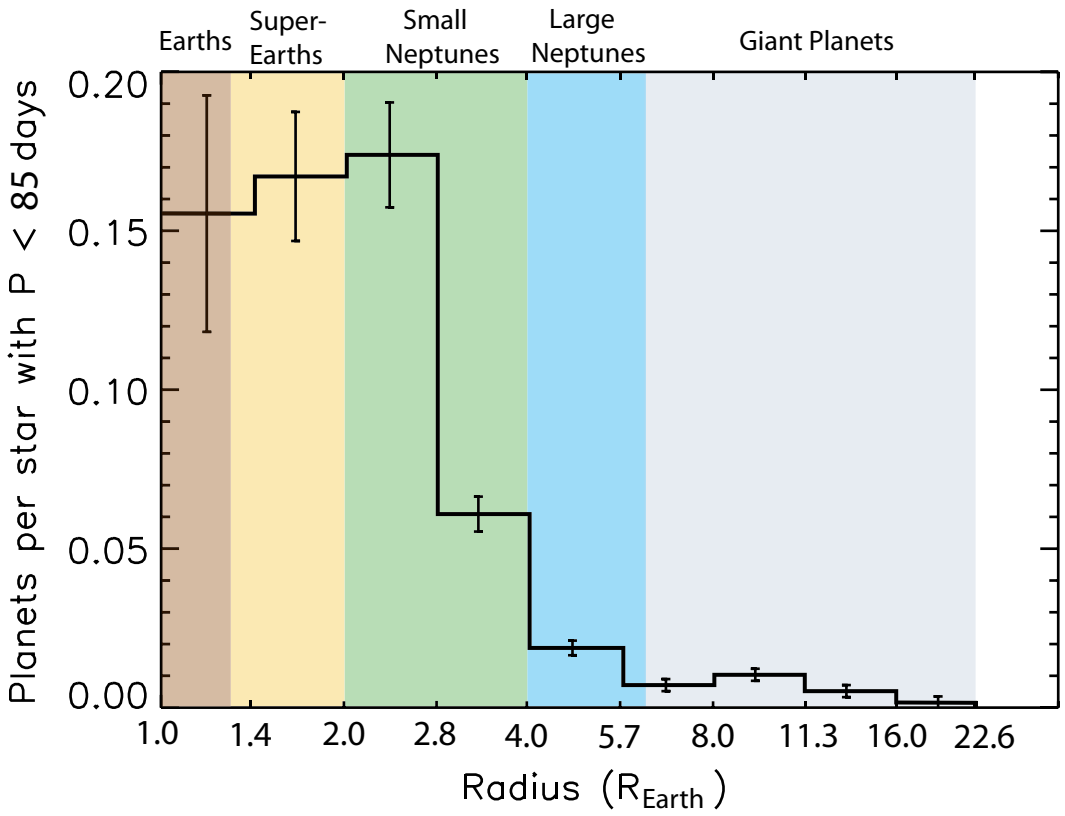

Figure 1.2 Number of planets per star found by *Kepler* orbiting with periods less than 85 days versus planet radius, corrected for selection effects and false positives from Fressin *et al.* (2013).

directly from the circumstellar disk. However, if the cores are relatively low mass or if they take more than a few million years to form, then the gaseous disk will dissipate before the planets can accrete an envelope. In the inner part of the disk, proto-planets will be dominated by rock and iron as in the Earth, since rocky silicates and refractory metals like nickel and iron are the only condensable species for normal abundances at temperatures $\gtrsim$300 K. Meanwhile, ice and gas giants like those in the outer Solar System are believed to form beyond their star's water-ice snowlines, where the increased density of solid material greatly enhances the speed of core driven formation (e.g. Pollack *et al.*, 1996; Ida and Lin, 2004; Mordasini *et al.*, 2009).

What are the sub-Neptunes then? Is most of their mass in water, methane, and ammonia ices as seems to be the case for Uranus and Neptune? Or are they instead rocky planets with a small fraction of their mass in H/He envelopes? In short, are the sub-Neptunes scaled up versions of the Earth or scaled down versions of Neptune?

These are two fundamentally different paradigms of planet formation. If the sub-Neptunes closely resemble the Solar System ice giants, then they need to have formed on wide orbits beyond their stars' snowlines (Rogers *et al.*, 2011). Today, however, we find these planets on highly irradiated orbits within the orbit of Mercury. If the sub-Neptunes are water-rich then they must have undergone dramatic migration by planet-planet scattering (e.g., Rasio and Ford, 1996; Lin and Ida, 1997) or type I migration (e.g., Tanaka *et al.*, 2002; Ida and Lin, 2010; Mordasini *et al.*, 2009). Formation beyond the snowline followed by large inward migration is a common explanation for the formation of the massive short-period hot-Jupiters (e.g., Lin *et al.*, 1996; Alibert *et al.*, 2004). On the other hand if the sub-Neptunes are water-poor then it is possible that they formed at or close to their current orbits (e.g., Hansen and Murray, 2011;

Chiang and Laughlin, 2013). In this case their low densities would be explained by having a few percent of their mass in a H/He envelope, either outgassed from the rocky mantle (Elkins-Tanton and Seager, 2008) or accreted directly from the proto-planetary disk (e.g., Ikoma and Hori, 2012; Mordasini *et al.*, 2011).

Likewise, *Kepler* has also found a similarly abundant population of likely rocky super-Earths $<1.5\ R_{\oplus}$. Such planets are small enough that they are unlikely to have significant H/He envelopes and are consistent with Earth-like abundances of rock and iron (Lopez and Fortney, 2013b). Are these Earth and super-Earth sized planets a natural continuation of the volatile-rich sub-Neptunes, perhaps the evaporated remnants or failed cores of sub-Neptunes, or a completely separate population that formed under different circumstances?

This thesis focuses on understanding the nature and origin of these new populations of extrasolar planets. We have developed coupled thermal evolution and photo-evaporation models that can be used to answer questions both for individual planetary systems and for the population of planets as a whole. In brief, these models are designed to follow a planet's mass, radius, internal structure, and composition over its lifetime. We focus particular attention on aspects of planet evolution which enable us to answer the above questions about the composition and formation of low-mass planets. We highlight particular systems like Kepler-11 and Kepler-36 that are useful case studies to understand planet evolution and we identify key diagnostic trends among the broader planet population.

Transiting planet surveys, like Kepler, primarily measure a planet's radius. Converting a measured radius into an estimate of a planet's composition requires careful modeling of planetary interiors, structures, and evolution. Some planets may be rocky, while others may

have large amounts of H/He or water in deep convective envelopes. Moreover, planets with volatile envelopes will form with large amounts of heat from formation leading to large initial radii, which then contract as the planets age and cool (e.g., Fortney *et al.*, 2007; Marley *et al.*, 2007).

In order to better understand the nature of low-mass low-density planets, in Lopez *et al.* (2012) we developed the first coupled thermal and photo-evaporative evolution model designed for this new class of planets. Using these models, we studied the detailed evolution of many of Kepler's multi-planet systems (e.g., Lopez *et al.*, 2012; Lopez and Fortney, 2013a; Barclay *et al.*, 2013; Gilliland *et al.*, 2013) and predicted planet radii as a function of mass, composition, irradiation, and age (Lopez and Fortney, 2013b). In particular, we found that a planet's size depends strongly on the fraction of its mass in an H/He envelope.

A planet's composition, however, is not necessarily constant throughout its lifetime. Close-in planets, like most of those found by Kepler, are bombarded by large amounts of ionizing radiation in the extreme UV and soft X-rays (jointly referred to as XUV hereafter) (Ribas *et al.*, 2005; Sanz-Forcada *et al.*, 2011). This partially ionizes hydrogen high up in a planet's outer atmosphere, heating gas up to $\sim$10,000 K and creating a collisional planetary wind that can strip away mass (e.g., Sekiya *et al.*, 1980; Yelle, 2004; Murray-Clay *et al.*, 2009). This photo-evaporative wind has been directly observed in Lyman α for a handful of transiting hot Jupiters (e.g., Vidal-Madjar *et al.*, 2004; Lecavelier des Etangs *et al.*, 2004). Likewise, photo-evaporation is believed to have stripped up to a terrestrial ocean of water from the atmosphere of early Venus (e.g., Watson *et al.*, 1981; Kasting and Pollack, 1983). Over billions of years, photo-evaporation can even transform large H/He-rich Neptune sized planets into barren rocky

super-Earths (e.g., Lopez *et al.*, 2012; Lopez and Fortney, 2013a; Owen and Wu, 2013).

Most of this evaporation takes place when planets are young. Young stars rotate more rapidly, leading to stronger magnetic activity and more coronal emission. As a result, when the Sun was only 100 Myr old it was over 100x more luminous in the XUV than it is today (Ribas *et al.*, 2005; Sanz-Forcada *et al.*, 2011). Additionally, planets with H/He envelopes are much more vulnerable to photo-evaporation at early ages due to their large initial radii. Combined, these effects mean that almost all of a planet's photo-evaporative mass loss takes place in its first few 100 Myrs (Lopez *et al.*, 2012). Because *Kepler* studies a relatively old stellar population in the thick disk of the Milky Way, the composition (and therefore radius) distribution seen by *Kepler* today was sculpted by photo-evaporation that took place billions of years ago. By examining trends in the present-day population found by *Kepler* we can uncover evidence of this ancient evaporation.

Chapters 2, 3, and 4 make up the core of this thesis. The material presented there corresponds to Lopez *et al.* (2012), Lopez and Fortney (2013a), and Lopez and Fortney (2013b), respectively. The chapters are arranged chronologically so that the time evolution of the field and our work can be seen.

In Chapter 2 we discuss the development of our models for tracking the coupled thermal and photo-evaporative evolution of low-mass planets. We show that there is strong observational evidence that photo-evaporation impacted the distribution of highly irradiated sub-Neptunes and super-Earths found by Kepler. For the observed population of transiting planets with well-determined masses, we showed that there is a critical photo-evaporation timescale, beyond which there are no observed planets with H/He envelopes. Moreover, we found that

this observed threshold was well reproduced by our coupled thermal and photo-evaporative evolution models using standard photo-evaporation efficiencies (Lopez *et al.*, 2012).

We then apply these planet evolution models to a particularly interesting multi-planet system Kepler-11. With six transiting planets including five low-density Neptunes and sub-Neptunes orbiting a single star, this system presents a unique test case for our models of photo-evaporative evolution. We examine different possible compositions for the five inner planets in the system. We show that the present day masses and radii in Kepler-11 can naturally be explained by photo-evaporation if it is a system of water-rich planets that underwent significant migration.

In Chapter 3 we extend our analysis to further examine the relationship and feedbacks between thermal evolution and photo-evaporation. We show that the evaporative history of a planet depends on the evaporative efficiency, it's level of irradiation, and most important of all, the mass of it's rock-iron core. We show that differences in evaporation histories can naturally explain the large density contrasts found in some multi-planet systems, in particular Kepler-36, a two-planet system in which the mean planetary densities differ by almost an order of magnitude despite very similar orbits.

Moving beyond the photo-evaporation threshold discussed in Chapter 2, we examine the implications of our models for the joint radius-incident flux distribution of planets found by *Kepler*. We show that the frequency of volatile-rich Neptune and sub-Neptune sized planets should increase significantly towards less irradiated orbits, while at short orbital periods $\lesssim$10 days there should be a large population of completely evaporated rocky cores. Moreover, in between the populations of sub-Neptunes and stripped cores, we identify a possible "evapora-

tion valley," in which planets may be quite rare. We discuss how the detection and depth of this valley may be used to constrain the water abundance of close-in low-mass planets, and therefore their formation and migration histories.

In Chapter 4, we examine the thermal evolution of our models in greater detail. We examine how our model planet radii depend on a planet's mass, composition, age, and level of irradiation. Most importantly, we show that at fixed H/He envelope fraction, radii show little dependence on mass for planets with more than $\sim$1% of their mass in their envelope. Consequently, planetary radius is to first order a proxy for planetary composition, i.e., H/He envelope fraction, for Neptune and sub-Neptune sized planets. We recast the observed mass-radius relationship as a mass-*composition* relationship and discuss it in light of traditional core accretion theory. We then discuss these results in light of the observed radius occurrence distribution found by *Kepler*.

Finally, in Chapter 5 we discuss other applications of our planetary evolution models in which I have been a co-author, both to individual systems like Kepler-37 (Barclay *et al.*, 2013) and Kepler-68 (Gilliland *et al.*, 2013) and in statistical studies of the population of planets (Wolgang & Lopez, in prep). We examine ways to further develop these models. We then finish by examining the future direction of exoplanet studies, including the potential impact of new transit surveys like *K2* and *TESS* and new instruments like those on board JWST. We discuss how these upcoming missions may help us final resolve the debate on the origin and composition of *Kepler's* sub-Neptunes and super-Earths and the place of our models in that broader picture.

Chapter 2

How Thermal Evolution and Mass Loss Sculpt Populations of Super-Earths and Sub-Neptunes: Application to the Kepler-11 System and Beyond

2.1 Chapter Introduction

In recent years, the frontier of the search for extrasolar planets has pushed towards ever smaller and more Earth-like worlds. We now know of dozens of Neptune mass planets and have even found the first definitively rocky extrasolar planets (Batalha *et al.*, 2011; Léger *et al.*, 2009). In between, transit searches have begun finding a population of low-mass low-density "super-Earths". Beginning with the discovery of GJ1214b (Charbonneau *et al.*, 2009), these planets represent a new class of exoplanets that do not have any analog in our Solar System.

Basic questions about their composition, structure, and formation are still unknown. Are these, in fact, scaled up versions of the Earth that simply have thick hydrogen/helium envelopes atop of rock/iron cores? Or are they instead scaled down versions of Neptune that are rich in water and other volatile ices?

The distinction between water-poor super-Earths or water-rich sub-Neptunes has fundamental implications for how these planets formed. So far these low-mass low-density (hereafter LMLD) planets have only been found well inside the snow-line. If these planets only contain rock, iron, and hydrogen/helium, then it is possible they formed close to their current orbits (Hansen and Murray, 2011). However, if a significant fraction of their mass is in water, then they must have formed beyond the snow-line and migrated in to their current locations (Alibert *et al.*, 2011; Ida and Lin, 2010; Rogers *et al.*, 2011).

The Kepler-11 system (Lissauer *et al.*, 2011a) is an extremely powerful tool for exploring the features of LMLD planets. With six transiting planets orbiting a close solar analog, it is the richest extrasolar system currently known. Moreover, five of the planets have masses from Transit Timing Variations (TTVs), and all five of these fall into the low-mass low-density regime in between Earth and Neptune. These five planets are all interior to Mercury's orbit, with periods from 10 to 47 days. This provides a unique laboratory to test the possible composition, formation, and evolution of LMLD planets and how these vary as a function of both period and planet mass.

Transiting planets with measured masses, like those in Kepler-11, are particularly valuable because we can determine their mean density. All the planets in Kepler-11 have densities too low for pure rock, and therefore must have some sort of thick envelope of volatiles.

Likewise, all the planets except Kepler-11b are less dense than pure water and so must have at least some hydrogen/helium.

Unfortunately, mass and radius alone cannot uniquely determine a planet's composition. In general, there is a large degeneracy between the relative amounts of rock, iron, water, and hydrogen/helium (Rogers and Seager, 2010a). This problem is particularly acute for planets with radii $\approx 2-4\,R_{\oplus}$, since in this range any of these four constituents can be important. Indeed these sorts of degeneracies have long been a focus of studies of Uranus and Neptune (Hubbard *et al.*, 1991; Fortney *et al.*, 2011a).

One possible solution to the composition problem is to obtain multi-wavelength transmission spectra, as has been done for GJ1214b (Bean *et al.*, 2011; Désert *et al.*, 2011; Croll *et al.*, 2011). Since hydrogen-rich atmospheres have much larger scale heights at a given temperature, near infrared water and methane absorption features will be much more prominent for planets with hydrogen/helium envelopes (Miller-Ricci *et al.*, 2009; Miller-Ricci and Fortney, 2010). Unfortunately, these observations are extremely time intensive and even then the possible presence of clouds can make their interpretation difficult. Even worse, nearly all the systems found by *Kepler* are too faint for these observations with current telescopes.

An alternative is to develop models of the formation and evolution of low-mass planets to try and predict what compositions can form and how those compositions change as a planet evolves. In particular, hydrodynamic mass loss from extreme ultra-violet (XUV) heating can remove large amounts of hydrogen/helium from highly irradiated LMLD planets. Models of XUV driven mass loss were first developed to study water loss from early Venus (Hunten, 1982; Kasting and Pollack, 1983), and hydrogen loss from the early Earth (Sekiya *et al.*, 1980;

Watson *et al.*, 1981). These kinds of models have since been developed to study mass loss from hot Jupiters (e.g., Lammer *et al.*, 2003; Yelle, 2004; Murray-Clay *et al.*, 2009; Ehrenreich and Désert, 2011; Owen and Jackson, 2012), where there is strong evidence that atmospheric escape is an important physical process (Vidal-Madjar *et al.*, 2004; Davis and Wheatley, 2009; Lecavelier Des Etangs *et al.*, 2010; Lecavelier des Etangs *et al.*, 2012).

In Sections 2.2.3, 2.3.3, and 2.5.1 we show that energy-limited hydrodynamic mass loss models, coupled with models of thermal evolution and contraction, can distinguish between water-poor super-Earth and water-rich sub-Neptune scenarios in Kepler-11. Moreover, these models make powerful predictions for the density distribution of the entire population of LMLD transiting planets. In particular, observations show that there is a threshold in the bulk density - incident flux distribution above which there are no LMLD planets. In Section 2.4 we examine this threshold and show how it can by reproduced using our thermal evolution models coupled with standard hydrodynamic mass loss prescriptions. Finally, in Section 2.4.2 we explore how this threshold can be used to obtain important constraints on planets without measured densities: We constrain the maximum radii of non-transiting radial velocity planets, and the minimum masses of *Kepler* candidates.

2.2 Our Model

2.2.1 Planet Structure

We have built on previous work in Fortney *et al.* (2007) and Nettelmann *et al.* (2011) to develop models of the thermal evolution of LMLD planets. To simplify what is undoubtedly a

complex interior structure for real planets, we construct model planets with well-defined layers. Low-mass planets are likely to have a significant fraction of their mass in iron and silicate rocks. For simplicity, we assume that these materials are contained in an isothermal rocky core with Earth-like proportions of 2/3 silicate rock and 1/3 iron. For the rock, we use the ANEOS (Thompson, 1990) olivine equation of state (EOS); while for the iron, we use the SESAME 2140 Fe EOS (Lyon and Johnson, 1992).

On top of this rock/iron core we then attach an interior adiabat. The composition of this adiabat depends on the planet model being considered. For this work, we consider three classes of LMLD planets: rocky super-Earths with H/He envelopes, water-worlds that have pure water envelopes, and sub-Neptunes with a water layer in between the core and the upper H/He layer. For the water-rich sub-Neptune models we assume that this intermediate water-layer has the same mass as the rock/iron core. We choose this value because it is comparable to the water to rock ratio needed to fit Kepler-11b as a water-world. This allows us to explore the proposition that all five Kepler-11 planets started out with similar compositions, but that mass loss has subsequently distinguished them. For hydrogen/helium we use the Saumon *et al.* (1995) EOS. Meanwhile for water we use the ab-initio H2O-REOS EOS developed by Nettelmann *et al.* (2008) and French *et al.* (2009), which was recently confirmed up to 7 Mbar in laboratory experiments (Knudson *et al.*, 2012).

In the Kepler-11 system, our models predict that water will be in the vapor, molecular fluid, and the ionic fluid phases. The interiors are too hot for high pressure ice phases. Finally, we model the radiative upper atmosphere by assuming that the planet becomes isothermal at pressures where the adiabat is cooler than the planet's equilibrium temperature, assuming 20%

Bond albedo and uniform re-radiation. We then calculate the radius at 10 mbar which we take to be the transiting radius.

We connect the different layers of our models models by requiring that pressure and temperature be continuous across boundaries. We then solve for the interior structure assuming hydrostatic equilibrium. A given model is defined by its mass, composition (i.e., the relative proportions in H/He, water, and the rock/iron core) and the entropy of its interior H/He adiabat. By tracking changes in composition and entropy we can then connect these models in time and study the thermal and structural evolution of a given planet.

2.2.2 Thermal Evolution

In order to obtain precise constraints on composition, it is important to fully model how a planet cools and contracts due to thermal evolution. Models that only compute an instantaneous structure (Rogers and Seager, 2010b) by necessity must vary the intrinsic luminosity of the planet over several orders of magnitude, which can introduce large uncertainties in the current composition. Obtaining precise constraints from thermal evolution is essential when considering mass loss, since mass loss histories are highly sensitive to uncertainties in the current composition. Moreover, since mass loss depends strongly on planetary radius (to the third power), the mass loss and thermal histories are inextricably linked.

Modeling this contraction requires a detailed understanding of a planet's energy budget. By tracking the net luminosity of a planet, we know how the specific entropy S, (i.e., the entropy per unit mass) of the interior adiabat changes with time. For a given mass and composition, this adiabat then defines the planet's structure and so we can track the planet's total

radius as the model cools and contracts with time. Equation (2.1) shows the energy budget for our models and how this relates to the change in entropy dS/dt.

$$\int_{M_{\rm core}}^{M_{\rm p}} dm \frac{T\,dS}{dt} = -L_{\rm int} + L_{\rm radio} - c_{\rm v} M_{\rm core} \frac{dT_{\rm core}}{dt} \tag{2.1}$$

The left hand side shows the rate of change of the thermal energy of the interior adiabat. Positive terms on the right hand side represent energy sources that heat and inflate a planet, while negative terms represent energy losses that allow a planet to cool and contract. The term $L_{\rm int} = L_{\rm eff} - L_{\rm eq}$ describes the intrinsic luminosity due to radiation from the planet, where $L_{\rm eq}$ is the planet's luminosity due only to absorbed stellar radiation.

The $L_{\rm radio}$ term describes heating due to radioactive decay. The important long-lived isotopes are ^{235}U, ^{40}K, ^{238}U, and ^{232}Th. These have half lives of 0.704, 1.27, 4.47, and 14.1 Gyr, respectively. We assume meteoritic abundances given by Anders and Grevesse (1989). We do not consider the early decay of ^{26}Al, since we only consider models that are at least 10 Myr after planet formation. The $L_{\rm radio}$ term has only a minor effect on our models since it is typically an order of magnitude smaller than the other terms in equation (2.1).

Lastly, there is the $dT_{\rm core}/dt$ term, which represents the delay in cooling due to the thermal inertia of the rocky core. As the interior adiabat cools, the core isotherm must also cool, as $T_{\rm core}$ equals the temperature at the bottom of the adiabat. When the core makes up a large fraction of the planet's mass, this can significantly slow down the planet's rate of contraction. We assume a core heat capacity of $c_v = 0.5 - 1.0$ J K^{-1} g^{-1} (Alfè *et al.*, 2002; Guillot *et al.*, 1995; Valencia *et al.*, 2010) as in Nettelmann *et al.* (2011). This range covers values appropriate for

both the cores of the Earth and Jupiter. For our three layer sub-Neptune models we still use the mass in rock and iron for $M_{\rm core}$, since the water layer is generally too hot for ice phases and so it is assumed to be fully convective.

For a given interior structure, we determine the intrinsic flux from the interior, at given S of the adiabat, via interpolation in a grid of model atmospheres. The values of $T_{\rm int}$ (a parametrization of the interior flux), $T_{\rm eq}$, and $T_{\rm eff}$ are tabulated on a grid of surface gravity, interior specific entropy, and incident flux for $50\times$ solar metallicity H/He atmospheres (similar to Neptune). This corresponds to a metal mass fraction of $Z \approx 0.35$ and a mean molecular weight of $\mu \approx 3.5\,{\rm g\,mol^{-1}}$. The grid is the same as that described in Nettelmann *et al.* (2011) for LMLD planet GJ 1214b, where a more detailed description can be found. Here we do expand on that grid to now include a range of incident fluxes, as was done for giant planets in Fortney *et al.* (2007).

In choosing the initial entropy for our evolution model, we assume a "hot start" for model; i.e., we start the models out with a large initial entropy. We then allow the models to cool and contract until either 10 Myr or 100 Myr which is when we begin the coupled thermal and mass loss evolution. This is a common but important assumption. However, in general our thermal evolution models are insensitive to the initial entropy choice by ~ 100 Myr as in Marley *et al.* (2007). As a result, we present results at both 10 and 100 Myr. Moreover, to gain confidence in our 10 Myr models we examined the effect of starting those models with a lower initial entropy. Specifically, we ran models in which we started the 10 Myr with the entropies found at 100 Myr. This allowed us to separate the effect of the stellar XUV evolution, from any "hot start" vs. "cold start" uncertainties. Future progress in modeling the formation

of water-rich sub-Neptune planets (e.g., Rogers *et al.*, 2011) may allow for an assessment of the most realistic initial specific entropies.

2.2.3 XUV-Driven Mass Loss

Close-in planets like those in Kepler-11 are highly irradiated by extreme ultraviolet (EUV) and x-ray photons. These photons photoionize atomic hydrogen high in a planet's atmosphere, which in turn produces significant heating (Hunten, 1982). If this heating is large enough, it can generate a hydrodynamic wind that is capable of removing significant mass, potentially including heavier elements as well (Kasting and Pollack, 1983). We couple this XUV driven mass loss to our thermal evolution models following the approach of Jackson *et al.* (2010) and Valencia *et al.* (2010), which explored possible mass loss histories for CoRoT-7b (Léger *et al.*, 2009; Queloz *et al.*, 2009). Similar approaches have also been used to study the coupled evolution of hot Jupiters (e.g., Baraffe *et al.*, 2004, 2005; Hubbard *et al.*, 2007b,a) and hot Neptunes (Baraffe *et al.*, 2006).

A common approach to estimate the mass loss rate is to assume that some fixed fraction of the XUV energy incident on a planet is converted into heat that does work on the atmosphere to remove mass. This is known as the energy-limited approximation (Watson *et al.*, 1981) and allows a relatively simple analytic description of mass loss rates.

$$\dot{M}_{\mathrm{e-lim}} \approx \frac{\epsilon \pi F_{\mathrm{XUV}} R_{\mathrm{XUV}}^3}{G M_{\mathrm{p}} K_{\mathrm{tide}}} \tag{2.2}$$

$$K_{\mathrm{tide}} = (1 - \frac{3}{2\xi} + \frac{1}{2\xi^3}) \tag{2.3}$$

$$\xi = \frac{R_{\rm Hill}}{R_{\rm XUV}} \tag{2.4}$$

Equation (2.2) describes our estimate of the mass loss rate based on the formulation from (Erkaev *et al.*, 2007). $F_{\rm XUV}$ is the total flux between $1-1200$ angstroms, which is given by Ribas *et al.* (2005) for Sun-like stars. For stars older than 100 Myr, Ribas found that at 1 AU, $F_{\rm XUV} = 29.7\tau^{-1.23}\,{\rm erg\,s^{-1}\,cm^{-2}}$, where τ is the age of the star in Gyr. Using this power law, we scale the XUV flux to the appropriate age and semi-major axis for each planet in our models. Although Ribas only targeted Sun-like stars, Sanz-Forcada *et al.* (2010) found similar results for a wide range of stellar types from M3 to F7. Hereafter, we will simply refer to the entire $1-1200$ angstroms ; spectrum as XUV.

$R_{\rm XUV}$ is the planetary radius at which the atmosphere becomes optically thick to XUV photons, which Murray-Clay *et al.* (2009) find occurs at pressures around a nanobar, in the hot Jupiter context. For our work, we assume that the atmosphere is isothermal between the optical and XUV photospheres. This neglects heating from photo-disassociation, which should occur around a μbar (Miller-Ricci Kempton *et al.*, 2012a). However, this effect should be relatively small and if anything will lead to slight underestimate of the mass loss rate. We vary pressure of the XUV photosphere from 0.1 nbar to 10 nbar to include the uncertainty in the structure of the XUV photosphere. For H/He atmospheres on LMLD planets, the nbar radius is typically 10-20% larger than the optical photosphere. $K_{\rm tide}$ is a correction factor that accounts for the fact that mass only needs to reach the Hill radius to escape (Erkaev *et al.*, 2007). For planets like Kepler-11b today this correction factor increases the mass loss rate by $\sim 10\%$, however at early times it can increase the rate by as much as a factor of 2.

Finally, ϵ is an efficiency factor that parametrizes the fraction of the incident XUV flux that is converted into usable work. This efficiency is set by radiative cooling, especially via Lyman α, and can depend on the level of incident flux (Murray-Clay *et al.*, 2009). Kepler-11 is a 8 ± 2 Gyr old Sun-like star. Using the power law from Ribas et al., this implies that current XUV flux at Kepler-11f is $\approx 37\,\mathrm{erg\,s^{-1}\,cm^{-2}}$. Similarly, when Kepler-11 was 100 Myr old, the flux at Kepler-11b was $\approx 6 \times 10^4\,\mathrm{erg\,s^{-1}\,cm^{-2}}$. Murray-Clay *et al.* (2009) found that at XUV fluxes over $10^5\,\mathrm{erg\,s^{-1}\,cm^{-2}}$, relevant for many hot Jupiters, mass loss becomes radiation/recombination-limited and highly inefficient. However, at the lower XUV fluxes relevant for the Kepler-11 system mass loss is roughly linear with F_{XUV} and has efficiencies $\sim 0.1 - 0.3$. For this work, we assume a default efficiency of $\epsilon = 0.1 \pm^{0.1}_{0.05}$, although we do examine the effects of lower efficiencies. While we predominantly investigate the loss of H/He envelopes, in some limited cases for Kepler-11b, we also assume this holds for steam envelope loss.

One important implication from equation (2.2) is that mass loss rates are much higher when planets are young. This is for two reasons. First, at young ages planetary radii are considerably larger due to residual heat from formation. Secondly, at ages less than 100 Myr F_{XUV} was ≈ 500 times higher than it is currently (Ribas *et al.*, 2005). As a result, most of the mass loss happens in a planet's first Gyr. Thus although a planet's envelope may be stable today, its composition may have changed significantly since formation. Likewise, a considerable amount of mass will be lost between the end of planet formation at ~ 10 Myr (Calvet *et al.*, 2002) and 100 Myr. Following the x-ray observations of Jackson *et al.* (2012), we assume that at ages younger than 100 Myr the stellar XUV flux saturates and is constant at the 100 Myr value. Unfortunately, the observations for 10-100 Myr do not cover the EUV (100-1200 angstroms)

Table 2.1. Kepler-11: Current Mass and Composition

Planet	Current Mass ($M_\oplus$)	% H/He	% Water	% H/He 3-layer
Kepler-11b	$4.3\pm^{2.2}_{2.0}$	$0.3\pm^{1.1}_{0.25}$ %	$40\pm^{41}_{29}$ %	n/a
Kepler-11c	$13.5\pm^{4.8}_{6.1}$	$4.6\pm^{2.7}_{2.3}$ %	n/a	$0.3\pm^{1.0}_{0.1}$ %
Kepler-11d	$6.1\pm^{3.1}_{1.7}$	$8.2\pm^{2.7}_{2.4}$ %	n/a	$1.3\pm^{0.9}_{0.8}$ %
Kepler-11e	$8.4\pm^{2.5}_{1.9}$	$17.2\pm^{4.1}_{4.2}$ %	n/a	$5.5\pm^{2.3}_{3.0}$ %
Kepler-11f	$2.3\pm^{2.2}_{1.2}$	$4.1\pm^{1.8}_{1.5}$ %	n/a	$0.4\pm^{0.6}_{0.2}$ %

Note. — Present day masses and compositions for Kepler-11 for three classes of models. The third (fourth) columns list the current H/He fractions predicted by our thermal evolution models assuming two layer H/He (water) on rock/iron model. The final column lists the predicted fraction of H/He for three layer "sub-Neptune" models with equal mass in the rock and water layer. This scenario is not applicable to 11b since it only needs 40% water to match its radius.

part of the spectrum, so there is some uncertainty as to whether this saturation age is uniform across the entire XUV spectrum. Nonetheless, our constraints on the formation of Kepler-11 in sections 2.3.2 and 2.5.1 come from the lower limits we are able to place on the initial compositions. Assuming that the EUV (100-1200 angstroms) saturates along with the x-rays (1-100 angstroms) is conservative assumption in terms of the amount of mass that is lost.

In general, models of LMLD planets that assume H/He envelopes today will predict much larger mass loss histories than models that assume steam envelopes. Partly, this is because of the lower mean molecular weight of hydrogen. Mostly, however, it is because when we integrate the compositions back in time from the present, the addition of a small amount of H/He has much larger impact on a planet's past radius than a small amount of water. A larger radius in the past in turn means a higher mass loss rate; and so the integrated mass loss history becomes much more substantial for H/He envelopes.

2.3 Application to Kepler-11

2.3.1 Current Compositions from Thermal Evolution

The first step in trying to understand the formation and history of a planetary system is to identify the possible current compositions for each of the planets in the absence of any mass loss. This then gives us estimates for the current masses of each planet's core, which we then use as the starting point for all of our calculations with mass loss.

Figure 2.1 shows the Kepler-11 planets in a mass-radius diagram along with curves for different possible compositions. For all planets, we color-code by the incident bolometric

flux they receive. The Kepler-11 planets are shown by filled circles with identifying letters next to each one. The other known transiting exoplanets in this mass and radius range are shown by the open squares. In order of increasing radius, these are Kepler-10b (Batalha *et al.*, 2011), Kepler-36b (Carter *et al.*, 2012), CoRoT-7b (Léger *et al.*, 2009; Queloz *et al.*, 2009; Hatzes *et al.*, 2011), Kepler-20b (Fressin *et al.*, 2012; Gautier *et al.*, 2012), Kepler-18b (Cochran *et al.*, 2011), 55 Cancri e (Winn *et al.*, 2011; Demory *et al.*, 2011), GJ 1214b (Charbonneau *et al.*, 2009), Kepler-36c (Carter *et al.*, 2012), Kepler-30b (Fabrycky *et al.*, 2012; Sanchis-Ojeda *et al.*, 2012), and GJ 3470b (Bonfils *et al.*, 2012). Lastly, the open triangles show the four planets in our own solar system that fall in this range: Venus, Earth, Uranus, and Neptune.

The curves show various possible compositions. The solid black curve shows a standard Earth-like composition with 2/3 rock and 1/3 iron as described in Section 2.2.1. The other curves show compositions with thick water or H/He envelopes atop an Earth-like core. These curves include thermal evolution without mass loss to 8 Gyr, the age of Kepler-11. The blue dashed curves show the results for 50% and 100% water-worlds computed at $T_{\rm eq}$ = 700 K, approximately the average temperature of the five inaner planets. Likewise, the dotted orange curves show the results for H/He envelopes; however, here each curve is tailored to match a specific Kepler-11 planet and is computed at the flux of that planet. These fits are listed in greater detail in table 2.1. Here we list the mass of each planet taken from Lissauer *et al.* (2011a); the H/He fractions needed to match each planet's current radius for a water-poor super-Earth model; the water fraction needed to match Kepler-11b as a water-world; and the H/He fractions needed to fit Kepler-11c, d, e, and f as sub-Neptunes with an intermediate water layer, as described in Section 2.2.1. As described in section 2.3.2, we varied the planetary albedo, the heat capacity

of the rocky core, and the observed mass, radius, current age, and incident flux.

Figure 2.1 and table 2.1 clearly show the degeneracy between various compositions that we are attempting to untangle. There are now four planets including Kepler-11b that can easily be fit either as water-worlds or as water-rich sub-Neptunes with $< 2\%$ of their mass in H/He. However, it is worth looking closer at Kepler-11b in particular. It is the only planet in the system which does not require any hydrogen or helium to match its current radius, although it must have some sort of volatile envelope. Moreover, it is also the most irradiated and it is fairly low gravity. As a result, adding a small amount of hydrogen to its current composition has a large impact on the bulk density, which in turn makes the planet more vulnerable to mass loss, as seen in Eq. (2.2). A clearer picture for this planet emerges when including XUV driven mass-loss and relatively strong constraints from formation models discussed in Section 2.5.1. Thus, if there is hope of using mass loss to constrain the composition and formation of the system, it likely lies with Kepler-11b.

2.3.2 Mass Loss for a Super-Earth Scenario

Now that we have estimates for the present day compositions, we will begin considering the effects of mass loss. We will compute mass loss histories that when evolved to the present day, match the current mass and composition. This then tells us what the mass would have to be in the past to result in the current mass and composition. As discussed in Section 2.2.3, there is uncertainty in stellar XUV fluxes ages younger than 100 Myr; as a result, we will present results both at 10 Myr and 100 Myr after planet formation.

First we will consider water-poor super-Earth models for each planet, which have

Table 2.2. Kepler-11 Results from Mass Loss: Mass and Composition for Super-Earths

Planet	Mass 10^8 yr ($M_\oplus$)	% H/He 10^8 yr	Mass 10^7 yr ($M_\oplus$)	% H/He 10^7 yr
Kepler-11b	$34.6\pm^{6.5}_{28.2}$	$87.6\pm^{6.6}_{85.4}$ %	$44.8\pm^{9.7}_{10.1}$	$90.4\pm^{5.1}_{8.2}$ %
Kepler-11c	$13.7\pm^{4.7}_{5.8}$	$6.0\pm^{5.0}_{3.2}$ %	$14.2\pm^{4.3}_{3.1}$	$9.1\pm^{28}_{7.3}$ %
Kepler-11d	$6.7\pm^{2.8}_{0.6}$	$16.5\pm^{22}_{8.5}$ %	$7.8\pm^{12.8}_{0.8}$	$28\pm^{56}_{17}$ %
Kepler-11e	$8.8\pm^{2.3}_{1.6}$	$21.2\pm^{6.0}_{3.2}$ %	$9.7\pm^{2.5}_{1.9}$	$28.1\pm^{10.5}_{7.7}$ %
Kepler-11f	$3.1\pm^{5.2}_{0.2}$	$29\pm^{58}_{24}$ %	$3.4\pm^{6.6}_{0.4}$	$35\pm^{57}_{25}$ %

Note. — Masses and H/He fractions predicted by coupled mass loss and thermal evolution models at 100 and 10 Myr, assuming all five planets are water-poor super-Earths. The large error bars on some compositions are due mostly to uncertainties in the current masses from TTV. The 10 Myr values are subject to some model uncertainties as discussed in sections 2.2.2 and 2.2.3. Kepler-11b is extremely vulnerable to H/He mass loss and would have to start off implausibly massive to retain a small H/He envelope today. Kepler-11c, d, e, and f are all consistent with have formed with $\sim$30% H/He.

H/He envelopes atop Earth-like rocky cores. As discussed in Section 2.2.3, H/He envelopes are particularly susceptible to mass loss. As an example, Figure 2.2 shows four possible cooling histories for Kepler-11b. The solid lines show thermal evolution without any mass loss while the dashed lines include mass loss. The orange curves are for water-poor super-Earth models, while the blue curves show water-world models. The red cross shows the current radius and age of Kepler-11b. These curves illustrate the impacts of both thermal evolution and mass loss on the radius of a low-mass planet. The water-world models require that 40% of the current mass must be in water to match the current radius. Assuming our standard efficiency $\epsilon = 0.1$, implies an initial composition of 43% water at 10 Myr. This illustrates the relative stability of water envelopes. On the other hand, the dashed orange curve shows the vulnerability of H/He layers. Here we have assumed a efficiency $5\times$ lower $\epsilon = 0.02$ and yet more mass is lost than in the water-world scenario. Even at this low efficiency, Kepler-11b would have to initially be 11% H/He and 4.8 $M_{\oplus}$ to retain the 0.3% needed to match the current radius. This also shows the large increase in radius that can result from even a relatively modest increase in the H/He mass.

Table 2.2 summarizes the results for Kepler-11 b-f for the water-poor super-Earth scenario. We list the masses predicted by our models when the planets were 10 and 100 Myr old. In addition, we list the fraction of the planets' masses in the H/He envelope at each age. These results are further illustrated in Figure 2.4a. Here we have plotted the mass and H/He fraction for each planet at 10 Myr, 100 Myr, and today. Each color corresponds to a particular planet with the squares indicating the current masses and compositions, the circles the results at 100 Myr, and the triangles the results at 10 Myr. In order to calculate the uncertainty on

these results, we varied the mass loss efficiency ϵ from 5-20% and varied the XUV photosphere from 0.1-10 nbar. Likewise, we varied the planetary Bond albedo from 0-0.80 and varied the heat capacity of the rocky core from 0.5-1.0 $\mathrm{J\,g^{-1}\,K^{-1}}$. Also, as discussed in section 2.2.2, we varied the initial entropy for the 10 Myr models, to account for undertainties in "hot-start" vs. "cold-start". Finally, we factored in the observed uncertainties in mass, radius, and incident flux.

Clearly, Kepler-11b is vulnerable to extreme mass loss if it has a H/He envelope atop a rock/iron core. Although less than 1% H/He today, if it is a water-poor super-Earth it could have been have over $\sim$ 90% H/He in the past. At 10 Myr, its mass would have been 45 ± 10 $M_{\oplus}$, an order of magnitude higher than the current value. Kepler-11b is able to undergo such extreme mass loss because its high XUV flux and the low mass of its rocky core put it in a regime where it is possible to enter a type of runaway mass loss. This happens when the mass loss timescale is significantly shorter then the cooling timescale. After the planet initially loses mass it has an interior adiabat and rocky core that are significantly hotter than would otherwise be expected for a planet of its mass and age. This is because the interior still remembers when the planet was more massive and has not had sufficient time to cool. As a result, the planet will stay inflated for some time and the density stays roughly constant and can actually decrease. A similar effect was seen by Baraffe *et al.* (2004) when they studied coupled thermal evolution and mass loss models for core-less hot Jupiters. We find that this process generally shuts off once the composition drops below $\sim$20% H/He. At that point the presence of the core forces the total radius to shrink even if the planet is unable to cool efficiently. Figure 2.3 shows this process as Kepler-11b loses mass for three different values of its current mass and therefore its

core mass. The curves correspond to the best fit mass from transit-timing as well as the 1σ error bars. This shows that the timing of this runaway loss event depends strongly on the mass of the rock/iron core.

Super-Earth models of Kepler-11b are unusual in that they are subject to tremendous mass loss and yet they retain a small amount of H/He today. Typically models that start out $\sim 90\%$ H/He either experience runaway mass loss and lose their H/He envelopes completely, or they never enter the runaway regime and remain over 50% H/He. The uncertainty in the initial composition of Kepler-11b is due to uncertainty in its TTV mass. At a given current mass, the range of Kepler-11b models that will retain an envelope that is $< 1\%$ H/He is extremely narrow. In this sense, the current composition of Kepler-11b requires a rare set of initial conditions if it is a water-poor super-Earth.

Counter-intuitively, if Kepler-11b is more massive today then its implied mass in the past is actually lower. This is because a higher mass today would imply a more massive core, which would increase the planet's density and decrease its mass loss rate. As a result, a more massive model for Kepler-11b today is less vulnerable to mass loss and so less H/He is needed in the past in order to retain 0.3% today. At 100 Myr, there is a very large uncertainty in the composition due to the uncertainty in the core mass. However, even if we assume the 1σ error bar 6.5 $M_\oplus$, Kepler-11b would still be at least 37 $M_\oplus$ and at least 83% H/He at 10 Myr. In section 2.5.1, we will compare this to models of in situ formation and show that such a scenario is unlikely.

On the other hand, Kepler-11c is not particularly vulnerable to mass loss, at least using the best fit mass from transit timing, despite having the second highest flux in system.

Table 2.3. Kepler-11 Results from Mass Loss: Water-Worlds and Sub-Neptunes

Planet	Mass 10^8 yr ($M_\oplus$)	% H/He 10^8 yr	Mass 10^7 yr ($M_\oplus$)	% H/He 10^7 yr
Kepler-11b	$4.4\pm^{2.2}_{2.0}$	$41\pm^{39}_{28}$ %	$4.5\pm^{2.1}_{1.8}$	$43\pm^{38}_{29}$ %
Kepler-11c	$13.7\pm^{4.8}_{4.6}$	$1.8\pm^{18}_{1.4}$ %	$15.2\pm^{25}_{1.2}$	$12\pm^{70}_{10}$ %
Kepler-11d	$6.8\pm^{2.8}_{1.2}$	$11.6\pm^{17}_{8.7}$ %	$7.6\pm^{7.6}_{0.9}$	$21\pm^{49}_{10}$ %
Kepler-11e	$9.1\pm^{2.1}_{2.0}$	$12.8\pm^{4.6}_{6.7}$ %	$9.7\pm^{2.6}_{2.0}$	$18\pm^{12}_{10}$ %
Kepler-11f	$2.9\pm^{3.8}_{0.5}$	$21\pm^{62}_{17}$ %	$4.0\pm^{4.9}_{1.5}$	$43\pm^{44}_{36}$ %

Note. — Masses and volatile fractions predicted by coupled mass loss and thermal evolution models at 100 and 10 Myr, assuming Kepler-11c, d, e, and f are water-rich sub-Neptunes and Kepler-11b is a water-world. Thus the compositions listed for Kepler-11b are water fractions, while those for Kepler-11c-f are H/He fractions. Kepler-11c-f are all consistent with having formed as water-rich sub-Neptunes with 20-30% H/He. Kepler-11b is not vulnerable to mass loss if it has a water envelope; however, it could have easily also formed a water-rich sub-Neptune and lost its H/He envelope.

This is because of the relatively large mass of its rocky core; the high gravity means additional H/He has a more modest effect of the planet's radius and therefore on the mass loss rate. In fact, along with the incident XUV flux the mass of the rocky core is the single largest factor that determines whether a given planet will be vulnerable to mass loss. As a result, the dominant sources of uncertainty in our mass loss models are the uncertainties in the masses from TTV. These dominate over all the theoretical uncertainties in the thermal evolution and mass loss models. The uncertainty in planet mass from transit timing is particular large for Kepler-11c. If its mass is close to the 1σ low value, then it is possible Kepler-11c has undergone more substantial mass loss similar to Kepler-11d-f. Fortunately, as more quarters of data are processed the mass estimates from TTV will become more precise (Agol *et al.*, 2005; Holman and Murray, 2005). Finally, Kepler-11d, e, and f are modestly vulnerable to mass loss and are consistent with having originated with $\sim$ 20% H/He at 100 Myr and $\sim$ 30% H/He at 10 Myr. In Section 2.5.2 we will discuss these results in terms of orbital stability.

2.3.3 The Water-Rich Scenario

Next we consider a water-rich scenario where the entire system formed beyond the snow line. We assume that Kepler-11c-f are water-rich sub-Neptunes as described in Section 2.2.1, while Kepler-11b is currently a water-world. Otherwise the thermal mass loss histories are calculated in the same manner as the water-poor super-Earth scenario. For Kepler-11c-f we calculate the planet mass H/He fraction at 10 and 100 Myr, assuming that only H/He is lost. For Kepler-11b, we examine the vulnerability of both H/He and steam envelopes atop water-rich interiors. The results are summarized in Table 2.3 which list the water fraction for a

water-world model of Kepler-11b and the H/He fraction for water-rich sub-Neptune models of Kepler-11c-f. Likewise, the results for c-f are shown in Figure 2.4b.

In general, the three layer models are slightly more vulnerable to mass loss than the water-poor super-Earth models presented in section 2.3.2. Mostly this is because models with a water layer have hotter interiors that cool more slowly. For example, for Kepler-11c without mass loss the models presented in Table 2.1, at 8 Gyr the final entropy in the H/He layer is 6.6 k_b/baryon for the water-rich sub-Neptune model versus 5.8 for the water-poor super-Earth model. The second reason is that counter-intuitively the water-rich sub-Neptune models are slightly more vulnerable to mass loss precisely because they have less of the planet's mass in H/He today. For a planet that has less H/He today, adding a small amount of H/He at the margin has a larger impact on the planet's radius and therefore on the mass loss rate.

For Kepler-11c-f the results are broadly similar to those for the water-poor super-Earth scenario. Kepler-11c is again the least vulnerable to mass loss; while Kepler-11d is again the most vulnerable of the four planets that we model as water-rich sub-Neptunes. However, all four of these planets are consistent with having been $\sim 10-20\%$ H/He at 100 Myr and $\sim 20-30\%$ H/He at 10 Myr.

If Kepler-11b was always a water-world, then mass loss was never important for it. Between 10 Myr and the present, it only drops from 43% to 40% water. Moreover, if Kepler-11b was initially a water-rich sub-Neptune similar to the other planets in the system, it could have easily stripped its H/He outer envelope. If we start Kepler-11b at 100 Myr as a water-rich sub-Neptune similar to the other planets with 30% H/He atop 4.3 $M_\oplus$ of rock and water, then assuming $\epsilon = 0.1$ the entire H/He envelope will be stripped by 300 Myr. We can set upper limits

on the initial mass and H/He fraction of 70 $M_\oplus$ and 94% if Kepler-11b was originally a water-rich sub-Neptune. These are however strictly upper limits, a H/He layer could have been lost at any time between formation and now. Therefore, all five planets are consistent with a scenario is which they formed as water-rich sub-Neptunes with $\sim$ 10% H/He at 100 Myr and $\sim$ 20% H/He at 10 Myr.

2.4 A Mass Loss Threshold for Low-Mass Low-Density Planets

Although Kepler-11 provides a unique case-study, it is essential to explore how mass loss impacts the larger population of LMLD transiting planets. Figure 2.5 shows the bolometric flux these planets receive at the top of their atmospheres vs. their bulk densities. As in Figure 2.1, filled circles show the Kepler-11 planets with the letters indicating each planet. The open squares show the other transiting exoplanets that are less than 15 Earth masses. For reference, we have also plotted all other transiting planets between 15 and 100 $M_\oplus$ as gray crosses (Wright *et al.*, 2011). The colors indicate possible compositions. All planets with a best-fit mass and radius that lies below a pure rock curve are colored red. These include Kepler-10b, Kepler-36b, CoRoT-7b, and just barely Kepler-20b. Planets that are less dense than pure rock but more dense than pure water, indicating that the could potentially be water-worlds, are colored blue. These include Kepler-11b, Kepler-18b, and 55 Cancri e. Meanwhile those planets that must have a H/He envelope to match their radius are colored orange. These include Kepler-11c, d, e, and f, Kepler-30b, Kepler-36c, GJ 1214b, and GJ 3470b.

The dashed black lines show curves of constant mass loss rate according to equation

(2.2), assuming $\epsilon = 0.1$ and $K_{\rm tide} = 1$. These curves are linear in this plot since the instantaneous mass loss rate goes as the flux over the density. Although Figure 2.5 plots the bolometric flux today, we can relate this to an XUV flux at a given time using the Ribas *et al.* (2005) power law for sun-like stars described in Section 2.2.3. The curves show the flux today required to lose mass at 1 $M_\oplus\,{\rm Gyr}^{-1}$ when the planets were 1 Gyr old and 100 Myr old, along with another curve showing 0.1 $M_\oplus\,{\rm Gyr}^{-1}$ at 100 Myr. Since most of the mass loss happens in the first few hundred Myrs, the bottom two curves can roughly be considered as the respective thresholds for mass loss being important and being unimportant for LMLD planets.

One possible explanation of this mass loss threshold is that it is caused by XUV driven mass loss from H/He envelopes on low-mass planets. LMLD planets that form above the 100 Myr 1 $M_\oplus\,{\rm Gyr}^{-1}$ curve lose mass, increase in density and move to the right until they lie below this threshold. The planets that are left above this line are mostly rocky or at the very least probably do not have H/He envelopes. Planets more massive than $\sim 15\ M_\oplus$ are not affected since they have a larger reservoir of mass and the loss of a few earth masses of volatiles isn't sufficient to significantly change their bulk density. To illustrate this, we have plotted our predictions for the bulk densities of each of the Kepler-11 planets at 100 Myr, including the effects of both mass loss and thermal evolution. These are indicated by the shadowed letters at the left of Figure 2.5.

The situation becomes even clearer if we instead we plot flux against mass times density as in Figure 2.6. The timescale for XUV mass loss goes like $\rho M_{\rm p}/F_{\rm XUV}$, so lines in this diagram are constant mass loss timescales. Now the threshold is much clearer and applies to all planets up to all planets with H/He envelopes. This also removes any effects from the somewhat

arbitrary 15 $M_\oplus$ cut.The sparsity of planets at low flux and high density is almost certainly a selection effect, since these are likely to be planets with long periods and small radii. However, the interesting result is that there is appears to be a critical mass loss timescale above which we do not find any planets with H/He envelopes. In particular, all five of the inner Kepler-11 planets lie nicely along this threshold. Moreover, of the three planets that lie above the critical mass loss timescale, two are likely rocky.

$$t_{\rm loss} = \frac{M_{\rm p}}{\dot{M}} = \frac{GM_{\rm p}^2}{\pi \epsilon R_{\rm p}^3 F_{\rm XUV,E100}} \frac{F_\oplus}{F_{\rm p}} \tag{2.5}$$

The dashed black line in Figure 2.6 shows our best fit for this critical mass loss timescale. Equation 2.5 defines this mass loss timescale. Here $\epsilon = 0.1$ is the mass loss efficiency, $F_{\rm XUV,E100} = 504$ erg s^{-1} cm^{-2} is the XUV flux at the Earth when it was 100 Myr old, and $F_{\rm p}$ is the current incident bolometric flux at a planet. We find a best fit with $t_{\rm loss,crit} \approx 12$ Gyr. However, while equation 2.5 accounts for the higher XUV fluxes at earlier times, it does not include the effects of larger radii at formation. The will reduce $t_{\rm loss}$ by at least another order of magnitude.

A similar mass loss threshold was proposed by Lecavelier Des Etangs (2007). Unfortunately, at that time there were relatively few transiting planets and no known transiting super-Earths. As a result, the authors we mostly limited to hot Jupiters from radial velocity surveys and were forced to use a scaling law to estimate radii. Here we are able to confirm the existence of a mass loss threshold and extend it all the way down to $\sim 2\ M_\oplus$.

This mass loss threshold could also help explain features in occurrence rate of planets

found by *Kepler*. Howard *et al.* (2012) found that the frequency of 2-4 $R_\oplus$ *Kepler* planet candidates dropped off exponentially for periods less than 7 days. This 7 day cutoff corresponds to an incident bolometric flux of 200 $F_\oplus$. There are five planets with measured densities in figure 2.5 that lie above 200 $F_\oplus$. Of these five, three planets are consistent with being rocky and two with being water-worlds; none of the five requires a H/He atmosphere to match its observed mass and radius. If all low mass planets orbiting within 7 days lose their H/He atmospheres, then their radii will shrink from 2-4 $R_\oplus$ to <2 $R_\oplus$. This could naturally explain the drop off in 2-4 $R_\oplus$ candidates at short periods.

2.4.1 Reproducing the Mass Loss Threshold

In order to fully examine whether the mass loss threshold in Figure 2.5 can be explained by atmospheric mass loss, we performed a small parameter study with $\sim$800 mass loss models across a wide range of initial masses, compositions, and incident fluxes. For each model we ran thermal evolution and mass loss starting at 10 Myr around a Sun-like star. We ran models with initial masses of 2, 4, 8, 16, 32, and 64 $M_\oplus$. We assumed water-poor super-Earth compositions, meaning H/He envelopes on top Earth-like cores, with initial compositions of 1, 2, 5, 10, 20, and 40% H/He. Finally we varied the incident bolometric flux from 10 to 1000 $F_\oplus$, in order to cover the range of observed planets in Figures 2.5 and 2.6. We then recorded the resulting masses, densities, and compositions at various ages.

The results are shown in Figure 2.7. As in Figure 2.6, each panel plots the total incident flux at the top of the atmosphere vs. the planet mass times density assuming different mass loss histories for our full suite of models. The size of each point indicates the mass of

the planet, while the color indicates the fraction of its mass in the H/He envelope. The top left panel shows the initial distribution at 10 Myr before we start any mass loss. The other two top panels show the results at 100 Myr and 10 Gyr for our standard mass loss efficiency $\epsilon = 0.1$. Meanwhile, the bottom panels show the results at 1 Gyr for a range of different efficiencies. These range from highly inefficient mass loss $\epsilon = 0.01$, to our standard efficiency $\epsilon = 0.1$, and finally extremely efficient mass loss $\epsilon = 1$. In each panel, as planets cool and lose mass the points move to the right, shrink, and become bluer (less H/He). For reference, we have re-plotted our critical mass loss timescale from Figure 2.6 in each of the result panels.

As we can see, models with mass loss do in general result in a threshold roughly corresponding to a critical mass loss timescale. Moreover, the mass loss threshold observed in Figure 2.5 is well reproduced by mass loss models with $\epsilon \approx 0.1$. This is similar to the efficiencies found by detailed models of mass loss from hot Jupiters in the energy-limited regime (Murray-Clay *et al.*, 2009). This suggests that our assumption of comparable mass loss efficiencies for LMLD planets is reasonable. It is also apparent that the threshold already in place by 100 Myr, and subsequent evolution has a relatively minor effect. We also examined the effect of beginning our parameter study at 100 rather than 10 Myr; however, this did not significantly affect the location of the threshold.

Previous mass loss evolution models (e.g., Hubbard *et al.*, 2007b,a; Jackson *et al.*, 2012; Owen and Jackson, 2012) have also predicted mass loss thresholds. However, our models are the first to fully include the effects of coupled mass loss and thermal evolution for LMLD planets. We are able confirm and explain the observed threshold seen in Figure 2.6 in a region of parameter space where most of the *Kepler* planets are being found.

2.4.2 Constraints On Mass and Radius for the General Population

If we use the critical mass loss timescale curve from Figure 2.6 as a approximation for the observed mass loss threshold, then we can write down a simple expression for the threshold. This is shown in equation (2.6), which is valid for planets around Sun-like stars with $F_{\rm p} < 500$ $F_{\oplus}$. The 500 $F_{\oplus}$ cut excludes highly irradiated rocky planets like Kepler-10b and CoRoT-7b. These planets may have once had volatiles in the past, but they are likely rocky today and so H/He mass loss is no longer relevant. This cut also excludes the region where energy-limited escape breaks down and mass loss becomes radiation and recombination limited (Murray-Clay *et al.*, 2009)

$$\rho M_{\rm p} \geq \frac{3\epsilon F_{\rm XUV,E100}}{4G} \frac{F_{\rm p}}{F_{\oplus}} t_{\rm loss,crit} \tag{2.6}$$

The exciting implication of equation (2.6) is that we can use it to obtain lower limits on mass for the much larger population of *Kepler* super-Earths and sub-Neptunes for which we do not have measured densities. This will help identify promising targets for follow-up work with radial velocity observations. This is shown in equation (2.7).

$$M_{\rm p} \geq \sqrt{\frac{\pi\epsilon F_{\rm XUV,E100}}{G} \frac{F_{\rm p}}{F_{\oplus}} t_{\rm loss,crit}} R_{\rm p}^{3/2} \tag{2.7}$$

Table A.1 applies equation (2.7) to a list of *Kepler* candidates smaller than 4 $R_{\oplus}$ that are well suited to radial-velocity follow-up. We excluded any planets with $F_{\rm p} > 500$ $F_{\oplus}$, since equation (2.7) is not valid in that regime. Also, we limited the sample to only those planets with

minimum radial velocity semi-amplitudes $K_{\rm min} > 1.0\,{\rm m\,s^{-1}}$ around stars with Kepler magnitude brighter than 13, since these will be the most promising for RV follow-up. In the end, this leaves us with a list of 38 likely detectable targets, eight of which (KOIs 104.01, 107.01, 123.01, 246.01, 262.02, 288.01, 984.01, and 1241.02) have $K_{\rm min} > 2.0\,{\rm m\,s^{-1}}$.

Finally, we can also use the mass loss threshold to find an upper limit on the radii of non-transiting planets from radial velocity surveys with $F_{\rm p} < 500\ F_{\oplus}$. This is done in equation (2.8).

$$R_{\rm p} \leq \left(\frac{G}{\pi \epsilon F_{\rm XUV,E100} t_{\rm loss,crit}} \frac{F_{\oplus}}{F_{\rm p}}\right)^{1/3} M_{\rm p}^{2/3} \tag{2.8}$$

2.5 Discussion

2.5.1 Kepler-11: Comparison to Formation Models, Implications for Migration

By itself, the constraints from mass loss do not tell us whether Kepler-11 is a system of water-poor super-Earths or water-rich sub-Neptunes. Instead we need to compare our estimates of the initial compositions to models of planet formation. By doing so we can examine whether our estimates of the original compositions for a water-poor super-Earth scenario are consistent with the maximum H/He fraction that can be accreted during in situ formation.

Ikoma and Hori (2012) examine the accretion of H/He atmospheres onto the rocky cores of hot water-poor super-Earths. In particular, they examine the in situ formation of the Kepler-11 system. In addition to a planet's core mass and temperature, the amount of H/He accreted will depend strongly on the lifetime and dust grain opacity of the accretion disk. As

with thermal evolution, the need to cool the rocky core can slow the contraction of the accreting atmosphere and limit the final H/He fraction. They are able to set hard upper limits on the initial compositions for in situ formation by assuming a grain-free, long-lived ($\sim$ 1 Myr in the inner 0.2 AU) accretion disk and ignoring the delay in accretion due to cooling the cores.

In particular, Ikoma and Hori (2012) find that Kepler-11b could not have accreted more than 10% of its mass in H/He if it formed in situ. Moreover, using a more typical disk lifetime of 10^5 yr (Gorti *et al.*, 2009) and including the effect of cooling the core implies that Kepler-11b was $<$ 1% H/He at formation. On the other hand, in Table 2.2 we showed that thermal evolution and mass loss models predict that if Kepler-11b is a water-poor super-Earth then it was $87 \pm^{7}_{85}$ % H/He and at least 82% H/He at 10 Myr. Combined with the results of Ikoma and Hori (2012), this disfavors in situ formation of Kepler-11b. This result appears robust to any uncertainties in thermal evolution or mass loss models. Even if we only look after the period of run-away mass loss, at 3 Gyr Kepler-11b was still 10% H/He, the maximum allowed by Ikoma and Hori (2012). Likewise, we find that Kepler-11f was at least 10% H/He at 10 Myr, even though the Ikoma and Hori (2012) models predict that it cannot have accreted its current composition of 4% H/He if it formed in situ. Furthermore, the co-planar, tightly packed, circular orbits in the system strongly suggest that it could have undergone type 1 migration (Ida and Lin, 2010). As a result, we disfavor in situ formation of the system.

If the Kepler-11 system did not form at its current location, then one possibility is that it formed at or beyond the snow-line and then Type 1 migrated to it is current location (Rogers *et al.*, 2011). If this is the case, then it is likely a system of water-rich sub-Neptunes and water-worlds as discussed in Section 2.3.3. As we showed in Section 2.3.3, Kepler-11b is

very stable to mass-loss if it is a water-world. If it was initially a water-rich sub-Neptune, it could have easily lost its H/He layer in the first few 100 Myr. Likewise, Kepler-11c-f are all consistent having formed as water-rich sub-Neptunes with $\sim$ 20% of their mass in H/He.

The other possibility is that Kepler-11 is a system of water-poor super-Earths that has nonetheless undergone significant migration. For a grain-free accretion disk that lasts 10^6 yr at 550 K, the critical mass for run-away accretion drops to 5 $M_\oplus$ (Ikoma and Hori, 2012). This implies that Kepler-11b could possibly have formed as a water-poor super-Earth at or beyond the current orbit of 11f. Nonetheless, this assumes a completely grain-free long-lived disk, which may not be realistic. Furthermore, this scenario still requires that Kepler-11b was $\sim$90% H/He when it formed, while all the other planets in the system are consistent with more modest initial compositions. As a result, we favor the water-rich sub-Neptune scenario.

2.5.2 Kepler 11: Mass Loss and Orbital Stability

One possible result of significant mass loss is that it could impact the orbital stability of closely packed multi-planet systems like Kepler-11. Although this system is stable in its current configuration, it might not be with the initial masses determined by our models. One relatively simple stability check is to calculate the separation between pairs of planets in terms of their mutual Hill spheres. Figure 2.8 plots the separation in mutual Hill spheres (Δ) between adjacent pairs of planets at both 10 Myr and the present, assuming a water-poor super-Earth composition.

Smith and Lissauer (2009) found that systems with five or more planets tended to de-stabilize when $\Delta < 9$. This threshold is shown as dashed gray lines in figure 2.8. Although

Kepler-11b-c currently lies well below this threshold, Lissauer *et al.* (2011a) showed that the system is nevertheless stable today because planets b and c are dynamically decoupled from the other four planets and so act more like a two planet system. For two planet systems the absolute minimum stable separation is $\Delta = 2\sqrt{3} = 3.46$ (Gladman, 1993). This second stability threshold is shown by the dotted lines in figure 2.8. The Hill radius goes as $M_p^{1/3}$, as a result the change in Δ from mass loss is relatively modest; nonetheless, the stability of the system is in danger. At 10 Myr, Planets d-e do lie below the approximate $\Delta > 9$ stability threshold; however, both pairs on either side of d-e are still relatively stable which may help stabilize the system. More importantly, the separation of planets b-c at 10 Myr skirts dangerously close, $\Delta = 3.8 \pm^{0.5}_{0.4}$, to the critical $\Delta > 2\sqrt{3}$ stability threshold. More detailed modeling needs to be done to assess the impact of mass loss on orbital stability; nonetheless, the $\Delta > 2\sqrt{3}$ stability threshold provides another strong reason to be skeptical of a water-poor super-Earth scenario for Kepler-11b.

The major caveat to this stability analysis is that we assume that all of the orbits are stationary even as the planets lose mass. This is motivated by Adams (2011), which showed that in the presence of a modest planetary magnetic field XUV driven mass loss from hot Jupiters tends to come out along the magnetic poles. Assuming that the magnetic field is sufficiently strong, dipolar, and perpendicular to the plane of the orbit, then mass loss won't have any impact on the orbit. In general however, the directionality of mass loss will be an extremely complicated problem determined by the interaction of the ionized hydrodynamic wind, the planetary magnetic field, and the stellar wind. Boué *et al.* (2012) showed that if the mass loss is directed in the plane of the orbit, then it can have a significant impact on both semi-major axis and eccentricity.

2.6 Chapter Conclusions

In order to better understand the structure, history, and formation of low-mass planets, we constructed coupled thermal evolution and mass loss models of water-poor super-Earths, water-worlds, and water-rich sub-Neptunes. The Kepler-11 system represents a new class of low-mass low-density planets that offers a unique test-bed for such models and gives us powerful insights on planet formation and evolution. Applying this understanding more broadly, we find a relation between a planet's mass, density, and its incident flux that matches the observed population. Moreover, this threshold can help constrain the properties of hundreds of planets. Our primary conclusions are:

- XUV-driven hydrogen mass loss coupled with planetary thermal evolution is a powerful tool in understanding the composition and formation of low-mass low-density planets.
- A coupled model is essential for this work, due to the much larger planetary radii in the past, when XUV fluxes were significantly higher.
- In situ formation of the Kepler-11 system is disfavored, instead it could be a system of water-rich sub-Neptunes that formed beyond the snow line.
- If Kepler-11b is a water-poor super-Earth then it likely formed with $\sim$ 90% H/He beyond 0.25 AU. We believe this is unlikely and instead show that Kepler-11 b-f all could have originated as water-rich sub-Neptunes with $\sim$ 20% H/He initially. If this is the case, Kepler-11b could have lost its H/He envelope and become a water-world today for a wide range of initial masses and compositions.

- There is a sharp observed threshold in incident flux vs. planet density times mass above which we do not find planets with H/He envelopes. To date, low-density planets have not been found above this threshold.

- This mass loss threshold is well reproduced by our coupled thermal evolution and mass loss models.

- This threshold can be used to provide limits on planet mass or radius for the large population of low-mass low-density planets without measured densities.

- In particular, we have identified promising *Kepler* targets for RV follow-up.

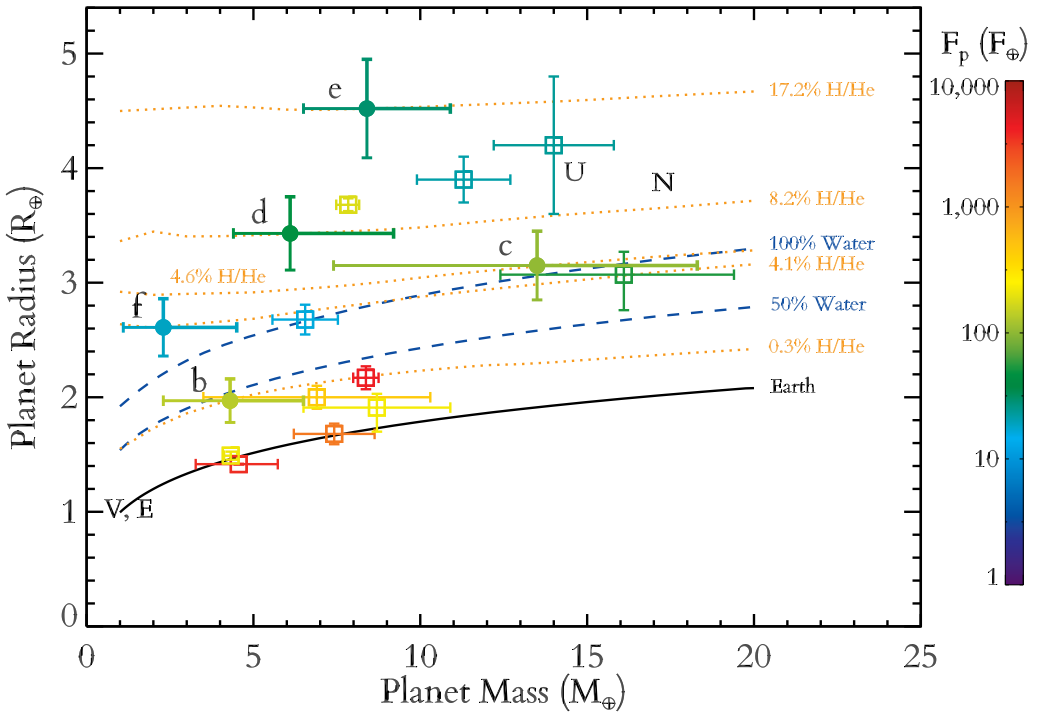

Figure 2.1 Radius vs. mass for transiting exoplanets with measured masses, along with curves for different compositions. Planets are color-coded by the incident bolometric flux they receive. Kepler-11 planets are shown by filled circles with letters indicating each planet. Other known exoplanets in this mass and radius range are shown by open squares. Solar system planets Earth, Venus, Uranus, and Neptune are shown by black letters. The solid black curve is for a Earth-like composition with 2/3 rock and 1/3 iron. All other curves use full thermal evolution calculations, assuming a volatile envelope atop a earth like core. The dashed blue curves are for 50% and 100% water by mass. The dotted orange curves are for H/He envelopes at 8 Gyr; each one is tailored to match a Kepler-11 planet and is computed at the appropriate flux and for that planet.

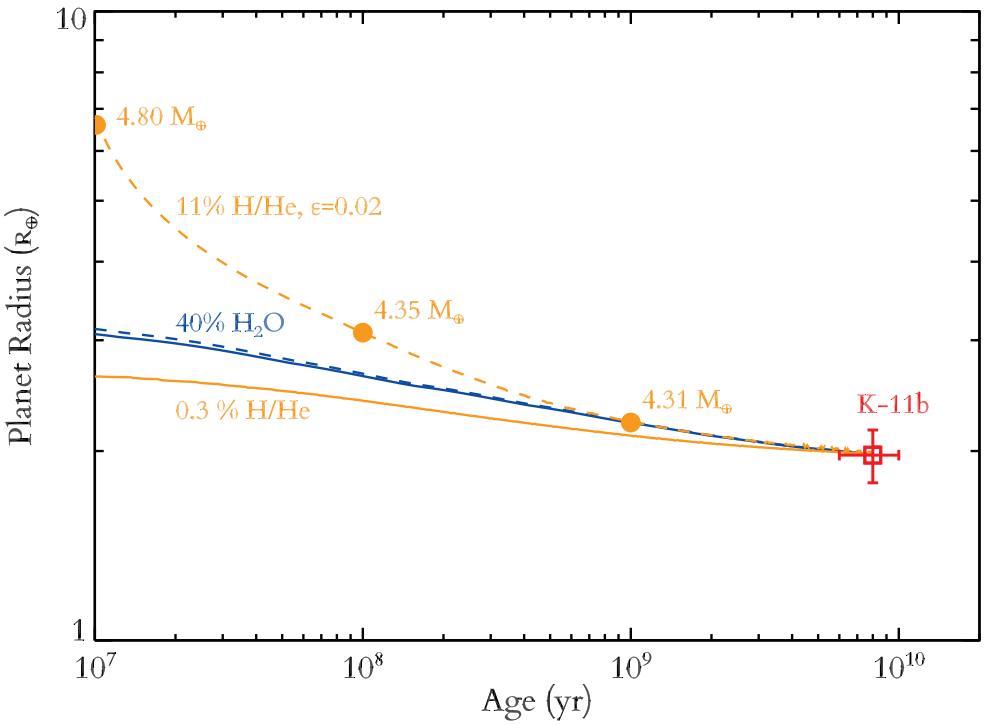

Figure 2.2 Radius vs. time for four example model runs that match the present day mass and radius of Kepler-11b. The blue curves show water-world models, while the orange curves show water-poor super-Earth models. Dashed lines are with mass loss, while solid are without. Both water-world models and the water-poor super-Earth model without mass loss show very similar cooling curves. Even with our standard efficiency of 10% the water models undergo only minor mass loss. Meanwhile, even with an efficiency 4× smaller the H/He model undergoes substantial mass loss. This model is initially 14% H/He and 5.0 $M_{\oplus}$. We have marked the masses for the H/He with mass loss model at 10 Myr, 100 Myr, and 1 Gyr. This also shows the large impact on radius that even a modest (compared to Figure 2.3) H/He envelope can have.

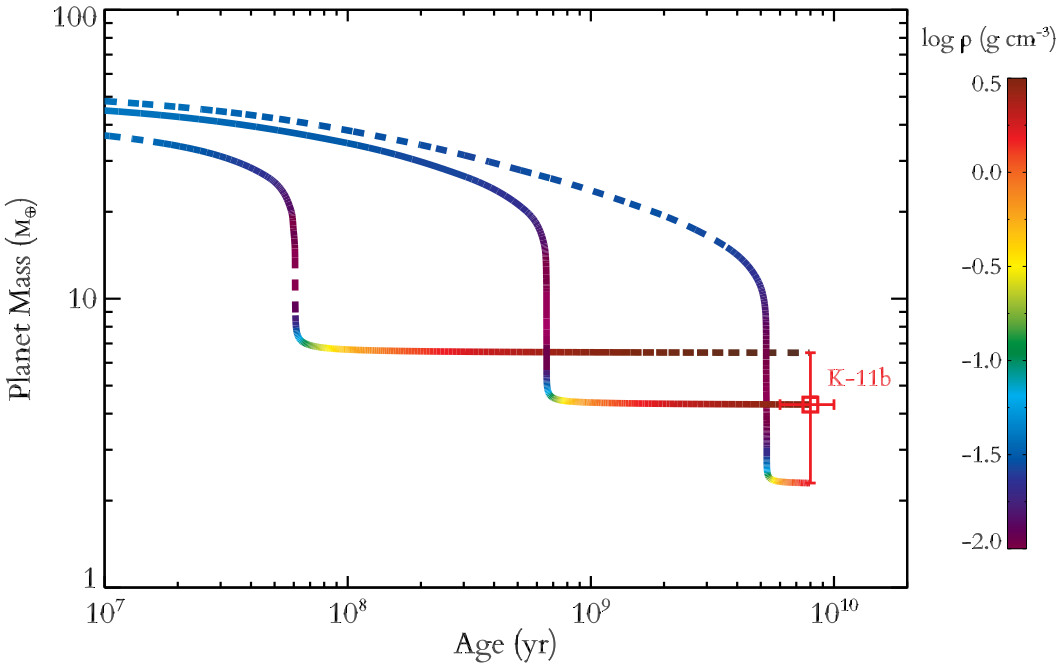

Figure 2.3 Mass vs. time with mass loss for three model runs that match the present day mass along with its 1σ range for Kepler-11b. All three models assume a water-poor super-Earth composition that is 0.3% H/He today. The curves are color-coded by log density. The solid line corresponds to the best fit current mass from TTV; the dashed lines correspond to the 1σ bounds. This demonstrates several features described in the text. The initial mass is actually lower if Kepler-11b is more massive today due to a correspondingly more massive core. There is a period of runaway mass loss during which the density actually declines slightly, and the timing of this period depends strongly on the mass of the rocky core.

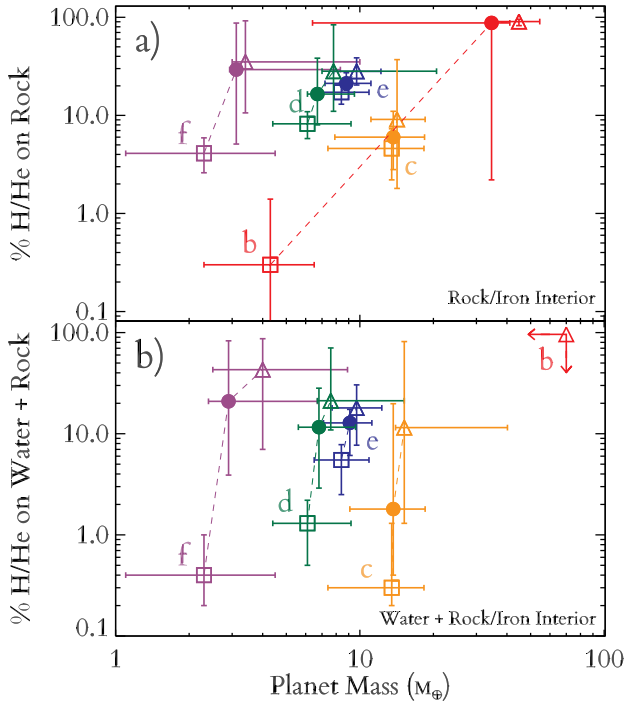

Figure 2.4 Composition vs. mass for models of Kepler-11 with mass loss. Panel a) shows the results for water-poor models with a H/He envelope atop a rock/iron core. Panel b) shows the results for water-rich models that also have a thick water layer in between. Each point shows the % H/He and mass predicted by our models at a given time. Each color indicates a particular planet as identified by the letters and connected by dashed lines. The open squares show the present day mass and composition as listed in table 2.1. The filled circles show the results at 100 Myr and the open triangles show the results at 10 Myr as listed in tables 2.2 and 2.3. Kepler-11b is extremely vulnerable to H/He mass loss, and would have been up to $\sim$ 90% H/He if it formed as a water-poor super-Earth. All five planets are consistent with having initially been water-rich sub-Neptunes with comparable amounts of rock and water and $\sim$20% of their mass in H/He.

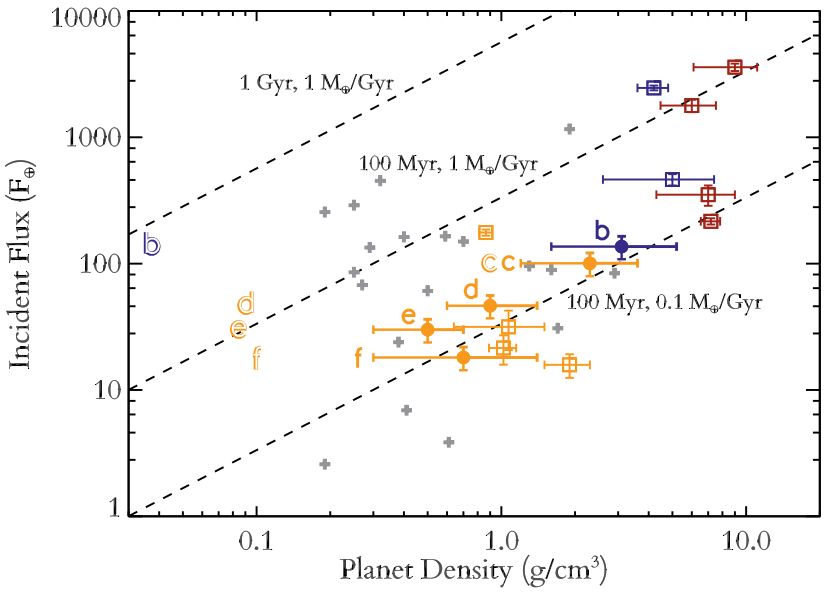

Figure 2.5 Bolometric flux at the top of the atmosphere, relative to the flux incident on Earth, vs. planet density. Once again, Kepler-11 planets are shown by filled circles with letters indicating each planet. Open squares show the other extrasolar planets included in Figure 2.1. Colors indicate possible compositions. Planets that could be rocky are red, those that could be water-worlds are blue, and those that must have H/He are orange. For comparison, the gray crosses show all other transiting planets with measured masses greater than 15 $M_\oplus$ and less than 100 $M_\oplus$. The dashed black lines show curves of constant mass loss for different mass loss rates and ages, assuming our standard mass loss efficiency of 20%. Finally, the shaded letters at the left indicate the densities for each Kepler-11 planet at 100 Myr predicted by our mass loss evolution models in Section 2.3.2.

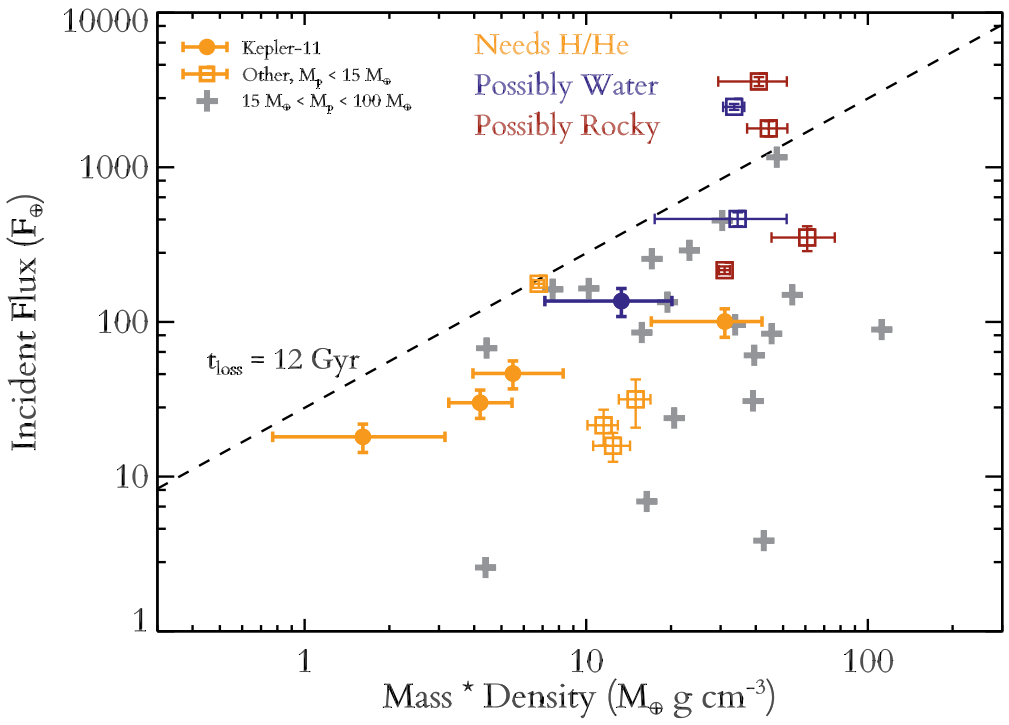

Figure 2.6 Similar to Figure 2.5 except here we have multiplied the x-axis by planet mass. Once again, Kepler-11 planets are shown by filled circles, while open squares show the other extrasolar planets included in Figure 2.1. Colors indicate possible compositions. Low mass planets that could be rocky are red, those that could be water-worlds are blue, and those that must have H/He are orange. For comparison, the gray crosses show all other transiting planets with measured masses greater than 15 $M_\oplus$ and less than 100 $M_\oplus$. There is a threshold in this diagram above which there are no observed transiting planets. Moreover, this threshold corresponds to a critical mass-loss timescale (see eq. 2.6), as shown by the dashed black line. We discuss this threshold in the context of XUV driven mass loss in section 2.4.

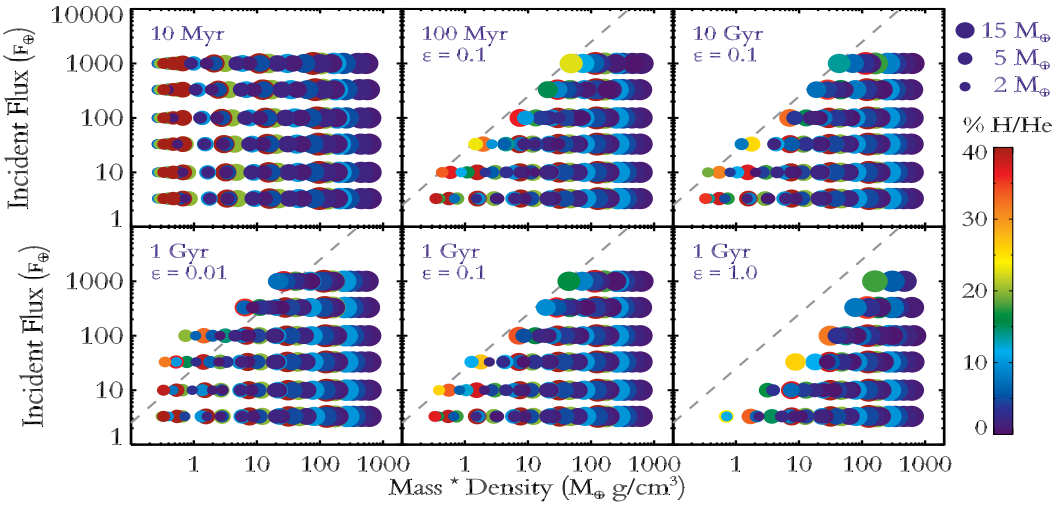

Figure 2.7 This shows the results of $\sim$ 1000 thermal evolution and mass loss model runs which reproduce the mass loss threshold seen in Figure 2.6. Each panel plots incident bolometric flux in $F_{\oplus}$ vs. planet density $\times$ mass for different ages and mass loss histories. Each point is sized according to its mass and colored according to its composition, assuming a H/He atmosphere atop an Earth-like core. The top left panel shows the initial distribution of the models before any mass loss has taken place. The other two top panels show results at 100 Myr and 10 Gyr for our standard mass loss efficiency (ϵ = 0.1). Meanwhile the bottom panels show the results at 1 Gyr for three different mass loss efficiencies ranging from extremely inefficient (ϵ = 0.01), to extremely efficient mass loss (ϵ = 1). As planets lose mass, the points shrink, move to the right, and become bluer. The dashed line in panels 2-6, is the same as the black dashed line in Figure 2.6 corresponding to critical mass loss timescale. The threshold in Figure 2.5 is well reproduced by models with ϵ = 0.1, which is also the approximate value implied by detailed models as discussed in Section 2.2.3.

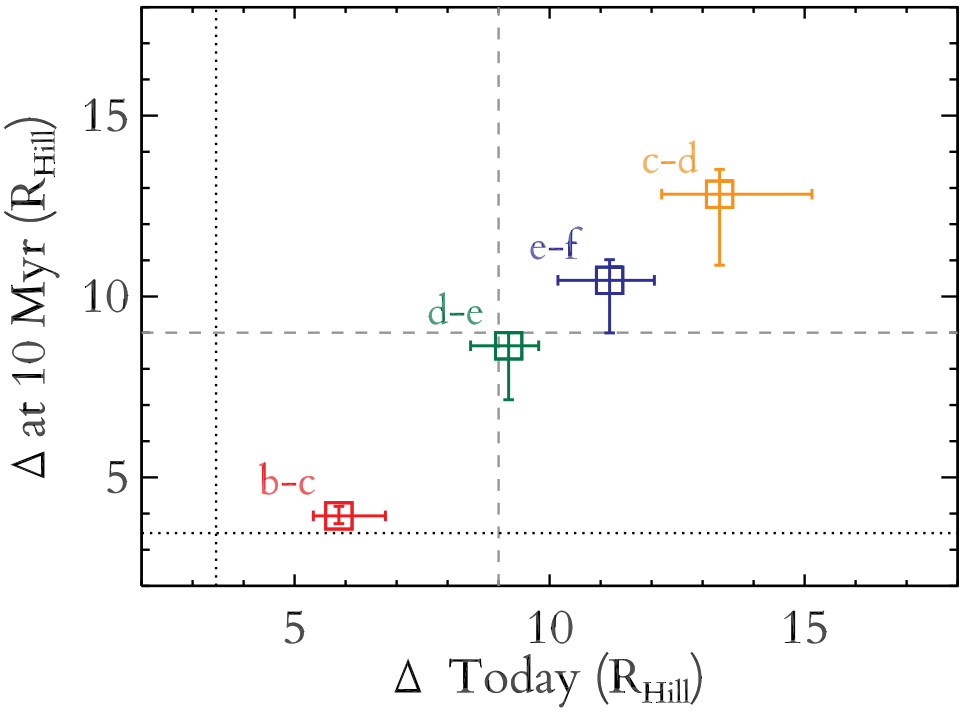

Figure 2.8 Separation between adjacent pairs of planets in Kepler-11, in terms of their mutual Hill spheres Δ. The x-axis shows the separations in terms of the current Hill spheres, while the y-axis shows the predicted Hill spheres when the system was 10 Myr old assuming a water-poor scenario and that the planets remained stationary. The dashed lines show the approximate $\Delta > 9$ stability threshold for five planet systems from Smith and Lissauer (2009). Likewise, the dotted lines show the $\Delta > 2\sqrt{3}$ stability threshold for two planet systems from Gladman (1993). Importantly, the b-c pair drops dangerously close to the $\Delta > 2\sqrt{3}$ critical threshold for dynamical stability in two-planet systems. This is another reason we disfavor a water-poor super-Earth scenario for Kepler-11b.

Chapter 3

The Role of Core Mass in Controlling Evaporation: The *Kepler* Radius Distribution and The Kepler-36 Density Dichotomy

3.1 Chapter Introduction

The Kepler-36 system (Carter *et al.*, 2012) is a fascinating case-study for theories of planet formation and evolution. It contains a closely spaced pair of super-Earth mass planets with periods of 13.8 and 16.2 days orbiting a slightly evolved 6.8 ± 1.0 Gyr old G1 sub-giant that is 2.9 times more luminous than the Sun. Although too faint for reliable radial velocity measurements, the system exhibits strong Transit Timing Variations (TTVs), which allowed the planet densities to be determined to better than 10% precision (Carter *et al.*, 2012). Surprisingly, despite their extremely similar orbits, the planets have densities that differ by almost an order of magnitude. The inner planet Kepler-36b has a mass of $4.5 \pm 0.3\ M_{\oplus}$ and a density of 7.2 ± 0.7

$\mathrm{g\,cm^{-3}}$, fully consistent with an Earth-like composition. Meanwhile the outer planet Kepler-36c has a mass of $8.1\pm^{0.6}_{0.5}\ M_\oplus$ but a density of only $0.87 \pm 0.05\ \mathrm{g\,cm^{-3}}$, meaning that it must have a substantial H/He envelope (Carter *et al.*, 2012).

This poses an interesting problem for theories of planet formation and evolution: how is it that two planets in the same system with very similar highly irradiated orbits arrived at such radically different densities today? One possibility is that the planets simply formed in very different environments. Models of core accretion show that it is much easier to accrete a substantial H/He envelope when the local disk temperature is lower (Ikoma and Hori, 2012). Perhaps Kepler-36b formed at or close to its current orbit while Kepler-36c formed substantially further out and migrated inwards (Ida and Lin, 2010).

However, another possibility is that the planets did form in similar environments, but that subsequent evolution has caused them to diverge. In particular, photo-evaporation due to extreme ultra-violet (XUV) heating can remove large amounts of hydrogen/helium from highly irradiated planets through hydrodynamic mass loss. Models of XUV-driven mass loss were first developed to study water loss from early Venus (Hunten, 1982; Kasting and Pollack, 1983), and hydrogen loss from the early Earth (Sekiya *et al.*, 1980; Watson *et al.*, 1981). These kinds of models were further developed to study mass loss from hot Jupiters (e.g., Lammer *et al.*, 2003; Yelle, 2004; Murray-Clay *et al.*, 2009), where there is clear evidence that atmospheric escape is an important physical process. This includes both trends in the population of hot Jupiters (Lecavelier Des Etangs, 2007; Hubbard *et al.*, 2007b,a; Davis and Wheatley, 2009; Ehrenreich and Désert, 2011) and direct detections of atmospheric escape (Vidal-Madjar *et al.*, 2003, 2004; Linsky *et al.*, 2010; Lecavelier Des Etangs *et al.*, 2010; Lecavelier des Etangs *et al.*, 2012;

Haswell *et al.*, 2012; Ehrenreich *et al.*, 2012). More recently, mass loss models have been used to study the new populations of super-Earths and sub-Neptunes being found by transiting surveys like CoRoT and *Kepler* (Jackson *et al.*, 2012; Owen and Jackson, 2012; Lopez *et al.*, 2012; Wu and Lithwick, 2013; Owen and Wu, 2013).

Recently, in Lopez *et al.* (2012) we showed that exoplanet compositions are subject to a photo-evaporation threshold. Observationally there are no planets with low bulk density and high incident flux, implying that low-mass planets with substantial H/He envelopes do not exist in this area of parameter space. Following Lecavelier Des Etangs (2007) who studied hot Jupiters, Lopez *et al.* (2012) were able to show that this threshold can naturally be explained as a critical mass loss timescale. Detailed models in Lopez *et al.* (2012), which include coupled thermal and mass loss evolution, reproduced this threshold with standard mass loss efficiencies. We further showed that many of the super-Earths and Neptunes found by the *Kepler* mission including those in Kepler-11(Lissauer *et al.*, 2011a) and Kepler-36 lie along this threshold, indicating that these planets may have undergone substantial mass loss in the past. Here we show that photo-evaporation can be controlled by the mass of a planet's rock/iron core and that this provides a natural explanation for the divergent densities of Kepler-36 b&c. This process allows both planets to form with similar compositions and in similar environments before being sculpted by their different mass loss histories.

In addition to detailed studies of individual systems like Kepler-36, there is a growing body of literature examining the overall distribution of *Kepler* planet candidates. Detailed studies of planet occurrence rates by Petigura *et al.* (2013b) and Fressin *et al.* (2013) have recently shown that is a sharp drop off in the frequency of planets above $\gtrsim$2.8 $R_\oplus$, at least within 50 and

85 days respectively. In contrast, planets with radii $\lesssim$2.8 $R_\oplus$ seem to be equally common. Likewise, Howard *et al.* (2012) and Youdin (2011) showed that there is a drop off in the frequency of candidates at extremely short periods $\lesssim$10 days; moreover, this drop off is particularly acute for sub-Neptune sized planets. In multi-planet systems, Ciardi *et al.* (2013) showed that there is a tendency for outer planets to be larger than inner planets in the same system, particularly when those planets are smaller than Neptune and on orbits $\lesssim$20 days.

Models have shown that photo-evaporation and thermal evolution can significantly alter the H/He inventories of super-Earth and sub-Neptune sized planets (Baraffe *et al.*, 2006; Lopez *et al.*, 2012; Owen and Wu, 2013). Moreover, planet structure models have shown that changing the mass of a planet's H/He envelope has a large impact on its resulting radius (Rogers and Seager, 2010b; Lopez *et al.*, 2012). As a result, models of thermal and mass loss evolution can shed light on many of the observed trends in the radius distribution of *Kepler* planet candidates.

3.2 Our Model

For this work, we have used the coupled thermal evolution and mass loss model presented in Lopez *et al.* (2012), where additional model details can be found. Similar models have been used to track the coupled evolution of rocky super-Earths (e.g, Jackson *et al.*, 2010; Valencia *et al.*, 2010; Nettelmann *et al.*, 2011), hot Neptunes (e.g, Baraffe *et al.*, 2006), and hot Jupiters (e.g, Baraffe *et al.*, 2004, 2005; Hubbard *et al.*, 2007b,a). Beginning shortly after the end of planet formation, we track planetary mass and radius as a function of age. The use of

coupled model is essential, because planetary radii are largest at young ages, when stellar XUV fluxes are highest.

At a given age, a model is defined by the mass of its heavy element core, the mass of its H/He envelope, the amount of incident radiation it receives, and the internal entropy of its H/He envelope. Here we assume an isothermal rock/iron core with an Earth-like 2:1 rock/iron ratio, using the ANEOS olivine (Thompson, 1990) and SESAME 2140 Fe (Lyon and Johnson, 1992) equations of state (EOS). For the H/He envelope we assume a fully adiabatic interior using the Saumon *et al.* (1995) EOS.

In order to quantitatively evaluate the cooling and contraction of the H/He envelope, we use a model atmosphere grid over a range of surface gravities and intrinsic fluxes. These grids relate the surface gravity and internal specific entropy to the intrinsic flux emitted for a given model. These radiative transfer models are computed at a Uranus and Neptune-like $50\times$ solar metallicity atmosphere using the methods described in Fortney *et al.* (2007) and Nettelmann *et al.* (2011). These atmosphere models are fully non-gray, i.e. wavelength dependent radiative transfer is performed rather than simply assuming a single infrared opacity. In addition, we include heating from radioactive decay in the rock/iron core and the delay in cooling due to the core's heat capacity. In order to correctly determine a planet's mass loss history, it is vital to include these thermal evolution effects, since these will strongly affect a planet's radius over time. Radius, in turn, has a large impact on the mass loss rate as seen in Equation 3.1.

Close-in planets like those in Kepler-36 are highly irradiated by extreme ultraviolet (EUV) and X-ray photons. These photons photo-ionize atomic hydrogen high in a planet's atmosphere, which in turn produces significant heating (Hunten, 1982). If this heating is large

enough, it can generate a hydrodynamic wind that is capable of removing significant mass. We couple this XUV-driven mass loss to our thermal evolution models using the energy-limited approximation (Watson *et al.*, 1981). This allows a relatively simple analytic description of mass loss rates.

$$\dot{M}_{\text{e–lim}} \approx \frac{\epsilon \pi F_{\text{XUV}} R_{\text{XUV}}^3}{G M_{\text{p}} K_{\text{tide}}} \tag{3.1}$$

$$K_{\text{tide}} = (1 - \frac{3}{2\xi} + \frac{1}{2\xi^3}) \tag{3.2}$$

$$\xi = \frac{R_{\text{Hill}}}{R_{\text{XUV}}} \tag{3.3}$$

Equation (3.1) describes our estimate of the mass loss rate based on the formulation from Erkaev *et al.* (2007). F_{XUV} is the time-dependent total flux between $1-1200$ angstroms, which is given by Ribas *et al.* (2005) as a function of age for Sun-like stars. R_{XUV} is the planetary radius at which the atmosphere becomes optically thick to XUV photons, which occurs at pressures around a nanobar (Murray-Clay *et al.*, 2009). K_{tide} is a correction factor that accounts for the fact that mass only needs to reach the Hill radius to escape (Lecavelier des Etangs *et al.*, 2004; Erkaev *et al.*, 2007). Finally, ϵ is an efficiency factor that parametrizes the fraction of the incident XUV flux that is converted into usable work. For this work we use $\epsilon = 0.1$ based on the observed photo-evaporation threshold described in Lopez *et al.* (2012). This value is similar to the efficiencies found by Owen and Jackson (2012). Using more sophisticated photo-evaporation models for hot-Neptunes they found mass loss efficiencies that varied from 0.05 to 0.2.

It is important to note, however, that efficiencies of order $\sim$10% are only relevant for planets on orbits similar to those found in Kepler-36 or Kepler-11, i.e. orbits of $\sim 10-50$ days for Sun-like stars. For more irradiated planets on $\sim$1-3 day orbits, the mass loss efficiency will be significantly lower due to additional cooling from recombination, while further out in the habitable zone the evaporation is no longer hydrodynamic (Murray-Clay *et al.*, 2009; Owen and Jackson, 2012). Finaly, we make an additional conservative modeling choice by starting mass loss at an age of 10 Myr, since stellar XUV fluxes and planetary radii post-formation are not well understood at even earlier times.

3.3 Kepler-36: Explained by Mass Loss?

Before we determine the possible mass loss histories of Kepler-36b & c, we must first examine their present day compositions. For Kepler-36b, this is relatively straightforward since its density is consistent with a rocky compositions without a H/He envelope. In this case we find that it should be $25.9\pm^{9.1}_{4.3}$ % iron, consistent with an Earth-like rock/iron ratio. This is derived by matching the observed mass and radius with our structure models in the absence of any H/He or water envelope. Likewise, the error bars include the observed 1σ uncertainties in mass and radius. In contrast, Kepler-36c has much lower density and requires a substantial H/He envelope to explain its radius. To estimate its present day composition, we ran our thermal evolution models in the absence of any mass loss. To explain its current radius Kepler-36c must be 8.6 ± 1.3% H/He, assuming an Earth-like core. To calculate the error bars we varied the planetary albedo from 0-0.8 and the heat capacity of the rocky core from 0.5-1.0 $\mathrm{JK^{-1}\,g^{-1}}$.

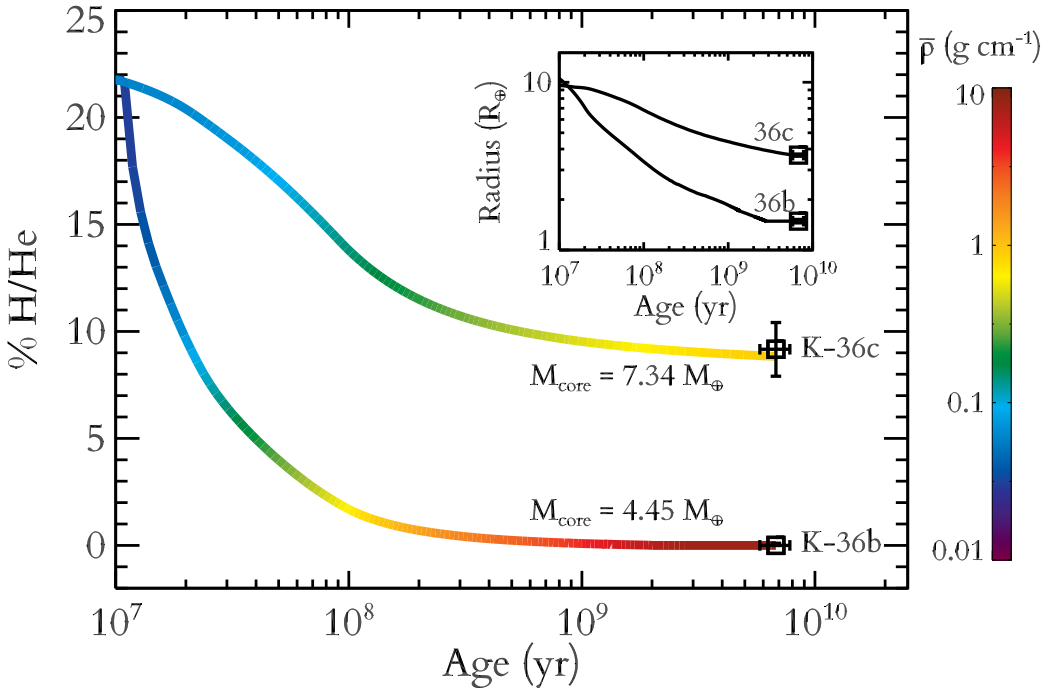

Figure 3.1 Possible mass loss histories for Kepler-36b & c. The curves plot the mass fraction in the H/He envelope vs. time, while the colors indicate each planet's density at a given age. Likewise the inset shows the radius evolution of each planet. The black points on the right hand side indicate the current compositions of Kepler-36b & c, while the text lists the rock/iron mass predicted for each planet. Currently, Kepler-36c requires $\sim$ 8% of its mass in H/He, while Kepler-36b is consistent with an Earth-like composition. Nonetheless it is possible both planets formed with $\sim$ 22% H/He, but subsequent mass loss has distinguished them due to differences in their core masses. This provides a natural explanation for the large density contrast seen today in this system. Such evolutionary histories are a generic outcome of our evolution calculations, with a wide range of initial H/He masses and mass loss efficiencies.

We also included the observed uncertainties in mass, radius, current age, and incident flux. In addition, for Kepler-36b we can set an upper limit on the presence of any H/He envelope. It must be $< 0.1\%$ H/He, assuming a maximally iron rich core (Marcus *et al.*, 2010).

By knowing the present day compositions, we can determine the mass of each planet's core. For Kepler-36b it is simply the observed mass from TTVs, $4.5 \pm 0.3\ M_{\oplus}$, while for Kepler-36c it is $7.4 \pm^{0.5}_{0.4}\ M_{\oplus}$. Using these core masses, we ran fully coupled models including both mass loss and thermal evolution, in order to determine the initial composition each planet had after formation. To ensure consistency, we check that these models with mass loss are still able to reproduce present day radius.

Figure 3.1 shows the results of our coupled mass and thermal evolution models for both planets in the Kepler-36 system. The model assumes that both planets formed at their current orbits with the same initial H/He mass fraction. Each curve plots the fraction of each planet's mass in the H/He envelope vs. age, while the colors indicate the planet's density at that age. The black points at the right indicate the current age and composition of the Kepler-36 planets. We also show the radius evolution of both planets in an inset. Such large radii at young ages are a generic outcome of evolution models, since the H/He envelopes are warm and are not degenerate. See Mordasini *et al.* (2012) for a wider exploration of planetary radii for low-mass planets with H/He envelopes as a function of age.

At 10 Myr, when we start photo-evaporation both planets are $\sim 10\ R_{\oplus}$. Kepler-36b rapidly contracts as it loses mass and is down to $\sim 3\ R_{\oplus}$ by 100 Myr. Kepler-36c is also vulnerable to mass loss. To have retained its current 8% of H/He Kepler-36c would need to have been formed with 22% H/He at 10 Myr and a mass of 9.4 $M_{\oplus}$. Since Kepler-36b is

consistent with no H/He envelope today, we can only set upper limits on its initial composition. However, if we assume that it formed with the same initial 22% H/He as 36c, then it would have lost its entire H/He envelope by the time it was 2 Gyr old. Thus the large discrepancy in the present day densities of the two planets, can naturally be explained by the fact that Kepler-36b is significantly more vulnerable to mass loss than Kepler-36c.

However, this leads to the question, why is Kepler-36b so much more vulnerable than its neighbor? Although it does receive $\approx 24\%$ more incident radiation than 36c, this alone produces far too small an effect to explain the necessary difference in mass loss histories (Carter *et al.*, 2012). Instead, it is caused almost entirely by the difference in the masses of the two planets. As shown in Lopez *et al.* (2012), planetary radius at fixed composition is relatively flat as a function of mass for $\sim 1-20\ M_\oplus$ planets with significant H/He envelopes. As a result, density for these planets goes roughly like the mass. Since the mass loss rate is proportional to the inverse of the of the average density $1/\bar{\rho}$, the mass loss timescale goes like $M_\mathrm{p} \times \bar{\rho}$ or M_p^2.

However, rather than considering a planet's total mass today, it is useful to consider simply its heavy element mass today. Unlike the current total mass and bulk density, the heavy element mass should remain essentially constant as a planet contracts and loses its H/He envelope, providing a useful tool for estimating a planet's mass loss rate throughout its history. For simplicity, we assume here that the heavy elements are locked in a silicate/iron core, although it is also possible that some of these metals could be mixed into the H/He. Of course at a given composition, the mass of this rocky core M_core is proportional to the total mass M_p. Thus the mass loss timescale t_ml goes roughly like M_core^2. We calculate that Kepler-36c's rocky core should be 65% more massive than that of Kepler-36b. As a result, we predict that the mass

loss timescale for Kepler-36b was ~ 3 times shorter than for Kepler-36c.

In Figure 3.1, we have presented one possible scenario for the evolution of Kepler-36. These results are insensitive to any reasonable variation in the mass loss efficiency or the initial envelope fractions. For mass loss efficiencies significantly less than 0.1, it is not possible to construct a scenario where both planets b and c started out with identical envelope fractions. Nonetheless, even for lower efficiencies it is still quite possible that both planets started off with substantial amounts of H/He but that Kepler-36b lost its gaseous envelope to mass loss.

3.4 The Role of Core Mass

3.4.1 A Parameter Study

The Kepler-36 system clearly demonstrates that the mass loss evolution of planet depends on more than just the incident XUV flux that a planet receives. In Lopez *et al.* (2012) we showed that there is a threshold in the observed population of transiting planets with measured densities and H/He envelopes. This threshold is well described by a critical mass loss timescale:

$$t_{\rm loss} = \frac{GM_{\rm p}^2}{\pi \epsilon R_{\rm p}^3 F_{\rm XUV,E100}} \frac{F_\oplus}{F_{\rm p}} \approx 12 Gyr \tag{3.4}$$

Here $F_{\rm p}$ is the incident bolometric flux that a planet receives from its parent star, $F_\oplus$ is the current bolometric flux that the Earth receives from the Sun, and $F_{\rm XUV,E100} = 504$ erg s^{-1} cm^{-2} is the XUV flux at the Earth when it was 100 Myr old. In Lopez *et al.* (2012) we then performed a simple parameter study to show that this critical mass loss timescale was well reproduced by our coupled thermal and mass loss evolution models.

In order to better understand in detail how mass loss evolution depends on the mass of a planet's rocky core as well as the incident flux and mass loss efficiency, we greatly expanded the parameter study from Chapter 2. Beginning at 10 Myr, we ran over 6000 evolution models varying the incident flux, core mass, composition, and mass loss efficiency. We then recorded the radius, mass, and composition at different ages. The grid of initial conditions was evenly spaced logarithmically, with incident flux varying from $1-1000\ F_{\oplus}$, the rocky core mass from 1-64 $M_{\oplus}$, the initial H/He mass fraction from 0.1-80% H/He, and the mass loss efficiency from 0.01-1.0. Figure 3.2 summarizes the results. In each panel we have plotted the incident flux vs. the core mass. Each circle corresponds to an individual planet that is color-coded by the fraction of its initial H/He envelope that is lost by the age indicated on the panel. At each point we overplotted multiple models with different initial compositions, in each case the size of the circle corresponds to the initial mass fraction in the H/He envelope. Finally the different panels compare results at different times and for different mass loss efficiencies. The top three panels show the results using our standard mass-loss efficiency at 50 Myr, 100 Myr, and 1 Gyr. Meanwhile the bottom three panels show the results at 5 Gyr, a typical age for *Kepler* systems, for mass loss efficiencies of 0.01, 0.1, and 1.0.

Clearly, the mass loss history of a planet depends strongly on both the incident flux and the mass of the rock/iron core. The indigo models in the lower right of each panel have lost a negligible fraction of their initial H/He envelope. These models have either relatively massive cores and/or receive little incident flux and so mass loss is unimportant to the evolution of planets in this part of parameter space. On the other hand, the dark red models in the upper left with low mass cores and high incident flux have completely lost their entire H/He envelopes.

This region of parameter space should be filled with highly irradiated rocky planets like CoRoT-7b and Kepler-10b (Léger *et al.*, 2009; Queloz *et al.*, 2009; Batalha *et al.*, 2011).

In between there is a transition region where mass loss is important but at least some of the models are able to retain a H/He envelope. This transition region is relatively narrow, spanning less than an order of magnitude in incident flux for a given core mass. For models in this transition region the relation between the size of the initial H/He envelope and the fraction of the envelope lost is extremely complicated and not always monotonic. There is trade off between the fact that planets with small initial envelopes have relatively little mass in those envelopes to lose, and the fact that planets with large initial envelopes have larger initial radii and therefore experience much higher mass loss rates. For models at early times and/or low mass loss efficiency, the fraction of the envelope lost increases with the initial envelope fraction. On the other hand, at late times and/or high mass loss efficiencies it is the planets with small initial envelopes that are most vulnerable. As a result, much of the scatter in characterizing this transition region is determined by variations in the initial H/He envelope fraction.

In addition, the bottom three panels of Figure 3.2 make it clear that the location of this mass loss transition region depends on the mass loss efficiency. This makes sense; it is of course easier to remove more mass if the photo-evaporation is more efficient. Below, we will show that this behavior can also be well approximated as a power-law. In contrast, the behavior with age is more like an exponential decay. Most of the mass is lost in the first 100 Myr, while a comparison of the top right and bottom middle panels shows that relatively little mass is lost after 1 Gyr.

Likewise, in each panel the threshold for significant mass loss can be described as a

power-law. If we define the criterion for significant mass loss to be the evaporation of half the initial H/He envelope by several Gyr, then at a given age and mass loss efficiency this defines a power-law relation between the rock/iron core mass and the threshold incident flux needed for substantial mass loss. The slope of this power-law is roughly $F_{\rm th} \propto M_{\rm core}^{2.4}$, as discussed in section 3.4.3.

3.4.2 Why Core Mass?

The virtue of studying mass loss trends vs. core mass is that it allows us to define a narrow band of parameter space in Figure 3.2 where the precise details of mass loss are important with relatively little scatter due to variations in the initial H/He envelope mass. The currently observable planet properties, such as present day planet mass, radius, and density, are themselves highly dependent on the mass loss history and therefore on other unknown variables like the mass loss efficiency and initial composition. This makes it difficult to separate the effects of variations in current planet mass from variations in other parameters like incident flux or mass loss efficiency. On the other hand core mass represents an initial condition which is constant throughout a planet's mass loss history.

Rather than core mass we could alternatively choose to study trends against other theoretical parameters like the initial envelope mass or initial total mass after formation. Like core mass, these parameters are independent of any subsequent mass loss evolution; however, in our models these parameters also less adept at predicting that mass loss evolution. In Figure 3.3 we show how $f_{\rm lost}$, the fraction of a planet's initial H/He envelope that is lost, depends on the core mass, the initial envelope mass, and the total mass. Each of the different curves is for a

different initial composition $f_{\rm envelope}$ varying from 1-60% H/He. All the models are computed at 100 $F_{\oplus}$, assume ϵ = 0.1, start at 10 Myr, and end at 5 Gyr.

Ideally we want a parameter that minimizes the scatter between models with different initial compositions. Initial composition is not directly observable, and determining a planet's mass loss history is a much more model-dependent exercise than determining its current composition. For observed planets like those in Kepler-36, it is possible to tightly constrain the mass in a H/He envelope, even without the coupled thermal evolution models used here (Rogers and Seager, 2010b). Moreover, as we show in Figures 3.4-3.7, trends with composition are complicated and cannot be described by a simple power-law. Thus parameters that minimize the scatter between models with different initial compositions are much better predictors of mass loss evolution. Comparing panels a) and b) in Figure 3.3, it is clear that plotting $f_{\rm lost}$ vs. core mass produces vastly less scatter than plotting $f_{\rm lost}$ vs. initial envelope mass. In panel c) we see that initial total mass is a reasonable predictor of $f_{\rm lost}$, but with about twice as much scatter as in panel a). Unique among a planet's properties, $M_{\rm core}$ is unchanged throughout a planet's evolution, is relatively model independent, and is a strong predictor of mass loss evolution.

3.4.3 Scaling Relations for Coupled Mass Loss Evolution

In order to quantify the dependency of mass loss on initial conditions, we examine how the location of the mass loss transition region varies with each variable independently. This allows us to understand the qualitative behavior of our complete model in terms of a few simple scaling relations. Such relations can be used for quick and relatively accurate estimates of the importance of mass loss for detected planets.

We start by defining $F_{\rm th}$ as the threshold flux for a model with a given core mass, mass loss efficiency, age, and initial composition to lose half of its initial H/He envelope. Holding all other variables fixed we examine how $F_{\rm th}$ varies with each parameter and try fitting a power-law relation. We then vary the other parameters across our entire parameter study and examine the scatter in these power-law fits. The dependence of $F_{\rm th}$ on $M_{\rm core}$, ϵ, and $f_{\rm lost}$ (the fraction of the initial H/He envelope that is lost) are all well fit by power-laws. As we previously described, the age dependence can be described as an exponential decay. For a 1 $M_\oplus$ core and $\epsilon = 0.1$, the best fit exponential decay is:

$$F_{\rm th} \sim \exp\left(-(t - 140\ {\rm Myr})/80\ {\rm Myr}\right) F_\oplus + 3.4 F_\oplus \tag{3.5}$$

Meanwhile for systems older than 1 Gyr, age dependence is unimportant, allowing us to study $F_{\rm th}$ independently of age.

Figure 3.4 shows in detail how the threshold flux and the amount of H/He lost depend on each variable in our parameter study according to our thermal and mass loss evolution model. For clarity we have picked representative values for the core mass, mass loss efficiency, and the initial composition, but the results shown are generalizable across the entire parameter space. The default values correspond roughly to those for Kepler-36c: an 8 $M_\oplus$ core, $\epsilon = 0.1$, and an initial composition of 20% H/He. Likewise, we choose models where 50% of a planet's initial envelope has been lost. We then vary $M_{\rm core}$, ϵ, and composition one at a time. For clarity, in each panel we list the variables that are being held constant.

In Figure 3.4a we examine how $F_{\rm th}$ depends on $M_{\rm core}$. This is well described by the

over-plotted power-law with $F_{\rm th} \propto M_{\rm core}^{2.4}$. This power-law is closely related to the critical photo-evaporation timescale that we described in Lopez *et al.* (2012), where the mass loss timescale $t_{\rm ml}$ goes like $M_{\rm p}\rho/F_{\rm p}$. This corresponds to the transition region in Figure 3.2. Because super-Earths and sub-Neptunes contain most of their mass in a rock/iron core, ρ, $M_{\rm p}$, and $M_{\rm core}$ all correlate strongly with each other, which implies that $F_{\rm th} \propto M_{\rm p}\bar{\rho} \propto M_{\rm core}^2$. Our fitted power-law, $F_{\rm th} \propto M_{\rm core}^{2.4}$, is slightly steeper than the simple $M_{\rm p}^2$ dependence we would expect analytically. The difference is due to the slight dependence of radius on core mass.

Likewise in Figure 3.4b we examine how $F_{\rm th}$ depends on ϵ. This is also well fit by a power-law, however it is intriguing that the dependence on ϵ is not quite inversely linear as it would be in a simple mass loss timescale. This is one of the effects of coupling mass loss and thermal evolution. All other things being equal, as the mass loss efficiency increases, the mass loss timescale becomes shorter while the thermal cooling timescale is relatively constant. As a result, the radius decreases more slowly as mass is lost, meaning that slightly more mass will be lost over a planet's history. This means that $f_{\rm lost}$ increases more than linearly with ϵ. In turn this means that for fixed $f_{\rm lost}$, $F_{\rm th}$ decreases less than linearly with ϵ. We can summarize both these trends in a single equation:

$$F_{\rm th} = 0.5 F_\oplus \left(\frac{M_{\rm core}}{M_\oplus}\right)^{2.4\pm0.4} \left(\frac{\epsilon}{0.1}\right)^{-0.7\pm0.1} \tag{3.6}$$

Equation (3.6) describes the results of our power-law fits for the location of $F_{\rm th}$. This is the incident flux a planet needs to receive from its parent star to remove half a planet's initial H/He envelope over the planet's lifetime, as a function of core mass $M_{\rm core}$, photo-evaporation

efficiency ϵ, and the flux that the Earth receives from the Sun $F_{\oplus}$. This was derived by fitting to all the models in our parameter study and the error bars correspond to the 1σ errors in those fits. Unfortunately, the dependence on initial composition is significantly more complicated and cannot be described by a simple power-law.

In Figure 3.4c we plot $F_{\rm th}$ against the initial mass fraction in the H/He envelope at 10 Myr. For modest initial H/He envelopes, up to $\sim 60\%$ of the planet's total mass, increasing the H/He mass does not significantly affect $F_{\rm th}$. However, above this point the envelope's self gravity becomes sufficiently strong that density increases rapidly and it becomes increasingly difficult to remove any mass. At the same time, since these planets have such massive envelopes, removing a few Earth masses of H/He has a much smaller impact on their overall composition. Figure 3.5 shows the other main effect of varying the initial composition. Here we show how the $M_{\rm core}-F_{\rm th}$ power-law index from Figure 3.4a depends on the initial composition. In general, as we increase the initial envelope mass, the radius-core mass relation becomes slightly steeper leading to a steepening of the $M_{\rm core}-F_{\rm th}$ relation.

In Figure 3.6 we complete the picture by showing how the amount of mass lost depends on all these aspects. We plot $f_{\rm lost}$, the fraction of the initial envelope that is stripped after 5 Gyr, vs. the ratio of the incident flux and the threshold flux described by equation (3.6). The relation is roughly linear as described by equation (3.7), where if $f_{\rm lost} \geq 1$ then the planet is completely stripped.

$$f_{\rm lost} = 0.5 \left(\frac{F_{\rm p}}{F_{\rm th}} \right)^{1.1 \pm 0.3} \tag{3.7}$$

Finally, in Figure 3.7 we examine the quality of these simple analytic approximations compared to full results of our actual models. Here we plot the ratio of our full model and the analytic results of equations (3.6) and (3.7) vs. the initial composition. The error bars represent the 1σ scatter due to variations in $M_{\rm core}$, ϵ, and $f_{\rm lost}$. For initial compositions that are less then $\sim 60\%$ H/He, the two generally agree with each other to within a factor of 2. For more massive initial envelopes, the analytic description breaks down and overstates a planet's vulnerability to mass loss. Also, it is important to keep in mind that these fitting equations are only rough approximations of the fully coupled evolution models and should not be used to make detailed predictions for individual planets. Nonetheless, these equations are valuable in understanding the qualitative behavior of our complete model and in making statistical comparisons to large populations of planets.

3.4.4 Comparison to Observed Population

Figures 3.2 and 3.4 make a clear prediction about which planets should be most vulnerable to mass loss. In addition to the incident XUV flux that a planet receives, its mass loss history should depend strongly on the mass of its rock/iron core. Planets that are either highly irradiated or have low mass cores are more vulnerable to losing any primordial H/He envelope. Thus we expect that we should not find planets with H/He envelopes above the $F_{\rm th} - M_{\rm core}$ threshold relation in equation (3.6). Any planets that are well above this relation should either be rocky, or water worlds which are less vulnerable to mass loss (Lopez *et al.*, 2012), or have H/He envelopes so large that equations (3.6) and (3.7) breakdown.

Figure 3.8 shows incident flux and core mass for all observed transiting planets with

well defined masses less than 100 $M_\oplus$ and radii less than 1.1 R_J from exoplanets.org (Wright *et al.*, 2011). Two planets were removed by the radius cut since they are known to be inflated and it is impossible to accurately determine a heavy element mass for these planets. To calculate core masses for the other 29 planets we ran water-free thermal evolution models without mass loss for each planet. The error bars on $M_{\rm core}$ include the observed uncertainties on mass, radius, and age as well as theoretical uncertainties on the iron fraction and thermal properties of the rocky core (Lopez *et al.*, 2012). Each planet is color-coded by its current H/He envelope fraction. The red-brown open circles are planets that are consistent with being rocky today. The dashed black line shows the $F_{\rm th} - M_{\rm core}$ relation from equation (3.6) scaled up by a factor of two so that equation (3.7) predicts complete stripping rather than only removing half the initial H/He envelope. Although the uncertainties are large, all the planets with substantial H/He envelopes are consistent with being to the right of this threshold. Of the six planets that lie to the left of the threshold, three (Kepler-10b, CoRoT-7b, and Kepler-20b) are consistent with being rocky and the other three with being water worlds (55 Cancri e, Kepler-18b, Kepler-20c).

3.5 Effects on Planet Radii

3.5.1 Trends in the Radius-Flux Distribution?

Thus far we have examined the effects of thermal and mass loss evolution on planet mass and composition. However, for the vast majority of *Kepler* candidates neither of these can be determined. As a result it is worth examining the predictions that our parameter study makes for planet radii. Figure 3.9 shows the radius-flux distribution of the models in our parameter

study after 10 Gyr of thermal and mass loss evolution. As a reminder, we ran models on a log uniform grid of incident flux, core mass, and initial envelope fraction. Points show individual models colored by their final H/He fractions while the grayscale boxes show the density of points in the distribution. In order to directly compare with other recent studies described below, we limited ourselves to core masses $<$15 $M_{\oplus}$, which also corresponds to the high end of core masses that will trigger runaway accretion (Movshovitz *et al.*, 2010). Modest variations of the maximum core mass, from 10-20 $M_{\oplus}$, do not qualitatively change any of the results described below. Planets with more massive cores, will have likely undergone runaway accretion and have final radii $>$ 4 $R_{\oplus}$. In addition to varying the core mass, initial envelope fraction, and incident flux, we have also varied the iron fraction of the rocky core since this will smear out any trends with radius. We varied the iron fraction uniformly from pure silicate rock, to the maximum iron fraction allowed by collisional stripping, $\sim$60-80% in this mass range (Marcus *et al.*, 2010). For simplicity we restricted ourselves to only a single age and our standard mass loss efficiency 0.1.

Our parameter study here is not meant to produce a realistic radius-flux distribution. Our choice of a log uniform distribution in core mass, envelope fraction, and incident flux is meant to effectively probe the range of possible models. Nonetheless there are key features in Figure 3.9 that should be observable in the flux-radius distribution of *Kepler* candidates. First and foremost, there should be a decline in the rate of sub-Neptune sized planets, here defined as 1.8-4.0 $R_{\oplus}$, at high incident fluxes due to photo-evaporation. In particular, these planets should become comparatively rare for $F_{\rm p} \gtrsim 100\ F_{\oplus}$, which corresponds to periods $\lesssim$10 days. Such an effect may have already been seen by Howard *et al.* (2012) and Youdin (2011). At the same

time there should be a corresponding increase in the frequency of rocky planets with R_p <1.8 $R_\oplus$, due to the large number of stripped cores.

Owen and Wu (2013) recently performed a similar parameter study and predicted that there should be a significant gap in the radius distribution with few planets between 1.5 and 2.5 $R_\oplus$. The origin of this gap is easy to understand. Planets in this size range will typically be ∼0.5% H/He. Such small envelopes are highly vulnerable to photo-evaporation; even tiny mass loss rates $\sim 0.01\ M_\oplus\, Gyr^{-1}$ will be more than sufficient to strip these planets. Moreover, planets that formed with more substantial initial envelopes are unlikely to end up in this part of parameter space. This behavior was discussed at length in the context of evolution models for Kepler-11b in Lopez *et al.* (2012). If a planet experiences enough mass loss to remove several percent of its mass, then it is much more likely to lose its envelope completely than to end up with an envelope that is ∼0.5% H/He.

Nonetheless, we do not see a gap that is as clear cut as that found by Owen and Wu (2013). Instead we see a diagonal band in which models are relatively rare, although by no means excluded. This "evaporation valley" is typically 0.5 $R_\oplus$ wide and occurs at slightly larger radii at higher incident fluxes. This is because in our parameter study we did not include planets that simply formed without any envelope at all. As a result, only planets that have lost their envelope to photo-evaporation end up being rocky. At the low flux end, only planets with initial envelopes ∼0.1% H/He and the lowest core masses will lose their envelopes, resulting in relatively small stripped cores. On the other hand, at the high flux end even planets with initial envelopes up to ∼ 1% H/He and core masses up to ∼10 $M_\oplus$ are easily stripped. This removes somewhat larger H/He envelopes but results in larger stripped cores, moving the evaporation

valley up to $\sim$2-2.5 $R_\oplus$.

However even in the middle of the diagonal evaporation valley, we find models from our study. Partially, this is due to varying the iron fraction of the cores, which smears out radius trends by $\sim$0.15 $R_\oplus$. Mostly however, it is due to running a comprehensive parameter study that sampled a wide range of initial conditions. The Owen and Wu (2013) study only tested five values for the core mass, without any initial compositions $<$1% H/He. In contrast, Figure 3.9 includes 200 different combinations of core mass and initial composition. In the absence of photo-evaporation, this suite of models finely samples the entire range of radii from 1-4 $R_\oplus$, as can be seen by the leftmost column in Figure 3.9. We suggest that the reason Owen and Wu (2013) see a clear gap in the radius-flux distribution is because their small sample of initial conditions do not adequately sample the parameter space.

Thus far no such gap has been has been seen in the observed distribution of planet radii. Fressin *et al.* (2013) and Petigura *et al.* (2013b) recently performed careful studies of *Kepler* planet occurrence rates as a function of radius after correcting for false positives and the various selection effects. In both cases the studies find a flat occurrence rate below $\sim$2.8 $R_\oplus$ with larger planets being significantly rarer. Both these studies span a wide range of periods, out to 85 days for Fressin *et al.* (2013) and 50 days for Petigura *et al.* (2013b), and use fairly wide radius bins. As a result, it is perhaps not surprising that they would not detect our relatively narrow evaporation valley. On the other hand, the flat occurrence rates found by Fressin *et al.* (2013) and Petigura *et al.* (2013b) seem inconsistent with the wide gap proposed by Owen and Wu (2013).

There are physical reasons why the evaporation valley seen in Figure 3.9 might not

exist or be less pronounced. First, there could exist a large population of 1-10 $M_\oplus$ rocky planets that simply formed without ever accreting a H/He envelope. This is possible if these planets formed through giant collisions after the disk had already dissipated (Morbidelli *et al.*, 2012). This would introduce another population of 1-1.8 $R_\oplus$ planets that would not show any strong dependence on incident flux due to photo-evaporation. Depending on how common these planets are, this could largely mask any gap in planet occurrence at radii $<$1.8 $R_\oplus$, which corresponds to incident flux $\lesssim$100 $F_\oplus$ or periods longer than $\sim$10 days.

Second, if sub-Neptunes typically form beyond the snowline then in addition to rock, iron, and H/He, these planets could have large amounts of water and other volatile ices (Rogers *et al.*, 2011). Much like varying the iron fraction of the core, varying the water fraction could wash out any trends in radius, but to a much greater extent. A 5 $M_\oplus$ planet that is 50% water will be $\sim$0.5 $R_\oplus$ larger than one with an Earth-like composition (Lopez *et al.*, 2012). Since our evaporation valley is only $\sim$0.5 $R_\oplus$ wide, varying the water content sub-Neptunes from 0-50% would completely eliminate any dip in planet occurance. *As a result, the presence or absence of such a dip is a useful test for whether sub-Neptunes form in situ without any water* (Chiang and Laughlin, 2013; Hansen and Murray, 2012), or migrate from beyond the snow-line with large amounts of water (Rogers *et al.*, 2011).

3.5.2 Relative Sizes in Multi-Planet Systems

Beyond simply explaining individual systems like Kepler-36, models of mass loss evolution may shed light on many of the puzzles of planet occurrence statistics. One such puzzle is that many of the *Kepler* multi-planet systems like Kepler-11, Kepler-18, & Kepler-36

exhibit regular ordering of their radii; i.e. each planet tends to be larger than the one interior to it. This trend was recently quantified by Ciardi *et al.* (2013) which found that in pairs of planets from *Kepler* multi-planet systems there is a statistically significant tendency for the inner planet to be smaller than the outer planet. Ciardi *et al.* (2013) examined over 900 pairs of planets with periods ranging from 0.45 to 331 days and found that the inner planet is smaller in $\approx$60% of planet pairs. Furthermore, they found that the fraction of planet pairs where the inner planet is smaller rises to $\sim$70% when the both planets are within 20 days, and that the trend is only apparent for planets that are smaller than Neptune. Assuming that these planets also have masses less than Neptune, these are precisely the planets that should be vulnerable to photo-evaporation. We find that this trend can be explained as a natural result of photo-evaporation. Unless there is a strong tendency for planets on shorter periods to have more massive rocky cores, then inner planets should be substantially more vulnerable to photo-evaporative mass loss.

On average we find that the inner planet in the Ciardi *et al.* (2013) sample receives 7.9 times more incident flux than the outer planet. Moreover, since this trend exists for pairs of planets orbiting the same parent star, we know that they receive the same XUV spectrum. Applying the scaling law derived in equation (3.7), this implies that the inner planets in their sample should typically lose $\sim$ 10 times as much H/He. In Lopez *et al.* (2012) we showed that there is a near one to one correspondence between radius and the H/He mass fraction. As a result, this increased vulnerability to mass loss should naturally lead interior planets to have smaller radii. In addition, we would expect the fraction of pairs with smaller inner planets to rise at the shortest periods if these trends are in fact due to atmospheric mass loss. When both

planets have periods shorter than $\sim$20 days, it is likely that both will be vulnerable to substantial mass loss and so there should be a larger impact on the relative radii.

However, there are several factors that can diminish the impact of mass loss on relative radii. Firstly, some planets will be rocky super-Earths without any volatile envelopes. Likewise our models predict that many planets on highly irradiated orbits should have envelopes completely stripped off. Of course, once a planet has lost its entire envelope its radius can not continue to shrink thus limiting any further differences in radii. Likewise, for planet pairs on less irradiated orbits, neither planet might be vulnerable to photo-evaporation. Also as we have already shown, large differences in rocky core mass can overwhelm differences in incident flux. All of the effects combine to limit the usefulness of radii alone to understand differences due to mass loss evolution and may explain why the trends seen by Ciardi *et al.* (2013) are relatively weak. Unfortunately, most of the planets in the Ciardi sample do not have mass measurements from radial velocity or TTVs, making it difficult to empirically test the importance of core mass on the trends they observe.

Currently, there are 16 pairs of *Kepler* planets where both planets have well determined masses and meet the SNR and impact parameter thresholds described in Ciardi *et al.* (2013). These include planets in Kepler-9 (Holman *et al.*, 2010), Kepler-10 (Batalha *et al.*, 2011), Kepler-11 (Lissauer *et al.*, 2011a, 2013), Kepler-18 (Cochran *et al.*, 2011), Kepler-20 (Fressin *et al.*, 2012; Gautier *et al.*, 2012), and Kepler-36 (Carter *et al.*, 2012). Of these 16 pairs, in four cases the inner planet is larger than the outer: Kepler-9b/c, Kepler-11c/f, Kepler-11d/f, Kepler-11e/f. In all four of these cases the inner is significantly more massive than the outer planet. With only four cases the trend is not yet statistically significant, however, the ten-

dency for inner planets to be either smaller or significantly more massive is a robust prediction of our mass loss models. Whenever the inner planet in a multi-planet system has a larger radius, it should also be significantly more massive. There should not be any highly irradiated pairs of planets where the inner planet is less massive than the outer but where the inner planet has enough of its mass in a H/He envelope such that its radius larger.

It is worth mentioning that there are other processes in planet formation and evolution which could contribute to the trends seen by Ciardi *et al.* (2013). Ikoma and Hori (2012) showed that when super-Earths and sub-Neptunes form on highly irradiated orbits, the rate of H/He accretion is significantly slower when the local disk temperature is higher. Moreover, on short period orbits it is much easier for low mass planets to open a gap in the disk, which would also limit their envelope accretion (Hansen and Murray, 2012). Assuming that planets in the *Kepler* multis formed in the same ordering that they are in today, then inner planets should have had more difficulty in accreting large H/He envelopes. Likewise, given that proto-planetary disks evaporate from the inside out (Calvet *et al.*, 2000), outer planets will have had more time to accrete an envelope. Nonetheless, given the critical mass loss timescale threshold that we identified observationally and theoretically in Lopez *et al.* (2012), and a concurring view advanced by Wu and Lithwick (2013), it seems quite reasonable that photo-evaporative mass loss plays an important role in producing the trends among planet pairs seen by Ciardi *et al.* (2013). Most likely, both planet formation and subsequent evolution combine to reduce the size of H/He envelopes for highly irradiated planets.

3.6 Chapter Summary

There is growing evidence from both models and observations that photo-evaporative mass loss plays an important role in the evolution of highly irradiated super-Earths and sub-Neptunes (Baraffe *et al.*, 2006; Jackson *et al.*, 2012; Wu and Lithwick, 2013). Lecavelier Des Etangs (2007) first proposed that there could be a critical mass loss timescale in the observed population of hot Jupiters and Neptunes. In Lopez *et al.* (2012) we confirmed the existence of this threshold for all planets with measured densities down to 2 $M_{\oplus}$. Moreover, Lopez *et al.* (2012) showed that this critical mass loss timescale is naturally reproduced by our coupled thermal and mass loss evolution models. Likewise, this mass loss threshold is also reproduced by other models which fully solve the hydrodynamics of the mass loss wind (Owen and Jackson, 2012; Owen and Wu, 2013). Here we have expanded upon the parameter study performed in Lopez *et al.* (2012) and shown in detail how mass loss history depends on incident flux, core mass, and mass loss efficiency.

We have shown that in addition to the amount of XUV irradiation received by a planet, the mass of its rock/iron core plays a critical role in determining a planet's photo-evaporation history. Moreover we have shown that this provides a natural explanation for the large density contrast observed between Kepler-36 b&c. In order to better understand the role of core mass, we performed an extensive parameter study and provided approximate scaling relations which can be used for estimates of whether mass loss has been important for detected planets.

Further, we showed that the compositions of the observed population of transiting planets are consistent with our detailed models and these scaling relations. Finally, we showed

that our coupled thermal and mass-loss evolution models make important predictions for the radius-flux distribution of *Kepler* candidates. In particular, we predict that sub-Neptune sized planets should become significantly less common at very short orbital periods. In addition, there may exist a narrow "evaporation valley," which is a useful test for whether sub-Neptunes are formed in situ. We anticipate that future progress in this area will come from additional mass determinations of sub-Neptune size *Kepler* candidates, a better understanding of XUV fluxes from all types of stars as a function of age, and further progress in modeling mass loss efficiencies in the framework of 1D and 3D models.

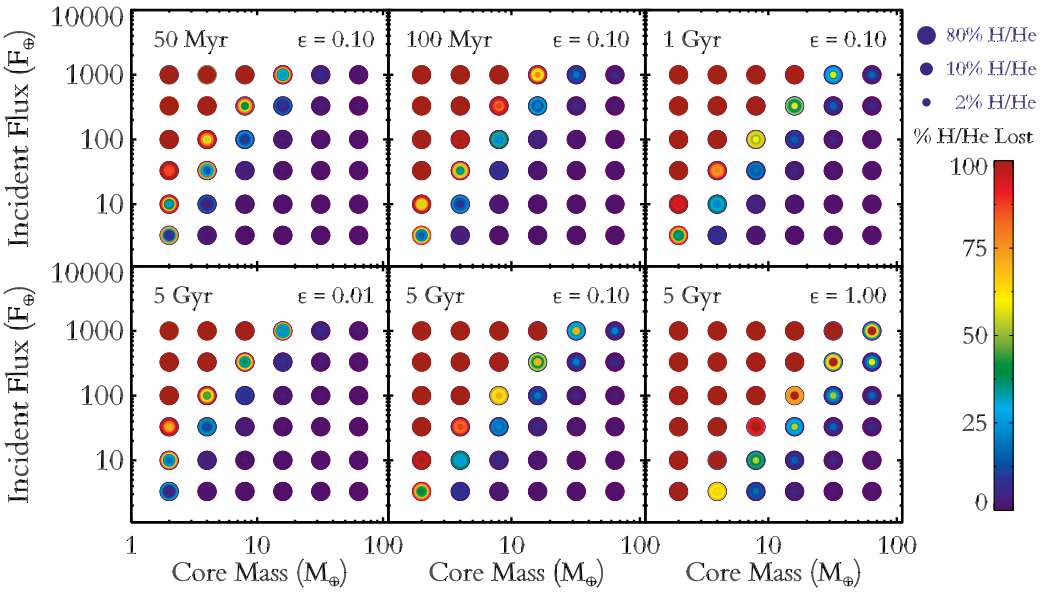

Figure 3.2 This summarizes the results of our evolution paramter study. In each panel we have plotted models on a grid of incident flux vs. planetary core mass in Earth masses. At each point in the grid, we have over-plotted multiple models with different initial compositions. The size of each point indicates the initial H/He fraction a planet began with. Meanwhile, colors indicate how much of this initial H/He envelope is lost over time. Thus dark blue points are models where mass loss is unimportant while dark red points are models where the entire H/He envelope has been stripped off. The mass loss history depends strongly on a planet's core mass as well as the incident flux. In each case, there is a clear threshold region where mass loss is important but, at least some models are able retain significant H/He envelopes. The top panels show the threshold at 50 Myr, 100 Myr, and 1 Gyr for our standard mass-loss efficiency of 10%. Most of the mass is lost in the first 100 Myr while almost no mass is lost after 1 Gyr. Likewise, the bottom panels show the results at 5 Gyr for efficiencies of 1, 10, and 100%.

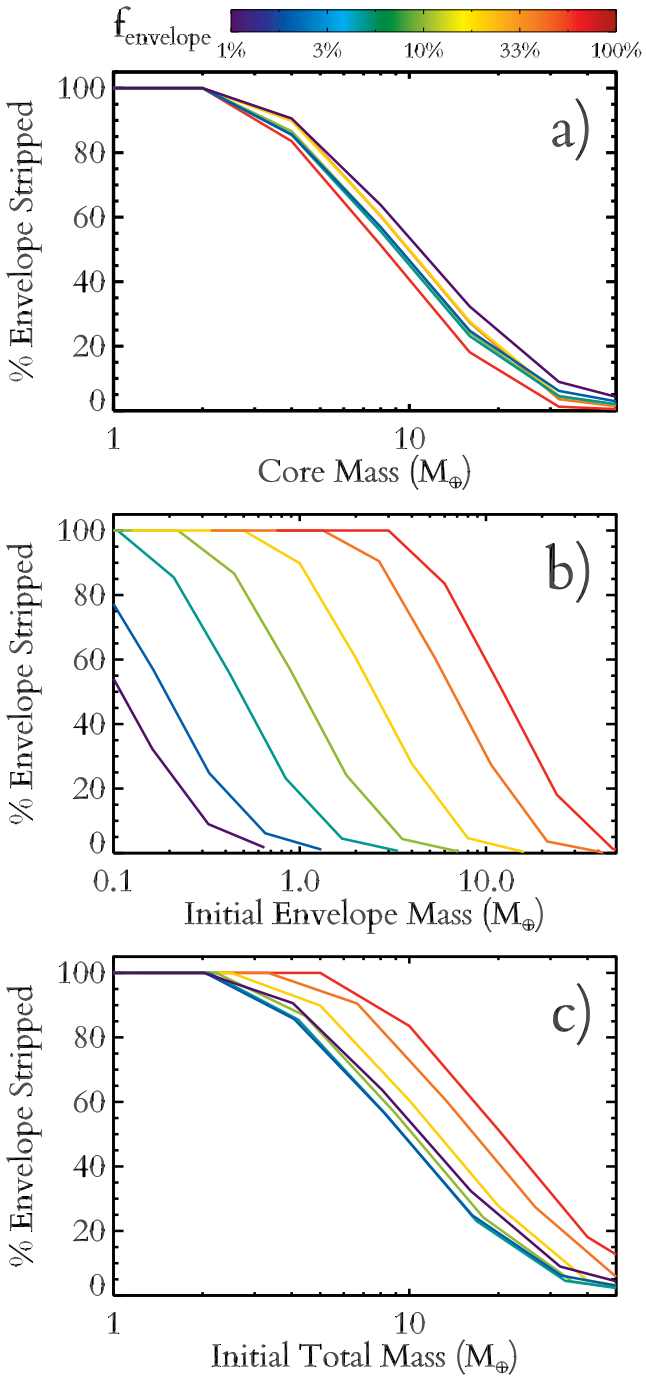

Figure 3.3 The fraction of the initial H/He envelope which is lost to subsequent photo-evaporation (f_{lost}) vs. three different mass parameters, according to our models. Panel a) plots f_{lost} against the mass of the rock/iron core while panel b) plots it against the mass of the initial H/He envelope and panel c) plots against the total initial mass. In each case, the different curves show the results for models with different initial H/He fractions $f_{envelope}$, varying from 1-60% H/He. All of these models receive 100 $F_{\oplus}$, assume ϵ = 0.1, start at 10 Myr, and end at 5 Gyr. Compared to envelope or total mass, core mass shows the least scatter between models with different composition.

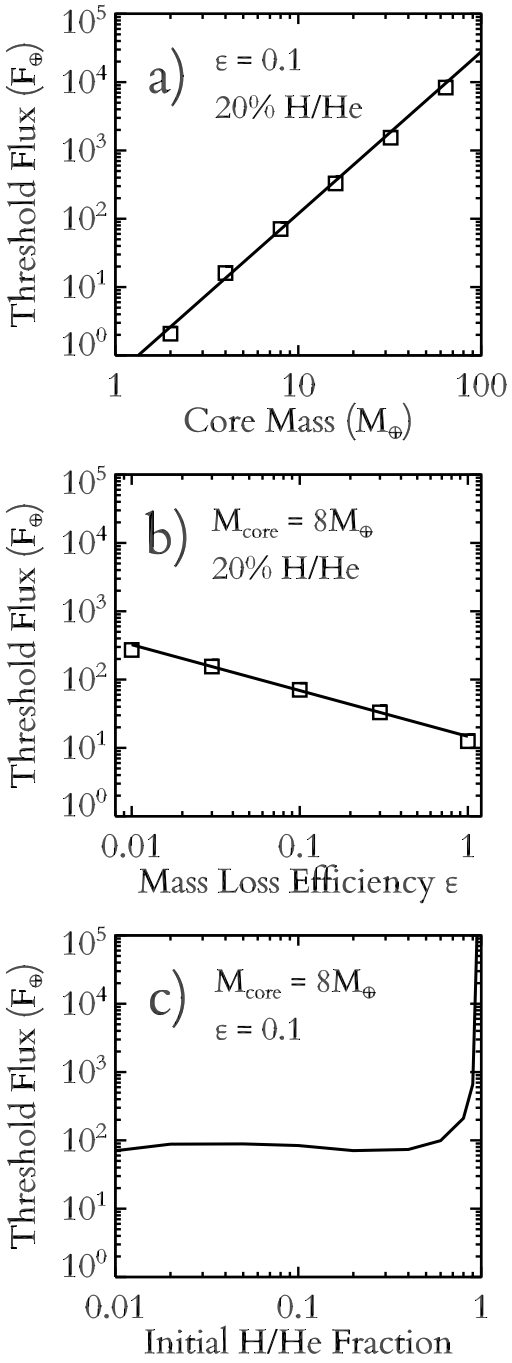

Figure 3.4 Three panels showing how the threshold flux varies with core mass, mass loss efficiency and the initial composition. In panel a) we show how the threshold flux, the incident flux needed to remove half a planet's initial H/He envelope, varies with the core mass along with the best fit power-law. In panel b) we do the same for the mass loss efficiency. In panel c) we show how the threshold flux depends on the initial H/He envelope fraction. There is little dependence on composition until the planet starts out > 60% H/He.

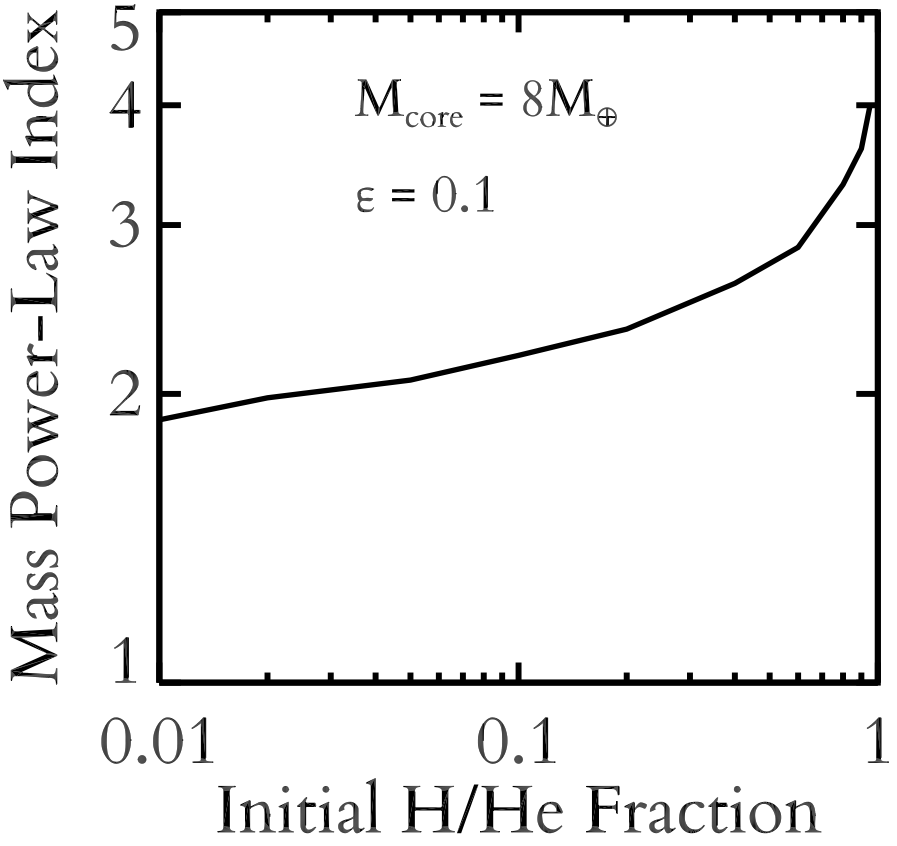

Figure 3.5 Index of the core mass power-law from Figure 3.4 and equation (3.6) vs. initial H/He envelope fraction. The dependence on core mass becomes steeper as the initial H/He fraction increases.

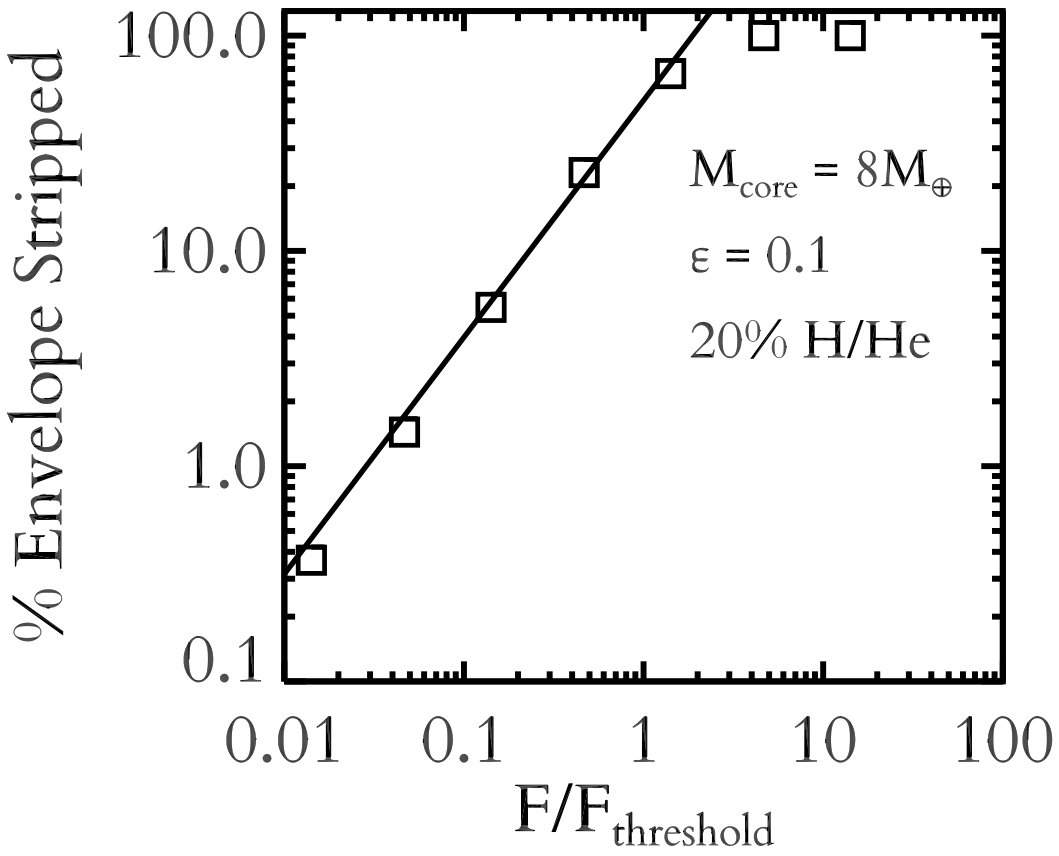

Figure 3.6 $f_{\rm lost}$ the fraction of the initial H/He that is stripped after 5 Gyr vs. incident flux compared to $F_{\rm th}$ the threshold flux defined in equation (3.6). Below $F_{\rm th}$, $f_{\rm lost}$ increases roughly linearly with incident flux. Above $\sim 2\times F_{\rm th}$, the envelop is completely stripped.

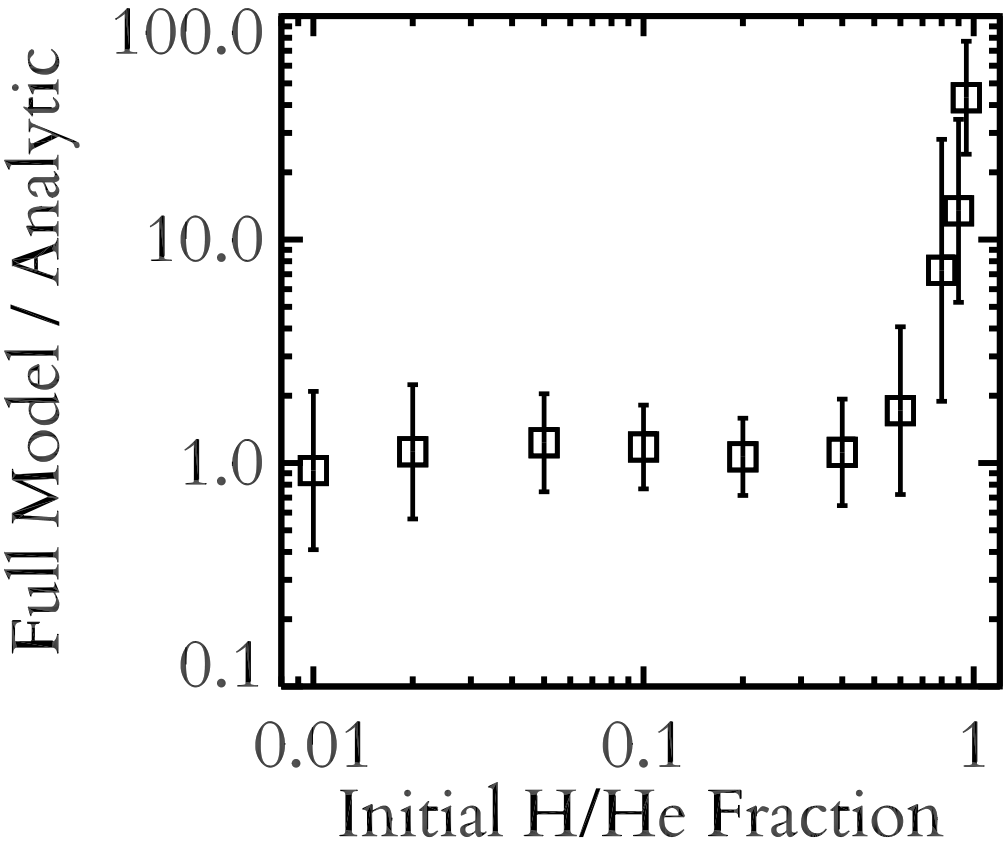

Figure 3.7 f_{lost} according to the results of our full model from Figure 3.2 is divided by f_{lost} according to the simple analytic description in equation (3.6) and plotted against initial H/He fraction. For initial compositions < 50% H/He, the two generally agree within a factor of 2 or better.

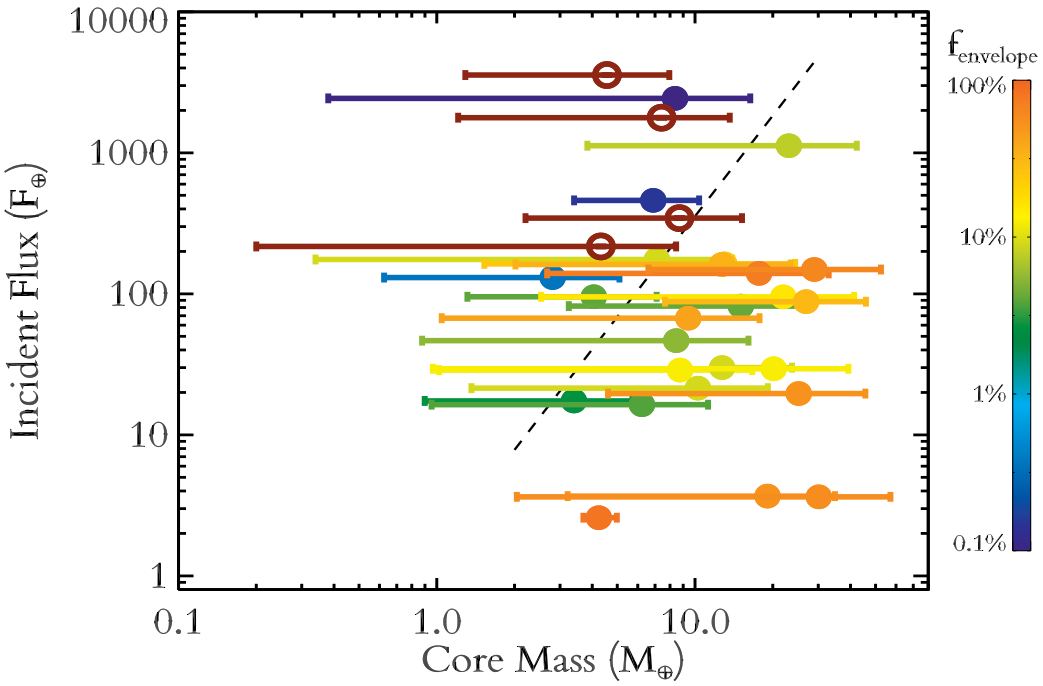

Figure 3.8 Incident flux and core mass for 29 observed transiting planets with well defined masses less than 100 $M_{\oplus}$. Planets are color-coded by their current H/He envelope fraction. Red-brown open circles are consistent with being H/He free. The dashed line shows the $F_{\rm th} - M_{\oplus}$ relation from equations (3.6) and (3.7), scaled up slightly to account for complete stripping of H/He. Of the six planets that lie 1 σ to the left of this relation, three are consistent with being rocky and three with having only water/steam envelopes.

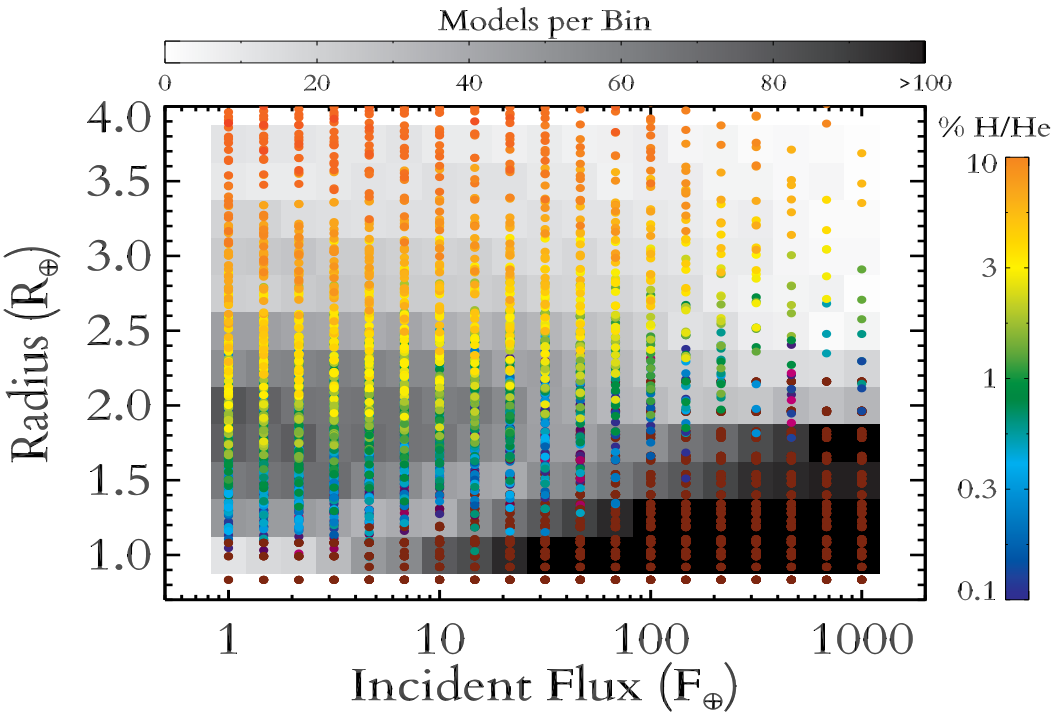

Figure 3.9 Final planet radius vs. incident flux in our parameter study. The greyscale boxes indicate the frequency of models that end in each box due to thermal and mass loss evolution; i.e., black boxes contain many models and white boxes few. At high incident flux there is a strong decrease in the frequency of $\sim 1.8-4.0\ R_\oplus$ sub-Neptune sized planets and an increase in the frequency of $\lesssim 1.8\ R_\oplus$ rocky super-Earths. Points show the individual models, colored by their final H/He envelope fractions as result of photo-evaporation. The leftmost column of points at $1\ F_\oplus$ closely approximates the distribution without any mass loss. Rust colored points in the bottom right correspond to rocky planets that have lost their envelopes. Just above these stripped cores there is a clear decrease in the frequency of models. Planets that enter this region have envelopes that are so small they tend to be stripped off completely.

Chapter 4

Understanding the Mass-Radius Relation for Sub-Neptunes: Radius as a Proxy for Composition

4.1 Introduction

NASA's *Kepler* mission has been an enormous success, discovering over 3500 planet candidates to date (Borucki *et al.*, 2011; Batalha *et al.*, 2013a). Among the mission's many firsts and accomplishments, however, one of the most revolutionary is that for the first time we have a robust determination of the relative abundance of different sizes of planets stretching from Earth-sized all the way up to the largest hot Jupiters (Howard *et al.*, 2012; Fressin *et al.*, 2013; Petigura *et al.*, 2013b).

In particular, *Kepler* has discovered an abundant new population of $\sim$3 $R_\oplus$ planets (Fressin *et al.*, 2013; Petigura *et al.*, 2013b). Although smaller than Neptune, these planets are

large enough that they must have substantial hydrogen and helium (hereafter H/He) envelopes to explain their radii. Such planets are unlike anything found in our own Solar System and fundamental questions about their structure and formation are still not understood. Are these Neptune-like planets that form beyond the snow-line and contain large amounts of volatile ices (Rogers *et al.*, 2011), or are these scaled up terrestrial worlds with H/He envelopes that formed close to their current orbits (Hansen and Murray, 2013; Chiang and Laughlin, 2013)?

In an attempt to address these questions, a great deal of effort has been invested in acquiring precise masses for a large number of these transiting planets. In recent years this has generated a much fuller understanding of the mass-radius relation, especially for sub-Neptune and super-Earth sized planets (Weiss *et al.*, 2013). In particular, there are now several multi-planet *Kepler* systems like Kepler-11 with masses determined from Transit Timing Variations (TTVs) (e.g Lissauer *et al.*, 2011a; Carter *et al.*, 2012; Cochran *et al.*, 2011; Lissauer *et al.*, 2013). Although rare, such systems are incredibly valuable because with both a mass and a radius we can estimate a planet's bulk composition using models of interior structure and thermal evolution (e.g. Rogers and Seager, 2010a; Nettelmann *et al.*, 2011; Miller and Fortney, 2011; Lopez *et al.*, 2012; Valencia *et al.*, 2013). Thus far efforts have been focused on individually determining compositions for this handful of planets. This paucity stands in stark contrast to the over 3500 *Kepler* Candidates with only measured radii. Unfortunately the vast majority of these candidates are in dynamically inactive systems without strong TTVs or around distant stars too faint for radial velocity measurements.

Moreover, even with precise masses and radii there are inherent degeneracies which limit one's ability to constrain the bulk compositions of super-Earth sized planets. For 1-

2 $R_\oplus$ planets the densities of water, silicate rocks, and iron (i.e. $\sim$ 1-10 g cm^{-3}) are similar enough that it is impossible to uniquely constrain the relative abundance of these components (Valencia *et al.*, 2007; Rogers and Seager, 2010a). To some extent models of planet collisions can set upper limits on the maximum iron or water mass fractions that are physically achievable (Marcus *et al.*, 2009, 2010), but for a given planet this still allows a wide range of internal compositions.

Fortunately, models are still able to set clear and useful constraints on composition. In particular, thermal evolution models can set robust constraints on the fraction of a planet's mass in a H/He envelope. Due to its significantly lower density, even a relatively minor amount of H/He (e.g., $\sim$1% of total planet mass) has a large impact on planetary radius. For sub-Neptune sized $\sim$ 3 $R_\oplus$ or larger planets, the H/He envelope will dominate a planet's size regardless of the abundance of other elements. As a result, for these planets, any degeneracies between rock, water, and iron are secondary to the overall distribution of material between the H/He envelope and heavier elements.

Moreover, for sub-Neptune sized planets at fixed bulk-composition, theoretical mass-radius curves are remarkably flat; i.e., planets with a given H/He abundance have very similar sizes regardless of their mass (Lopez *et al.*, 2012). As a result, there is a remarkably tight relationship between planetary radius and H/He envelope fraction that is independent of planet mass. Critically, this opens up the hope of constraining H/He envelope fractions for the vast population of Neptune and sub-Neptune sized *Kepler* candidates without measured masses. This is what we begin to explore in this paper.

Whenever possible it is still preferable to obtain a well measured mass. Planet mass

is critical for understanding how volatile rich planets accrete their initial H/He envelope (Bodenheimer *et al.*, 2000; Ikoma and Hori, 2012) and whether they can retain it against X-ray and EUV driven photo-evaporation (Lopez *et al.*, 2012; Lopez and Fortney, 2013a; Owen and Jackson, 2012; Owen and Wu, 2013). Nevertheless, for systems of sub-Neptunes like Kepler-11, even a factor of $\sim$2 uncertainties in planet masses are sufficient to tightly constrain H/He envelope fractions with precise radii (Lissauer *et al.*, 2013). This fact means that instead of only examining the *radius* distribution of *Kepler* candidates, we can begin thinking about a *composition* distribution.

4.2 Models

In order to understand how planetary radius relates to planet mass and envelope fraction, it is necessary to fully model how a planet cools and contracts due to thermal evolution. For this work, we have used the thermal evolution presented in Chapter 2, where additional model details can be found. Similar models are frequently used to track the evolution of sub-Neptunes and hot Jupiters. (e.g, Miller and Fortney, 2011; Nettelmann *et al.*, 2011). Unlike Chapters 2 and 3, here we do not consider the effects of photo-evaporation. Although photo-evaporation can have a large impact on the H/He envelope fraction of a planet (e.g. Baraffe *et al.*, 2006; Hubbard *et al.*, 2007a; Lopez *et al.*, 2012; Owen and Jackson, 2012), the effect on the thermal state of the interior is relatively minor (Chapter 3). Here we are primarily interested in the relationship between radius and H/He envelope fraction as controlled by thermal evolution, as a result the effects of photo-evaporation can be ignored. In essence, present-day envelope fraction

determines the radius, but that envelope fraction may have been strongly effected by formation and photo-evaporation.

At a given age, a model is defined by the mass of its heavy element core, the mass of its H/He envelope, the amount of incident radiation it receives, and the internal specific entropy of its H/He envelope. As a default model, we assume an isothermal rock/iron core with an Earth-like 2:1 rock/iron ratio, using the ANEOS olivine (Thompson, 1990) and SESAME 2140 Fe (Lyon and Johnson, 1992) equations of state (EOS). When determining envelope fraction error bars for observed planets, however, we varied this iron fraction from pure rock to the maximum possible iron fraction from impact models in Marcus *et al.* (2010). For the H/He envelope we assume a fully adiabatic interior using the Saumon *et al.* (1995) EOS. In addition we consider the possibility of water-worlds and three component models using the H2O-REOS for water (Nettelmann *et al.*, 2008). Finally atop the H/He envelope is a relatively small radiative atmosphere, which we assume is isothermal at the equilibrium temperature. We define a planet's radius at 20 mbar, appropriate for the slant viewing geometry in optical transits for solar metallicity, although our results are insensitive to the exact pressure level chosen (Hubbard *et al.*, 2001) .

In order to quantitatively evaluate the cooling and contraction of the H/He envelope, we use a model atmosphere grid over a range of surface gravities and incident fluxes. These grids relate the surface gravity and internal specific entropy to the intrinsic temperature of the flux emitted for a given model. The intrinsic temperature $T_{\rm int} = (T_{\rm eff}^4 - T_{\rm eq}^4)^{1/4}$ is the equivalent blackbody temperature of the net radiation leaving a planet, it is approximately the temperature the planet would have if the parent star were removed. These one-dimensional radiative-

convective models are computed for solar metallicity and for 50× solar metallicity enhanced opacity atmospheres using the methods described in Fortney *et al.* (2007) and Nettelmann *et al.* (2011). These atmosphere models are fully non-gray, i.e. wavelength dependent radiative transfer is performed rather than simply assuming a single infrared opacity. The atmospheres of Neptune and sub-Neptune sized planets might be significantly enhanced in metals (Fortney *et al.*, 2013) or host extended clouds that greatly enhance atmospheric opacity (Morley *et al.*, 2013). Therefore, our two atmosphere grids are a way to make a simplified first estimate of the role of enhanced opacity on planetary thermal evolution. For all runs we use the H/He Saumon *et al.* (1995) EOS for the envelope.

At very early times and very low masses, the models reach gravities beyond the edge of our cooling grid. In such cases we logarithmically extrapolate the intrinsic temperature $T_{\rm int}$ as a function of gravity. This does not significantly affect our results, however, as the dependence of $T_{\rm int}$ on gravity is slight and the models are only at such low gravities in the first few Myr.

Finally, we include heating from radioactive decay in the rock/iron core and the delay in cooling due to the core's heat capacity. In order to correctly determine the mass-radius-envelope fraction relationship, it is vital to include these thermal evolution effects, since these will significantly delay cooling and contraction, particularly for planets less than $\sim 5\,M_{\oplus}$ (Lopez *et al.*, 2012).

$$\int_{M_{\rm core}}^{M_{\rm p}} dm \frac{T\,dS}{dt} = -L_{\rm int} + L_{\rm radio} - c_{\rm v} M_{\rm core} \frac{dT_{\rm core}}{dt} \tag{4.1}$$

Equation (4.1) (Nettelmann *et al.*, 2011; Lopez *et al.*, 2012) summarizes our ther-

mal evolution models. The left hand side describes the cooling rate of the H/He envelope. Positive terms on the right hand side represent energy sources that heat and inflate a planet, while negative terms represent energy losses that allow a planet to cool and contract. The term $L_{\rm int} = 4\pi R_{\rm p}^2 \sigma T_{\rm int}^4$ accounts for cooling from the atmospheric radiative transfer models described above. $L_{\rm radio}$ describes radioactive heating, with abundances given by Anders and Grevesse (1989). Finally, $dT_{\rm core}/dt$ represents the cooling of the rocky core. We assume a core heat capacity of $c_v = 0.5 - 1.0$ JK^{-1} g^{-1} (Alfè *et al.*, 2002; Guillot *et al.*, 1995; Valencia *et al.*, 2010). Each of these terms is described in detail in Nettelmann *et al.* (2011) and Lopez *et al.* (2012).

As with previous models, we assume that planets initially form with a large initial entropy according to the traditional "Hot-Start" model (Fortney *et al.*, 2007; Marley *et al.*, 2007). Specifically we start our models at an age of 1 Myr with a large initial entropy of 10 $k_{\rm b}$ baryon^{-1}. This assumption does not significantly affect any of our results since hot-start and cold-start models are indistinguishable by the time planets are $\sim$100 Myr old (Marley *et al.*, 2007; Lopez *et al.*, 2012). Moreover, Mordasini (2013) recently showed that for planets less massive than Jupiter gravitational heating due to settling of heavy elements in the H/He envelope can erase any difference between hot and cold starts.

For low-mass planets, the hot-start assumption results in extremely large initial radii $\gtrsim$10 $R_\oplus$. However, as we explore in Section 3.2, such models cool extremely rapidly such that significant contraction has already occurred by several Myr. In general we present results at ages $>$10 Myr, when our results are insensitive to the initial choice of entropy.

4.3 A Mass Radius Parameter Study

Planetary radius is an invaluable tool in understanding the nature of low-mass planets; however, without the aid of thermal evolution models like those used here, it can be quite difficult to interpret. In order to better understand the information contained in planet radii, we performed a detailed parameter study of our thermal evolution and structure models for sub-Neptune type planets with rock/iron cores and thick H/He envelopes.

As part of this parameter study we ran over 1300 thermal evolution models varying planet mass, incident flux, envelope fraction, and atmospheric metallicity. We covered planets from 1-20 $M_{\oplus}$, 0.1-1000 $F_{\oplus}$, 0.01-60% H/He, for both solar metallicity and enhanced opacity models.We then recorded planet radius at every age from 10 Myr to 10 Gyr. The results of this study are summarized in Figure 4.1 and Tables A.3-A.8.

Examining Figure 4.1, it is immediately clear that iso-composition mass-radius curves are in fact remarkably flat for sub-Neptune or larger planets, at least once they are a few Gyr old. In each panel, we show theoretical mass-radius curves while varying the H/He envelope fraction, incident flux, and age of the model planets. For the parameters that are not varying in each panel, we use representative values of 5% H/He, 100 $F_{\oplus}$, and 5 Gyr.

Turning to panel a), we see the enormous effect that varying the H/He envelope fraction has on planetary radius. By comparison, any other changes to incident flux, age, or internal structure are secondary. For planets with envelopes $\sim$0.1% of their total mass, the mass-radius curve does increase slightly from $\sim$1.5 $R_{\oplus}$ at 1 $M_{\oplus}$ to $\sim$2.5 $R_{\oplus}$ at 20 $M_{\oplus}$. For envelopes this insubstantial, a planet's size is still dominated by its rocky/iron core and so the mass-radius

Figure 4.1 Here we show model mass-radius relations from 1-20 $M_{\oplus}$ and how these depend on H/He envelope fraction, irradiation, and age, indicated by the colors. Solid lines correspond to enhanced opacity models, while dotted lines correspond to solar metallicity. The dashed rust-colored lines show the size of bare rocky planets with Earth-like rock/iron abundances. Our default model is 5% H/He, 5 Gyr old, and receives $\sim$100 $F_{\oplus}$. In panel a) we vary the H/He envelope fraction from 0.1-60% H/He, this has by far the largest impact on planet size. In panel b) we vary the incident flux a planet receives from 1-1000 $F_{\oplus}$. In panel c) we show a time evolution from 10 Myr to 10 Gyr.

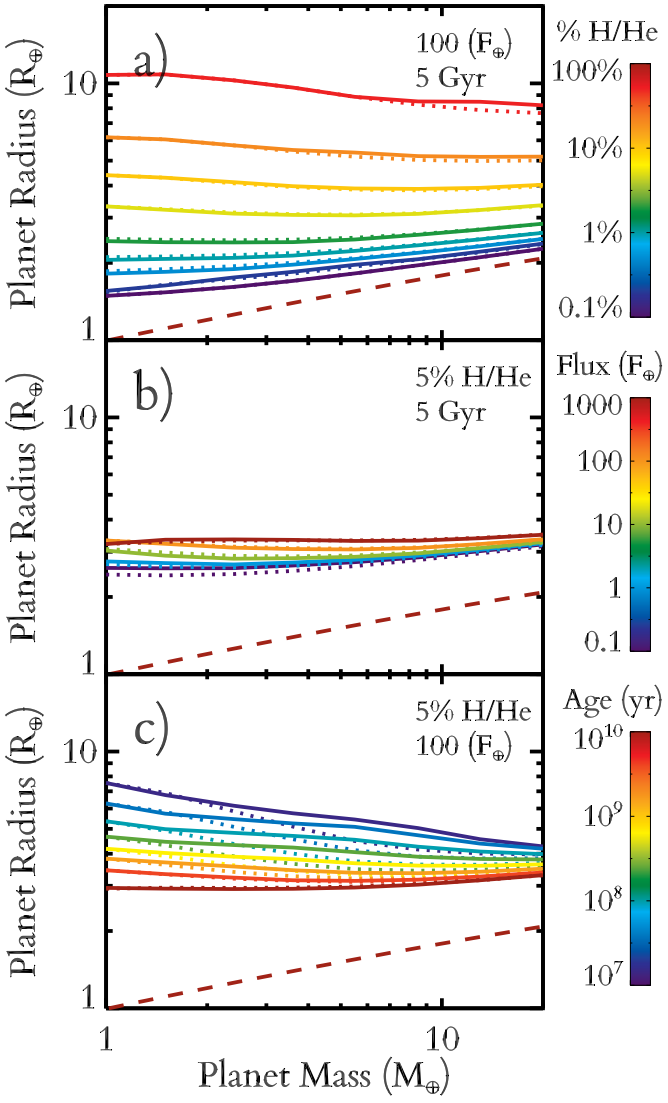

curves have a similar slope to the bare rock curve shown in Figure 4.1. However, as we increase the envelope fraction, the mass-radius curves rapidly flatten, beginning at low-masses, until by $\sim$3% H/He, the curves are almost completely flat.

By comparison, panel b) in Figure 4.1 shows the much more modest effect of varying the incident flux. More irradiated planets tend to be slightly larger because they have a large scale height in their atmospheres and because the irradiation alters the radiative transfer through their atmosphere, slowing their contraction (Fortney *et al.*, 2007). Nonetheless, despite varying the incident flux by four orders of magnitude, planet radii vary by less $\sim$30%.

Finally, panel c) shows how these mass-radius curves evolve over time. At early times lower mass planets are significantly larger than higher mass planets due to their similarly large internal energies and lower gravities. Over time, however, these low mass planets are able to cool more rapidly than their more massive relatives, which gradually flattens the mass-radius curves. By the time the planets are $\sim$ 1 Gyr old we see the characteristically flat mass-radius curves for H/He rich planets.

4.3.1 Describing Radius with Power-Laws

A quick inspection of Figure 4.1 makes clear that not all of a planet's properties have an equal impact on planet size. Planet mass and incident flux have only a modest impact on planet size, while planet age has a larger impact, particularly at younger ages. However, by far the largest determinate of a planet's size is the fraction of its mass in a H/He envelope. One way to quantify the relative importance of envelope fraction is to construct analytic fits for radius as a function of planet mass $M_{\rm p}$, H/He envelope fraction $f_{\rm env}$, incident flux $F_{\oplus}$, and age. In

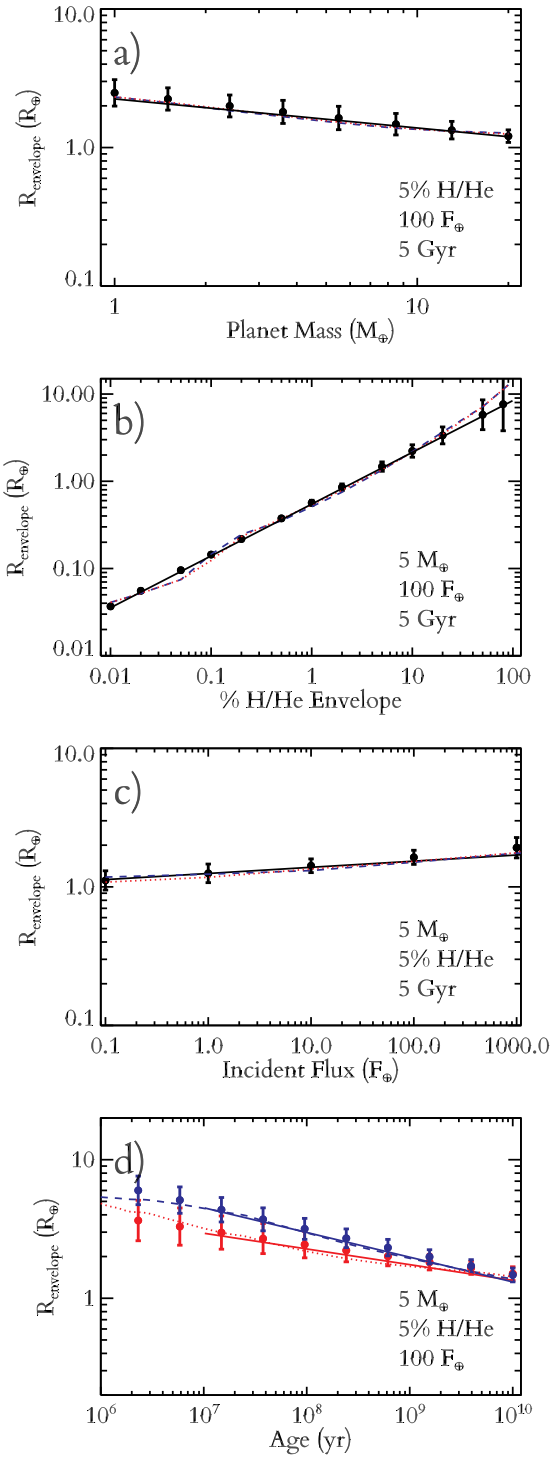

Figure 4.2 Four panels showing how the radius of the H/He envelope $R_{\rm env} = R_{\rm p} - R_{\rm core} - R_{\rm atm}$ varies with planet mass, envelope mass fraction, incident flux, and planet age for representative values. Red dotted lines correspond to solar metallicity atmospheres, while blue dashed lines correspond to enhanced opacity. Solid lines indicate power-law fits as described in equation (4.4). Here we use default values of 5 $M_\oplus$, 100 $F_\oplus$, 5% H/He, and 5 Gyr.

Lopez and Fortney (2013a) we performed a similar analysis examining planets' vulnerability to photo-evaporative mass loss.

Fortunately, the relationships between radius and each of these parameters are all reasonably well described by power-laws and the effects of each variable are relatively independent. As a result, we can do a reasonably good job of describing the results of our full parameter study with a set of four independent power-laws. The one caveat is that we do not fit for the total planet radius $R_{\rm p}$, but instead the radius of the H/He envelope $R_{\rm env} \approx R_{\rm p} - R_{\rm core}$, where $R_{\rm core}$ is the size of the rock/iron core. We do this because as $f_{\rm env}$ approaches zero, the planet radius does not approach zero but instead asymptotes to $R_{\rm core}$.

To first order, however, the rock/iron equation of state is very incompressible and so we can approximate $R_{\rm core}$ with the mass-radius curve of a envelope free rocky planet. Assuming an Earth-like rock/iron abundance, then $R_{\rm core}$ is described by equation (4.2) to within $\sim$2%. If we also allow the iron-fraction of the core to vary then this error rises to $\sim$10%, but for the qualitative analysis we attempting here such errors are unimportant. $M_{\rm core}$ in equation (4.2) refers to the mass of the rock/iron core, which for sub-Neptune sized planets is approximately the same as the total planet mass $M_{\rm p}$.

$$R_{\rm core} = \left(\frac{M_{\rm core}}{M_\oplus}\right)^{0.25} \approx \left(\frac{M_{\rm p}}{M_\oplus}\right)^{0.25} \tag{4.2}$$

Likewise, we must make a small correction to account for the size of the radiative upper atmosphere. To first approximation, this atmosphere is isothermal at the planet's equilibrium temperature $T_{\rm eq}$. For sub-Neptune sized planets at several Gyr, the radiative-convective

boundary is typically ∼100-1000 bar. For transiting planets the broadband optical radius is typically ∼20 mbar, or ≈8-10 scale heights higher. Thus the size of the radiative atmosphere is approximately given by equation (4.3), where g is a planet's gravity and $\mu_{\rm H/He}$ is the mean molecular weight. Generally however, this correction is typically quite small (∼0.1 $R_\oplus$) except at the very highest levels of irradiation.

$$R_{\rm atm} \approx \log\left(\frac{100\,{\rm bar}}{20\,{\rm mbar}}\right) H \approx 9\left(\frac{k_{\rm b}\,T_{\rm eq}}{g\,\mu_{\rm H/He}}\right) \tag{4.3}$$

With equations (4.2) and (4.3) in place, we can now fit for $R_{\rm env}$, and then simply add $R_{\rm core}$ and $R_{\rm atm}$to get the total radius. The results of these fits are summarized in Figure 4.2 and equation (4.4). Figure 4.2 compares our power-law fits to the results of our full models for representative values of $M_{\rm p}$, $f_{\rm env}$, $F_\oplus$, and age. The error bars in each panel show the 1σ scatter about the power-law fits for the full suite of models in our parameter study. Remarkably, this simple power-law description does a reasonable job of reproducing the results of our full model. In general, the analytic formulation in equation (4.4) matches our full models to within ∼0.1 dex.

For the age evolution, we fit separate power-laws for solar metallicity and enhanced opacity models. The solar metallicity models cool more rapidly initially. As a result, they are already relatively cold by ∼100 Myr and so the subsequent contraction is slower. However, the enhanced opacity models must eventually cool and by several Gyr any differences are erased. We fit power-laws only to the evolution after 100 Myr. For solar metallicity $R_{\rm env} \sim t^{0.11}$ while for enhanced opacity $R_{\rm env} \sim t^{0.18}$. Equation (4.4) shows the results for the enhanced opacity

models.

$$R_{\rm env} = R_{\rm p} - R_{\rm core} - R_{\rm atm} = 2.06\,R_\oplus \left(\frac{M_{\rm p}}{M_\oplus}\right)^{-0.21} \times \left(\frac{f_{\rm env}}{5\%}\right)^{0.59} \left(\frac{F_{\rm p}}{F_\oplus}\right)^{0.044} \left(\frac{age}{5\,{\rm Gyr}}\right)^{-0.18} \tag{4.4}$$

It is important to note however, that the results of these fits are only meant to be a rough approximation of the full models summarized Figure 4.1 and tables 2-6. These fits are done purely to help understand the qualitative behavior of our thermal evolution models, not to be used in place of the full models. Also, equation (4.4) only shows the fit to our the enhanced opacity models. At late times the solar metallicity models have a slightly shallower dependence on age, due to more rapid cooling at early ages.

Nonetheless, equations (4.2) and (4.4) do make several things quite clear. First of all, we can now quantify the importance of H/He envelope fraction; doubling $f_{\rm env}$ has an order of magnitude larger effect on $R_{\rm p}$ than doubling $F_{\rm p}$ and more than twice as large as an effect of doubling the age. We can also now see how flat the mass-radius curves are. Although, $R_{\rm env}$ decreases slightly with mass, this is almost exactly balanced by the increase in $R_{\rm core}$ with increasing mass. This result is insensitive to our choice of initial entropy for ages $\gtrsim$10 Myr.

4.3.2 Why is the Mass-Radius Relation Flat?

One of the key features of our thermal evolution and structure models is the relative flatness of mass-radius curves at fixed H/He envelope fraction. In sections 4.3 and 4.3.1, we showed that for planet with $\gtrsim$1% H/He, planet size is more or less indepent of mass. Thus far, however, we have not explained the origin of this flatness.

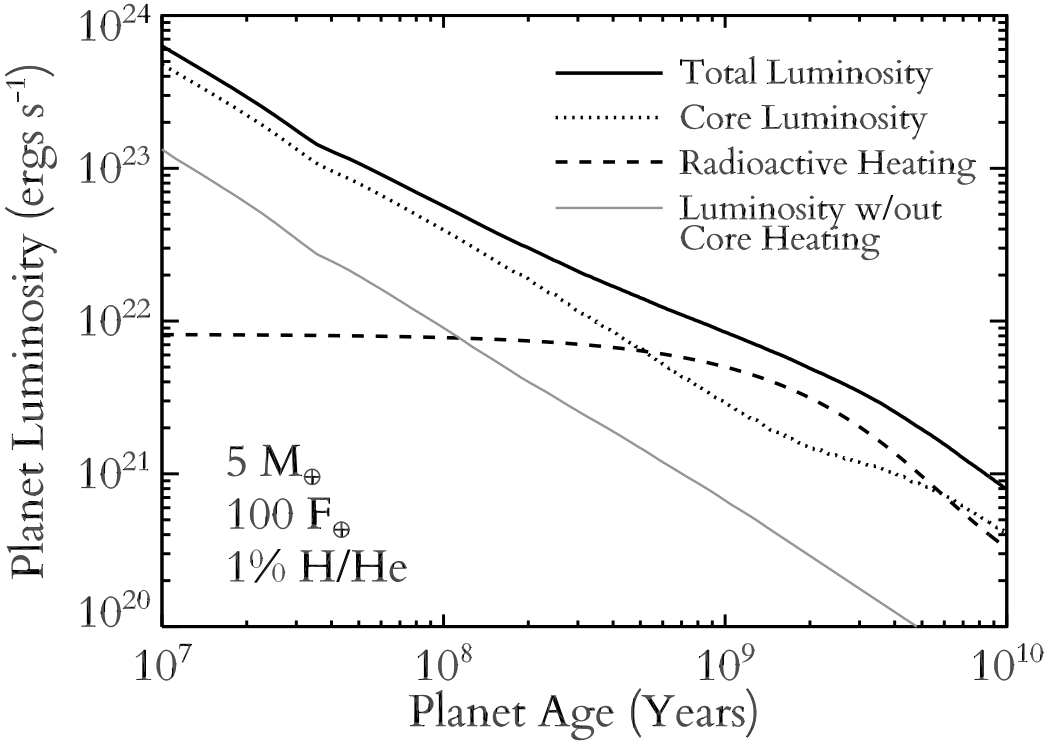

Figure 4.3 Here we show the planet luminosity budget vs. time for a representative example thermal evolution model with 1% H/He on a 5 $M_{\oplus}$ planet, receiving 100 $F_{\oplus}$ from a sun-like star. The black solid line shows the overall cooling rate while the dotted and dashed lines show the cooling rate of the rock/iron core and the heating from radioactive decay, respectively. The solid gray line shows the cooling rate if we ignore radioactivity and the need to cool the core. This clearly demonstrates the need to include these terms when calculating the thermal evolution of sub-Neptune like planets.

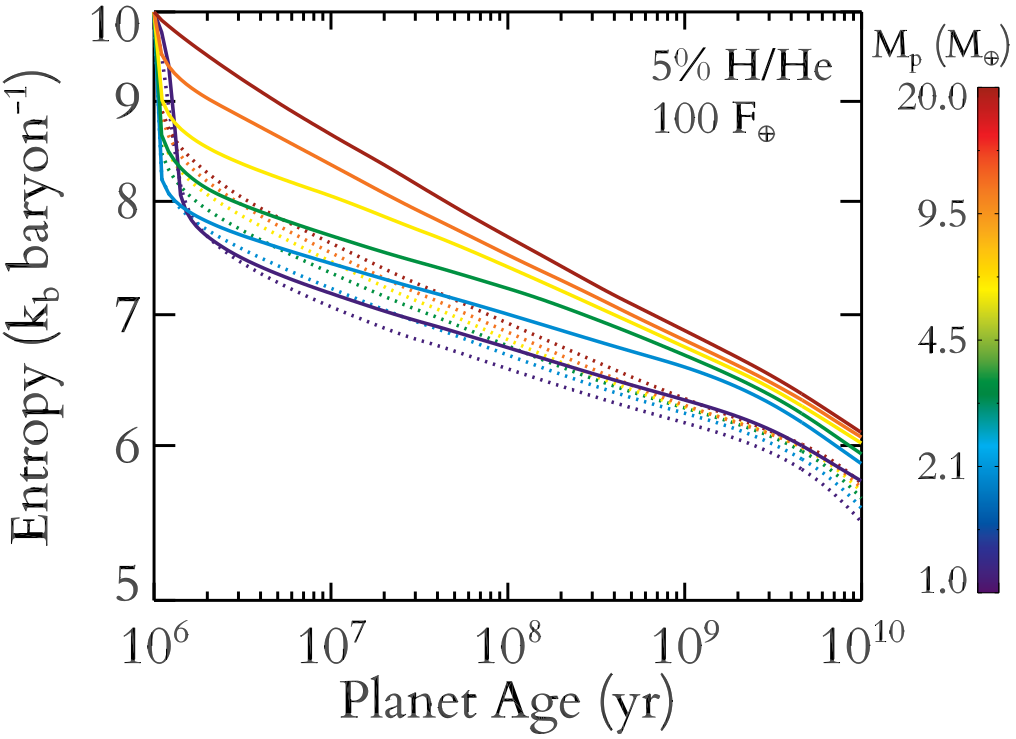

Figure 4.4 Shown is an example calculation in which all models start at the same young age and initial specific entropy. Internal specific entropy in the H/He envelope vs. time is shown for various planet masses. Solid lines show enhanced opacity, while dotted show solar metallicity. Planets start with large initial entropy, then rapidly cool. By 10-100 Myr, the models are insensitive to the choice of initial entropy. Low-mass planets experience more rapid cooling, leading to the flat mass-radius curves seen in Figure 4.1. Solar metallicity models cool rapidly at young ages and then experience more gradual cooling, while enhanced opacity models cool more steadily at all ages.

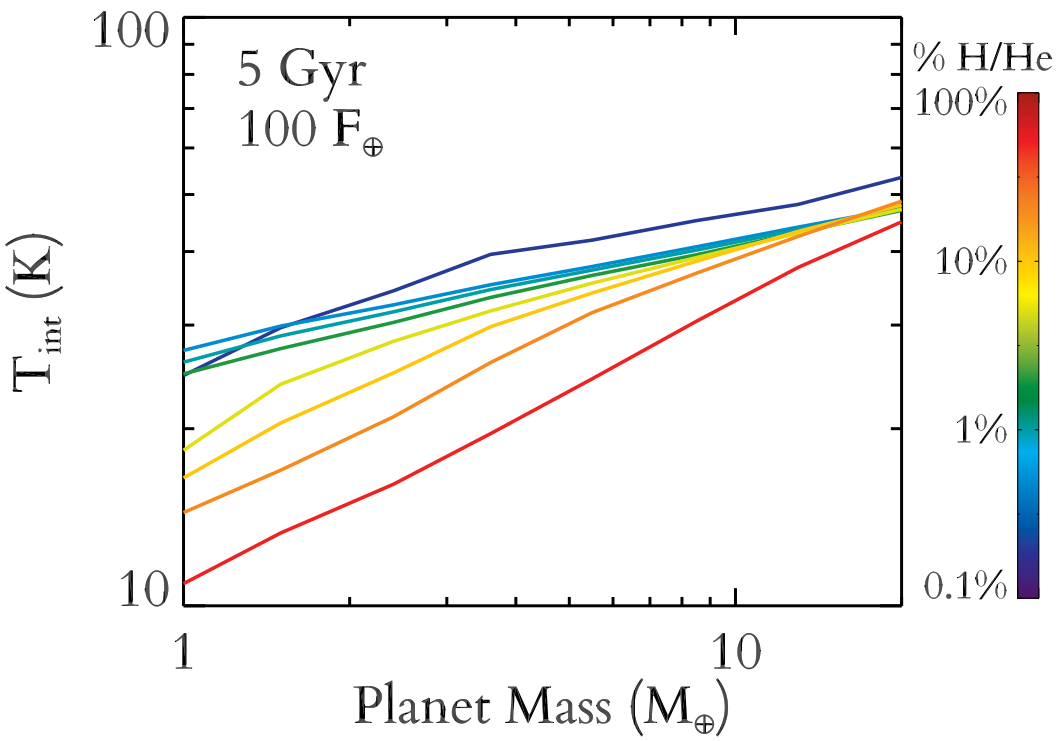

Figure 4.5 Intrinsic temperature $T_{\rm int}$, i.e., the equivalent blackbody temperature a planet's net outgoing flux, vs. planet mass for 5 Gyr old planets receiving 100 $F_\oplus$ with enhanced opacity atmospheres. Colors show different H/He envelope fractions. Clearly, by several Gyr lower-mass planets are significantly colder than higher mass planets. This demonstrates the need to perform full thermal evolution calculations. Simply assuming a fixed luminosity per mass will greatly overestimate the size of planets below $\sim 5\,M_\oplus$.

In fact, searching through the literature will show a wide range of mass-radius curves with very different behavior at low masses (e.g., Lissauer *et al.*, 2011a; Rogers *et al.*, 2011; Lopez *et al.*, 2012). Although, all the models tend to agree above $\sim$10-20 $M_{\oplus}$, there can be large disagreements below $\sim$5 $M_{\oplus}$. In some cases, radius decreases with decreasing mass in much the same way as the Earth-like mass radius curves in Figure 4.1. In other cases, the radius increases to implausibly large sizes due to the planet's lower gravity (Rogers *et al.*, 2011). Generally, these models face one of two limitations. Either they ignore the contributions of the rock/iron core to the thermal evolution, i.e., the need to cool the core and heating from radioactive decay, or they do not perform an evolution calculation at all and instead use static structure models in which the internal energy of the planet is treated as a free parameter.

For the Neptune and sub-Neptune sized planets that we are focusing on here, $\sim$90-99% of a planet's mass is contained in the rock/iron core. Ignoring the effects of that core on the thermal evolution will significantly underestimate these planet's cooling timescale, and therefore its radius. This is a common simplification with thermal evolution models that, like our own, were originally developed to model massive gas giants, where the core has a negligible impact on the overall thermal evolution. The importance of these effects, however, is clearly demonstrated in Figure 4.3, which shows the various contributions to the overall thermal evolution for a typical 5 $M_{\oplus}$, 1% H/He sub-Neptune sized planet. At every age, the cooling luminosity of the planet is dominated by these core cooling and heating terms. At early times, the thermal evolution is largely regulated by the need to cool the rock/iron core with its relatively large heat capacity (Alfè *et al.*, 2002; Guillot *et al.*, 1995). At ages $\gtrsim$1 Gyr, radioactive heating also becomes comparable to the core cooling rate, thanks mostly due to the decay of

^{40}K (Anders and Grevesse, 1989). On the other hand, ignoring these terms leads to a planet that is $\sim$30-100$\times$ less luminous at late times, and underestimates the final radius by $\sim$0.5 $R_{\oplus}$. Some models (e.g., Mordasini *et al.*, 2012), make the compromise of including radiogenic heating but not including the effect of the core's heat capacity. This is much better than ignoring the core altogether, but as shown in Figure 4.3 both terms are important and this will lead to underestimating the radii of sub-Neptune planets, especially at ages $\lesssim$1 Gyr.

On the other hand, it is also quite common to use static internal structure models which do not track a planet's thermal evolution, but instead assume a fixed specific luminosity (i.e. power per unit mass), which is then treated as a free variable (Rogers *et al.*, 2011). This is a common simplification made when a small H/He envelope is added to detailed models of terrestrial planets, for which the cooling history is harder to determine, and has little impact on overall planet size (Valencia *et al.*, 2007). When calculating possible envelope fractions for a single planet (e.g., Rogers and Seager, 2010b), this is fine, so long as the resulting uncertainty in the internal energy is accounted for. However, when plotting iso-composition mass-radius curves, this leads to an unphysical upturn at low masses. Lower mass planets will of course have lower gravities and larger scale heights, so assigning them the same specific luminosities as more massive planets will lead to much larger envelopes.

In reality though, lower mass planets tend to be colder at almost all ages. Partly this is due to their low gravities which slightly increases the rate of radiative transfer through their atmospheres (Fortney *et al.*, 2007). Mostly, however, it is simply due to the fact that lower mass planets have a higher ratio of radiating surface areas to their total internal energies. Thermal evolution will naturally result in planets that have cooling timescales comparable to their ages.

Since all other things being equal, lower mass planets will have shorter cooling timescales, their H/He envelopes will cool and contract slightly more to compensate.

These results are summarized in Figures 4.4 and 4.5. Figure 4.4 shows various cooling curves for the internal entropy in the H/He envelope. Planets start with large initial entropy, and therefore radii. As expected, models cool rapidly until their cooling timescale is comparable to their age. As in Figure, 4.2 solar metallicity models cool rapidly for their first $\sim$10 Myr and then contract more slowly. The enhanced opacity models, on the other hand, cool more steadily throughout their history. Eventually, the enhanced opacity models must also cool and contract and by several Gyr they have largely erased any differences with the solar models. At the same time, there is a slight change in the cooling rates due to the decay of ^{40}K.

Figure 4.5 shows the end result of this evolution. Here we show planetary intrinsic temperature $T_{\rm int}$ versus planet mass for various H/He envelope fractions for 5 Gyr old planets receiving 100 $F_{\oplus}$. As we can see, by 5 Gyr, low mass planets are always significantly cooler than higher mass planets at the same envelope fractions, regardless of H/He fraction or atmosphere metallicity.

Combined with the fact lower mass planets have slightly smaller rock/iron cores (equation (4.2)) this increase in cooling counter balances the fact that lower mass planets have lower gravities and produces the flat mass-radius curves seen in Figure 4.1. So long as a planet has enough of an envelope that $R_{\rm env} \gtrsim R_{\rm core}$, then equations (4.2) and (4.4) will roughly balance and iso-composition mass-radius curves will be quite flat. This typically happens for planets that are $\gtrsim$1% H/He or $\gtrsim$2.5 $R_{\oplus}$. Thus for most of *Kepler*'s Neptune and sub-Neptune sized planets, radius is nearly independent of planet mass and is instead a direct measure of bulk

H/He envelope fraction.

It has of course long been known that the mass-radius relationship should be flat for non-inflated giant planets (e.g., Fortney *et al.*, 2007). What is remarkable here, is that this is true even when the H/He envelope is a small fraction of a planet's mass. Moreover, it is for a different reason than in giant planets. For Jupiter mass planets and brown dwarfs the mass-radius relationship is flat because their interiors are highly degenerate and partially ionized (e.g., Zapolsky and Salpeter, 1969). That is not the case here, at the pressures and temperatures relevant for the interiors of Neptunes and sub-Neptunes, generally $\lesssim$1 Mbar and 10^4 K, the envelope is generally not degenerate. Even at the base of the H/He envelope for 20 $M_\oplus$ planet with a 20% envelope, the interior is only weakly degenerate, $\Theta = k_B \hbar^2 2 m_e (3\pi)^{2/3} T / n_e^{2/3} \sim 1$ (Nettelmann *et al.*, 2008).

4.4 The Mass-Composition Relation

Using our thermal evolution and structure models, we calculated H/He envelope fractions for all $\sim$200 confirmed planets with well determined masses, assuming a water-free interior. We excluded any planets which only have upper limits on mass or purely theoretical mass constraints. We used masses and radii from exoplanets.org (Wright *et al.*, 2011), except for where there are more recent values in the literature. For CoRoT-7b, the five inner Kepler-11 planets, and 55 Cancri e we used masses and radii from Hatzes *et al.* (2011), Lissauer *et al.* (2013), and Dragomir *et al.* (2013a), respectively. We exclude confirmed planets with analytical TTV mass estimates from Xie (2012) due to the degeneracy between planet mass and free ec-

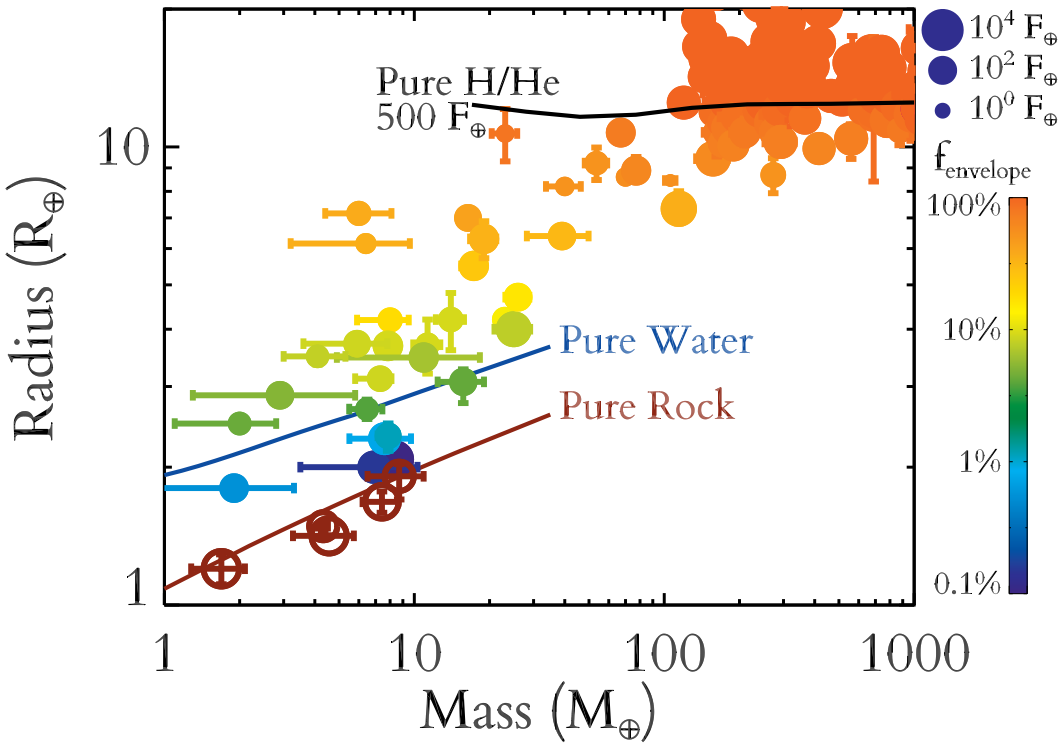

Figure 4.6 Planetary radius vs. mass for all 200 transiting planets with measured masses. Each planet is colored according to the fraction of its mass in a H/He envelope, assuming a water-free interior. Rust-colored open circles indicate potentially rocky planets. Points are sized according to the incident flux they receive from their parent stars, relative to $F_{\oplus}$ the flux that the Earth receives from the Sun. For comparison, we include theoretical mass-radius relations for pure silicate rock, pure water, and pure H/He at 500 $F_{\oplus}$. There is a very strong correlation between planetary radius and H/He envelope fraction, both of which are more weakly correlated with mass up to $\sim$100 $M_{\oplus}$.

centricity. For inflated hot Jupiters with radii larger than that of pure H/He, we simply assigned 100% H/He since such planets are beyond the scope of this work. Meanwhile, for potentially rocky planets like CoRoT-7b (Léger *et al.*, 2009; Queloz *et al.*, 2009) and Kepler-10b (Batalha *et al.*, 2011), we set strict upper limits on the size of any potential H/He envelope. Table A.2 summarizes the results for 44 planets with measured masses $< 100 M_{\oplus}$ and radii $< 12 R_{\oplus}$.

In order to calculate the uncertainty on these envelope fractions we included the affects of 1σ variations in the observed planet masses, radii, ages, and levels of irradiation. In addition, we included theoretical uncertainties on core iron fraction, core heat capacity, atmospheric albedo, etc., as described in Lopez *et al.* (2012). In general, uncertainties in the stellar radius and therefore the planetary radius are the dominant source of uncertainty. Typically this is followed by the unknown iron fraction in the core which is typically equivalent to a 0.1 $R_{\oplus}$ uncertainty in the radius for low-mass planets.

Figure 4.6 plots the current measured mass-radius relation with 1σ uncertainties for all confirmed transiting planets with measured masses up to $1000 M_{\oplus}$ and radii $20 R_{\oplus}$. The color of each point shows the H/He envelope fractions calculated by our models. Rust-colored open circles show potentially volatile-free rocky planets. Meanwhile, the size of the points correspond to the incident flux that each planet receives from its parent star, relative to $F_{\oplus}$, the incident flux that the Earth receives from the Sun.

Finally, we include three theoretical iso-composition curves. The rust colored curve shows pure silicate rock (specifically olivine). The dark blue curve corresponds to pure water worlds on a 10 day orbit around a 5 Gyr old Sun-like star, however, varying these details does not significantly change the curve. Finally, the black curve corresponds to pure H/He hot Jupiters

receiving 500 $F_\oplus$ (i.e., 500 times the current incident flux that the Earth receives from the Sun) from a 5 Gyr old Sun-like star. Roughly speaking, this last curve forms the dividing line between the inflated and non-inflated hot Jupiters.

Several features of the mass-radius relation are immediately apparent. As noted in Weiss *et al.* (2013), there is a roughly power-law increase in radius from $\sim$ 1-100 $M_\oplus$, above which radius saturates at approximately a Jupiter radius. Below $\sim 10\ M_\oplus$ there is a particularly large scatter in radius, with planets ranging from the potentially rocky to sub-Neptune sized planets with $\sim$3% H/He. For low-mass planets there is also an inverse correlation between radius and incident flux which may be due to photo-evaporative loss of H/He (Lopez *et al.*, 2012; Owen and Wu, 2013).

Above $\sim 100 M_\oplus$ we find the true gas giants including the highly inflated hot Jupiters. Here the correlation with incident flux is the reverse of that at low-mass with the most irradiated planets being extremely inflated. It is unclear why there do not appear to be any super-inflated hot Jupiters below $\sim 100 M_\oplus$, it is possible that such planets would be unstable to photo-evaporation or Roche-lobe overflow (Jackson *et al.*, 2010) or have a high mass fraction of heavy elements (Miller and Fortney, 2011).

Turning to the compositions of these planets, it is immediately clear that H/He envelope fraction is strongly correlated with both planet mass and radius. However, on closer inspection, where there is scatter in the mass-radius relationship it is the planet radius that correlates with envelope fraction. We argue here that planet radius is first and foremost a proxy for a planet's H/He inventory. The fact that both envelope fraction and radius correlate with mass is due to the fact that more massive planets are able accrete more gas during formation.

The radius saturates at $\sim$100 $M_\oplus$ because planet size does not simply increase with increasing H/He mass but rather with increasing H/He mass *fraction*. As shown in section 4.3, there is an approximately power-law relationship between the size of a planet's H/He envelope and the planets H/He mass fraction. A 100 $M_\oplus$ planet with a 10 $M_\oplus$ core, is already 95% H/He, as a result doubling the planet's mass will not significantly increase the H/He envelope fraction or the radius.

Figure 4.7 shows the observed sample of transiting planets except that here we have plotted H/He envelope fraction against radius. This clearly demonstrates the close relationship between the observed radius and the fundamental bulk composition, i.e., the fraction of it's mass in H/He vs. heavy elements. At a given radius, planet mass, shown by the color bar, can span up to a factor of $\sim$30. Nonetheless the scatter in H/He envelope fraction is typically only $\sim$0.3 dex. This is what we mean when we state that radius is primarily a proxy for composition.

Thus far, however, we have only considered dry interiors with H/He envelopes atop rock/iron cores. The gray shaded region in Figure 4.7 shows the effect of varying the water abundance of planets in our model. Using our three layer models we varied the water abundance of the interior from completely-dry, up to 90% of core mass, where by "core" we mean the combined mass of the rock and water layers. For clarity, we then fit power-laws to best fit radii and envelope fractions under both scenarios; the gray shaded region shows the area in between these fits. Clearly, allowing this degeneracy does slightly increase the scatter in the radius-envelope fraction relationship. Nonetheless, above $\sim$3 $R_\oplus$ this does not alter the conclusion that radius and H/He envelope fraction are intimately related.

As a result, this means that we can recast the mass-radius relationship in Figure 4.6

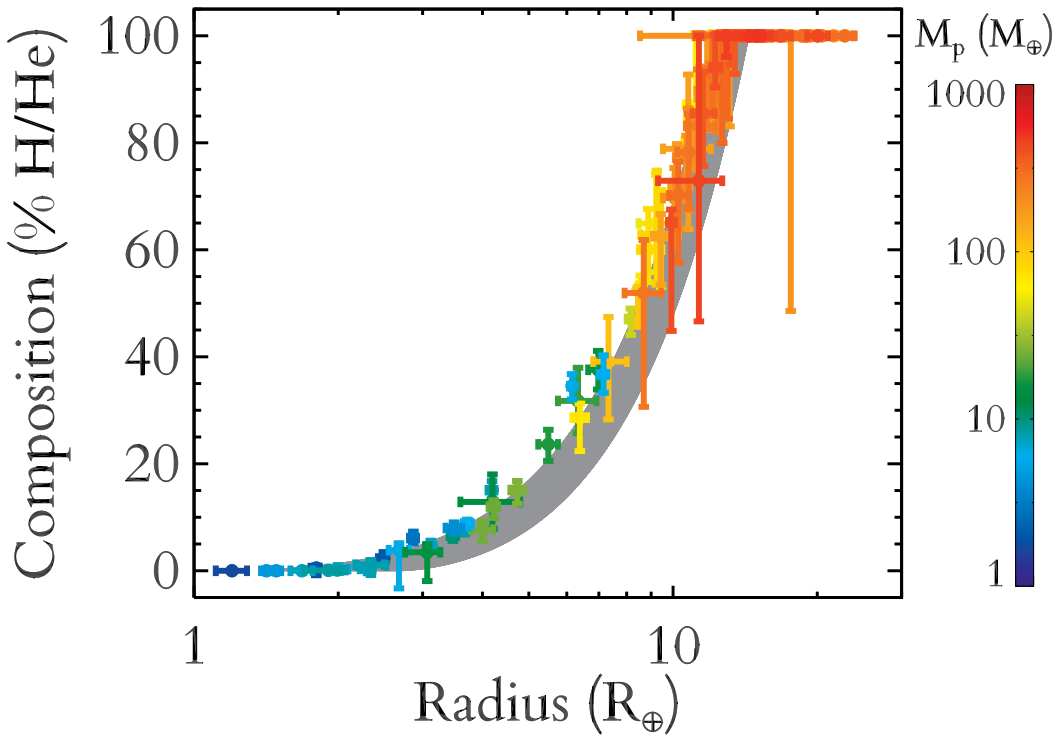

Figure 4.7 H/He envelope fraction vs. planet radius, for the 200 transiting planets shown in figure 4.6. Here each planet is color-coded according to its mass. The grey shaded region shows the effect of varying the water abundance of the interior, which lowers the amount of H/He at a given radius. Clearly there is a very tight correlation between size and H/He envelope fraction, lending credence to our claim that radius can be used as a proxy for planetary composition.

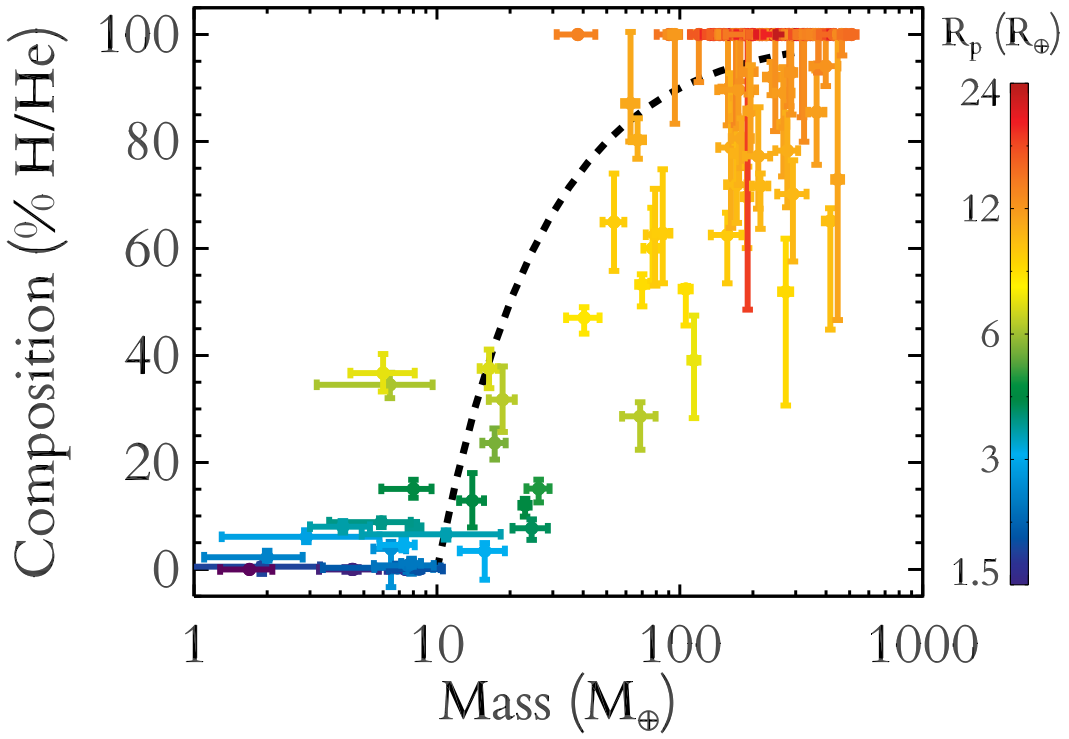

Figure 4.8 Similar to figure 4.6 but with H/He envelope fraction plotted against planetary mass, and color-coded by radius. Below ∼10 $M_\oplus$ there is a mix of rocky planets, possible water worlds, and sub-Neptunes with a few percent H/He. From ∼10-100 $M_\oplus$ there is a strong increase in both radii and H/He envelope fraction transitioning from Neptune sized planets with ∼10% H/He up to true gas giants that are almost entirely H/He. Above ∼100 $M_\oplus$ we find the familiar hot Jupiters, many of which have large inflated radii. The dashed black line shows a toy-model in which all planets have a 10 $M_\oplus$ core.

as a mass-*composition* relationship. This is shown in Figure 4.8. By doing this we have transformed the observable mass-radius relationship into one that is directly relatable to models of planet formation. Here we can clearly see that there is a fundamental change in the relationship around $\sim$10 $M_\oplus$. Below this planets typically have less than $\sim$5% of their mass in H/He with no clear relationship between envelope fraction and mass. Above this, however, most planets are roughly consistent with $\gtrsim$ 10 $M_\oplus$ of heavy elements and we see a steady rise in envelope fraction from sub-Neptunes up to gas giants.

These trends are all understandable in the light of the traditional core accretion model of planet formation (e.g., Hayashi *et al.*, 1985; Bodenheimer and Pollack, 1986). If a planet's rocky core becomes sufficiently massive, typically $\sim$5-10 $M_\oplus$, then its gravity becomes sufficiently strong to trigger runaway accretion from the disk. For comparison, the dashed black line in Figure 4.8 shows a the simple toy model in which all planets have 10 $M_\oplus$ core with solar metallicity H/He envelopes. This is of course a simplified view of planet formation. In reality there is considerable variation in disk mass, lifetime, metallicity, planet history, etc. all of which introduces considerable scatter into the mass-envelope fraction relationship. Most planets in Figure 4.8 lie to the right of the toy model, possibly indicating that they accreted additional planetesimals embedded in the nebula (Mordasini, 2013). Nonetheless, Figure 4.8 offers evidence for the core-accretion model of planet formation, at least for the close-in planets found by *Kepler*

4.5 The Super-Earth to Sub-Neptune Transition

Throughout this chapter, we have repeatedly used the terms super-Earth and sub-Neptune to refer to low-mass *Kepler* planets. What exactly is the difference between these classes of planets? For our purpose a sub-Neptune is any planet whose radius cannot be explained by a bare rock/iron model, i.e., it must have some sort of large optically-thick H/He or water envelope. Super-Earth on the other hand implies a more terrestrial planet, one that may have a solid or liquid surface and where the atmosphere, if any, contributes a negligible fraction to the planet's size. Although this may seem like semantics, one of the long-term goals of exoplanet science is to search for biomarkers in the transmission spectra of potentially habitable super-Earths. Whether or not a planet has a large H/He envelope tens of kbar deep has very important implications for habitability.

The current definition used by the *Kepler* mission is that planets 1.5-2.0 $R_\oplus$ are super-Earths, while planets 2.0-4.0 $R_\oplus$, are sub-Neptunes. These round numbers however, do not quite correspond to our more physically motivated definition of whether or not a planet has a thick envelope. Figure 4.9 plots the minimum H/He envelope fractions required by our models vs. planet mass for several different radii in the 1.5-2.5 $R_\oplus$ super-Earth/sub-Neptune transition region.

It is quite difficult to construct a 2.0 $R_\oplus$ planet that does not have some sort of thick envelope. Assuming an Earth-like interior, such planets would have to be 16.5 $M_\oplus$, to explain their size without any type of envelope. For a completely iron-free interior, it is possible to construct a 2.0 $R_\oplus$ that is only 11 $M_\oplus$. However, completely iron-free is probably not a realistic

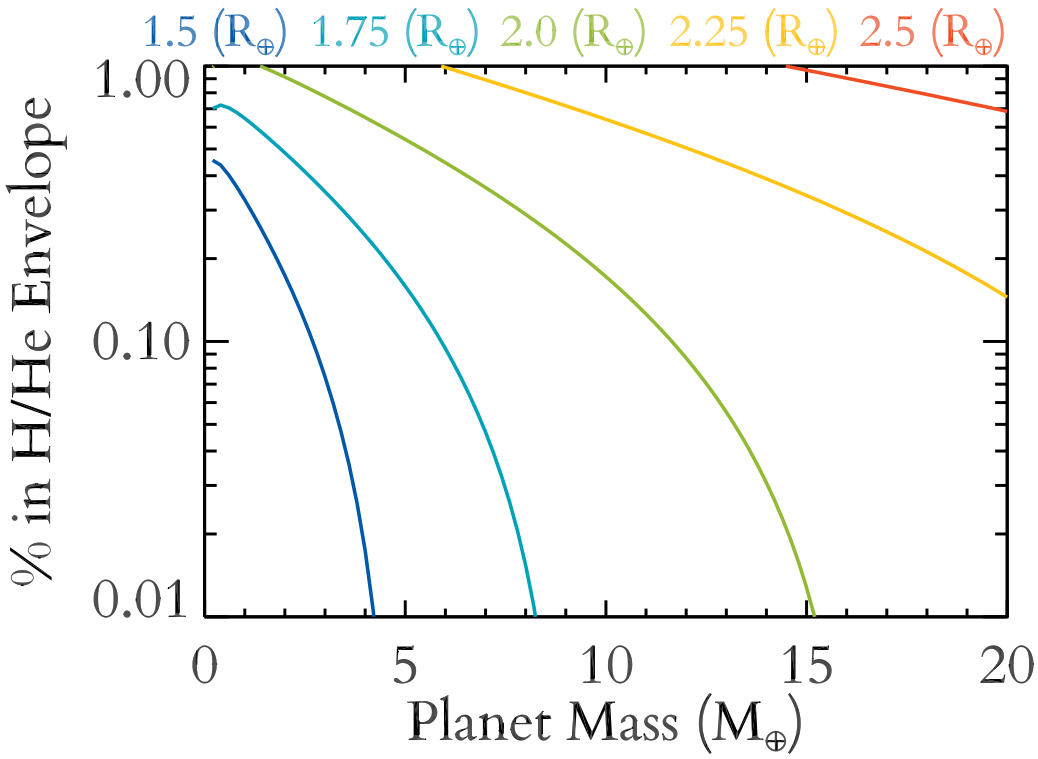

Figure 4.9 H/He envelope fraction vs. planet mass for super-Earth and sub-Neptune sized planets. Curves are color-coded according to planet radius ranging from 1.5-2.5 $R_{\oplus}$. Here we assume water-free sub-Neptunes with H/He envelopes atop Earth-like rocky cores.

composition for planets of several earth masses. Indeed both Kepler-10b and CoRoT-7b, may be slightly enhanced in iron compared to the Earth (Batalha *et al.*, 2011; Hatzes *et al.*, 2011).

This stands in contrast to the observed sample of likely rocky planets all of which are $<10\ M_\oplus$. It is possible that more massive rocky planets are yet to be found, however, the *Kepler* is essentially complete for 2.0 $R_\oplus$ within 100 days (Petigura *et al.*, 2013b). For follow-up RV and TTV mass measurements to have missed a population of $<10\ M_\oplus$ rocky planets, they would need to somehow be biased against more massive and therefore easier to detect planets. Moreover, there are basic arguments in core-accretion theory that lead us to expect that there should not be $\sim$20 $M_\oplus$ rocky planets. By the time a planet is $\sim$10 $M_\oplus$, its gravity should be sufficiently strong that it should be able to accrete a substantial H/He envelope from the disk (Ikoma and Hori, 2012), and for periods $\gtrsim$10 days be able to retain it against photo-evaporation (Chapter 3).

On the other hand, if we assume a more typical low-mass planet with a 5 $M_\oplus$ Earth-like core, then to be 2.0 $R_\oplus$ it would need 0.5% of its mass in a H/He envelope. This may not sound like much, but it corresponds to $\sim$20 kbars of hydrogen and helium, $\sim 20\times$ higher than the pressure at the bottom of the Marianias Trench. Moreover, the temperature at the bottom of such an envelope would be $\gtrsim$3000 K, even for ages of several Gyr. We believe that such a planet is more properly classified as a sub-Neptune. As a result, 2.0 $R_\oplus$ is more of a quite hard upper limit for the size of a envelope-free super-Earth and most of the planets between $\sim$ 1.75 and 2.0 $R_\oplus$ are likely to be H/He rich sub-Neptunes.

If 2.0 $R_\oplus$ is really the hard upper limit for the super-Earth/sub-Neptune transition, then what is the lower limit? As shown in Figure 4.9, for planets $\lesssim$1.5 $R_\oplus$ it is entirely possible

to explain their radii without any H/He. Moreover if such planets do have any H/He, then it must be $\lesssim$0.1% of their mass, even if we assume a maximally iron-rich core. This is small enough of envelope that the rock/iron core dominates the planet's size. Moreover, as shown in Chapter 3 and Owen and Wu (2013), such tenuous envelopes are quite-vulnerable to being completely photo-evaporated, at least at period $\lesssim$100 days. This does not exclude the possibility that 1.5 $R_\oplus$ cannot have large water envelopes, but it does suggest that they are unlikely to have large H/He envelopes.

To summarize, we can say that 2.0 $R_\oplus$ is likely a hard upper limit for the maximum size of envelope-free rocky super-Earths and 1.5 $R_\oplus$ is likely a lower limit for the minimum size of a H/He rich sub-Neptune. As a result, we suggest using $\sim$1.75 $R_\oplus$ rather than 2.0 $R_\oplus$ for the dividing line between these classes of planets.

4.6 Discussion

In Sections 4.3 and 4.4, we showed that planetary radius is to first order a proxy for a planet's envelope fraction above $\sim$2 $R_\oplus$. This means that the observed radius occurrence distribution for *Kepler* candidates found by Fressin *et al.* (2013) and Petigura *et al.* (2013b) is in reality an *envelope fraction* occurrence distribution for close-in planets at several Gyr. In particular, Fressin *et al.* (2013) and Petigura *et al.* (2013b) found that there is a sharp, roughly power-law like drop off in the frequency of planet occurrence above $\sim$3 $R_\oplus$, while below this there is a plateau in the planet occurrence rate down to at least 1 $R_\oplus$.

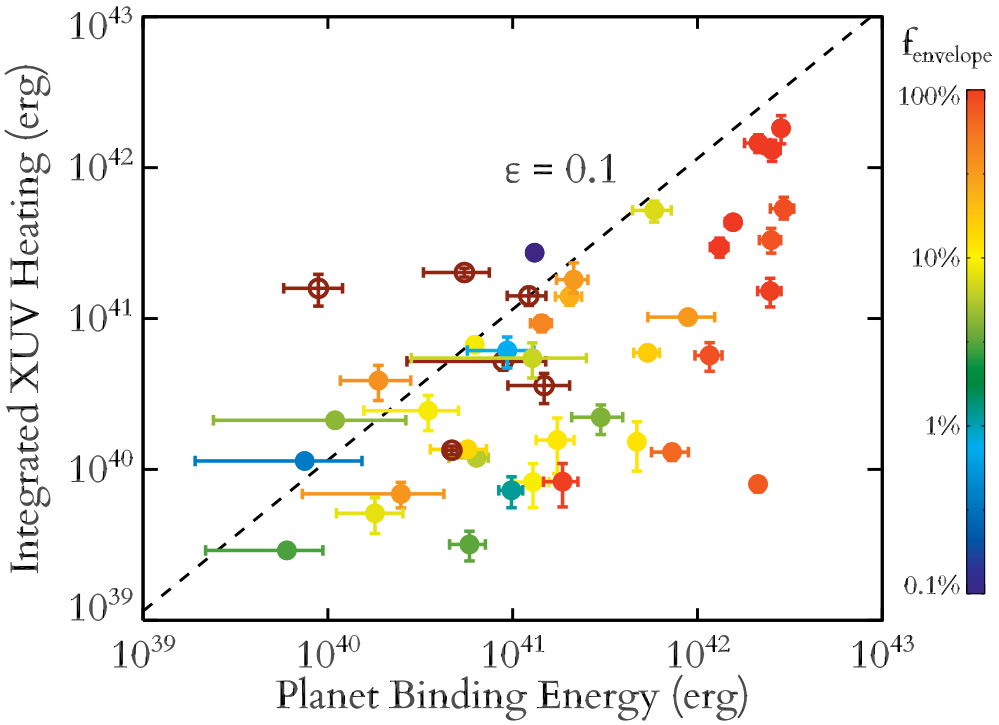

Figure 4.10 An updated version of the photo-evaporation threshold diagram from Lopez *et al.* (2012) and Lissauer *et al.* (2013). Integrated extreme UV heating received by a planet over its lifetime vs. current planetary binding energy for all transiting planets with well determined masses $\leq$100 $M_{\oplus}$, listed in Table A.2. Points are color-coded by their H/He envelope fractions, with rust-colored open circles indicating rocky planets. For comparison, the dashed line is the expected evaporation threshold from the coupled thermal evolution and photo-evaporation models of Lopez *et al.* (2012). There are no planets with significant H/He envelopes well above this threshold, indicating that the population of low-mass transiting planets has been significantly sculpted by photo-evaporation.

4.6.1 Planet Formation

This distribution makes sense in the light of traditional core accretion theory. The timescale for planetesimal collisions to form rocky planets is short compared to the typical lifetime of a disk and such planetesimals are preferentially concentrated deep in the star's potential well, so nature easily makes large populations of irradiated rocky planets (Chiang and Laughlin, 2013; Hansen and Murray, 2013).

At larger sizes, planets are limited by their ability to accrete a H/He envelope from the disk before the disk dissipates (Bodenheimer *et al.*, 2000; Ikoma and Hori, 2012; Mordasini *et al.*, 2012). In these models the accretion of the envelope is limited by the ability of the proto-planetary envelope to cool and contract. This makes it difficult to accrete larger initial H/He envelopes, particularly if the *Kepler* population formed in situ (Ikoma and Hori, 2012). It easier to form large planets further out, particularly beyond the snow-line where the increase in the local solid mass makes it easier to trigger runaway accretion to make a gas-giant. The relative scarcity of hot Jupiters found by Fressin *et al.* (2013) and Petigura *et al.* (2013b), is an indication that whatever migration mechanism brings in gas giants to orbits $\lesssim$100 days must be fairly rare.

One key puzzle, however, is the location of the break in the planet occurrence rate distribution. If it were due to a transition from a large rocky population to a sub-Neptune population, with planet occurrence declining with increasing envelope fraction, then one would expect the break to occur at $\sim$1.5-1.8 $R_\oplus$, which we have concluded is likely the maximum size for bare rocky planets. Instead the break occurs at 2.8 $R_\oplus$, indicating that the occurrence

plateau must include many volatile rich planets. Although 2.8 $R_\oplus$ is far too large for bare rocky planets, it is achievable for H/He free water-worlds. A 10 $M_\oplus$ planet with 80% of its mass in a water envelope would be $\sim$2.7 $R_\oplus$. As a result, it is at least possible that the break in the planet occurence distribution is a transition from an abundant population of rocky *and* water rich planets to a population with accreted H/He envelopes. Otherwise, models must explain why plateau should include a substantial population of planets with $\sim$1-3% of their mass in H/He envelopes before dropping off at larger envelope fractions.

One potential explanation is that perhaps the $\sim$2-3 $R_\oplus$ planets have hydrogen envelopes that were outgassed instead of accreted directly from the nebula. Elkins-Tanton and Seager (2008) showed that low-mass planets can outgas up to $\sim$5% of their mass after formation in H_2. However, this was only the case if the planets interiors were initially very wet, with $\sim$ half the mass of their initial mantles in water. This again requires a large of amount of water or other volatile ices to migrate to short period orbits.

4.6.2 H/He Envelopes Sculpted by Photo-Evaporation

It is also important to note that although the observed radius distribution may tell us the envelope fraction distribution of *Kepler* candidates today, this is not the same as the initial distribution the planets formed with. As shown in Chapter 2, Chapter 3, and Owen and Wu (2013) the observed *Kepler* population has likely been significantly sculpted by photo-evaporation. Close-in low-mass planets have likely lost a significant fraction of their initial H/He inventories, resulting in smaller radii today. Furthermore, less irradiated planets should be able to accrete larger initial H/He envelopes in the first place (Ikoma and Hori, 2012). As

more quarters of data are analyzed and the occurrence distribution pushes out to longer periods there should be a distinct increase in the abundance of Neptune and sub-Neptune sized planets.

Figure 4.10 shows an updated version of the photo-evaporation threshold diagram from Lopez *et al.* (2012) and Lissauer *et al.* (2013). This diagram compares the heating that a given planet receives from photo-ionizing radiation to the planet's current gravitational binding energy GM^2/R. This type of diagram was first proposed by Lecavelier Des Etangs (2007) for studying the effect of evaporation from hot-Jupiters and has since become a standard diagnostic tool for understanding the importance of evaporation (e.g., Lopez *et al.*, 2012; Jackson *et al.*, 2012; Owen and Jackson, 2012; Lissauer *et al.*, 2013; Zahnle and Catling, 2013). For each planet, we compute the integrated extreme UV flux that a planet receives at its semi-major axis from when it was 10 Myr old until now. To estimate the XUV output of from the star at ages > 100 Myr we use the empirical scaling-law $F_{\rm XUV} = 29.7(age/Gyr)^{-1.23}(a/AU)^{-2}\,{\rm erg\,s^{-1}\,cm^{-2}}$ from Ribas *et al.* (2005); at earlier ages we assume that the XUV irradiation saturates is in Lopez *et al.* (2012) based on x-ray observations from Jackson *et al.* (2012). We then multiply this integrated XUV flux by the planet's current cross-section $\pi R_{\rm p}^2$.

In order to compare to a more detailed model, we include the expected evaporation threshold predicted by our coupled thermal evolution and evaporation model from Lopez *et al.* (2012). This accounts for changes in the planet's size over its lifetime due to both thermal evolution and evaporation. This model is defined by a photo-evaporation efficiency ϵ, i.e., the fraction of the incident XUV flux that is converted into useful work to remove mass. That this threshold lies so close to the one-to-one line is a coincidence, the 10% evaporation efficiency is conter balanced by the fact that planets were 2-3 times larger when the were young and most

evaporation was taking place (Lopez *et al.*, 2012).

Figure 4.10 shows that the population of highly-irradiated low-mass planets have likely had their H/He envelope fractions, and therefore their radii, significantly sculpted by photo-evaporation. It is worth noting that since we first published a version of this diagram in (Lopez *et al.*, 2012), the sample size has nearly doubled including the discovery of extremely low-density planets like Kepler-79d (Jontof-Hutter *et al.*, 2013). Nonetheless, there are still no observed transiting planets with substantial H/He envelopes that lie above the predicted evaporation threshold. Of the planets that do lie above the threshold two, Kepler-10b and Kepler-78b, are likely rocky (Howard *et al.*, 2013; Pepe *et al.*, 2013), and the third, 55 Cancri e, likely has steam envelope (Gillon *et al.*, 2012). All three of these planets, and many of the Earth-sized *Kepler* candidates, are consistent with being the evaporated remnants of sub-Neptunes that initially had H/He envelopes.

Consequently, hoto-evaporation has important implications for current efforts to measure eta-Earth (e.g., Petigura *et al.*, 2013a), the frequency of Earth sized planets in the habitable zones of Sun-like stars. The *Kepler* survey is highly incomplete for Earth-sized planets on orbital periods longer than $\sim$200 days (e.g., Petigura *et al.*, 2013b,a). If most of Kepler's short-period Earth-sized candidates are in fact the photo-evaporated remnants of former sub-Neptunes, then current efforts to extrapolate the frequency of these candidates to longer orbital periods, where evaporation becomes much less effective (Owen and Jackson, 2012), will significantly overestimate the frequency of Earth-sized planets.

Another potential effect of photo-evaporation is the opening up of an "evaporation valley" in the radius-flux distribution (Lopez and Fortney, 2013a; Owen and Wu, 2013). Photo-

evaporation makes it less likely that planets will survive with envelopes $\lesssim$1% of their mass if they are on highly irradiated orbits. Planets will tend to either retain more substantial envelopes, or lose them entirely. More work needs to be done to carefully search for such a deficit, however there are some preliminary indications that it may exist. Both the raw candidate distribution (Owen and Wu, 2013), and a well-studied sample of M-dwarfs (Morton and Swift, 2013), appear to show a slight dip in the frequency of planets at $\sim$2 $R_{\oplus}$. Such hints are still preliminary, but if real this has important implications for constraining the envelope fractions of the *Kepler* population, since any large variation in the water fraction of close-in planets will tend to erase such a feature (Chapter 3). Using the models presented here, it is possible to instead study the *Kepler* envelope fraction distribution, which should aid in detecting any such "evaporation valley."

4.7 Chapter Summary

One of the key strengths of the thermal evolution models used here is that they allow us to predict the radius of a planet as a function of mostly observable parameters; namely, planet mass, incident flux, age, and envelope fraction. For Neptune and sub-Neptune size planets, we showed in section 4.3, that the effect of varying planet mass or incident flux on the radius is an order of magnitude smaller than the effect of varying the fraction of a planet's mass in a H/He envelope. In section 4.3.2, we described how this flatness in iso-composition mass-radius curves arises as a natural result of our thermal evolution models. As a result of these features, planetary radius is to first order a proxy for the H/He inventory of sub-Neptune and larger planets, almost

independent of their mass. In section 4.4 we showed the close connection between radius and envelope fraction for the observed population of transiting planets with measured masses. We then demonstrated how our models allow us to recast the observed mass-radius distribution as a mass-*composition* relationship, allowing a more direct comparison to models of planet formation and evolution.

Chapter 5

Further Applications and Prospects for the Future

5.1 Further Applications of the Models

In addition to the works described in Chapters 2, 3, and 4 our models have been used in a number of other studies for which I was a coauthor. Our thermal evolution models were used to determine possible planetary compositions for the discovery of many of *Kepler*'s most exciting multi-planet systems. This includes both the initial discovery (Lissauer *et al.*, 2011a) and subsequent follow-up (Lissauer *et al.*, 2013) of the incredibly rich six-planet Kepler-11 system, which is explored in great detail in Chapter 2. Likewise, our models were used to estimate H/He envelope fractions for the initial discovery of the two-planet Kepler-36 system (Carter *et al.*, 2012), which is further explored in Chapter 3.

In addition to determining H/He envelope fractions for planets with measured masses

and radii, it is also possible to use our models to rule out some compositions, even for planets without measured masses. In the case of extremely small highly irradiated transiting planets, we can use our photo-evaporation models to show that a planet can not retain a H/He or steam atmosphere for any possible mass. This technique was particularly useful in the discovery of Kepler-37b, the first sub-Mercury sized extrasolar planet (Barclay *et al.*, 2013). In Barclay *et al.* (2013) we showed that even if Kepler-37b formed with the maximum possible steam envelope given its radius, it would have lost that envelope in <10 Myr. By showing that the planet had to have a rocky composition, we were also able to set a minimum planetary mass of 0.01 $M_{\oplus}$, similar to the mass of our Moon. This minimum mass, combined with Kepler-37b's 13 day orbit, means that the planet is sufficiently massive to dynamically clear its orbit. Therefore despite being smaller than any planet in our Solar System, Kepler-37b is not a dwarf planet but instead the smallest known planet.

In addition to studies of individual systems, the grid of thermal evolution models described in Chapter 4 have been made publicly available and have been used by several authors (e.g., Lugar et al. in prep, Masuda, 2014). In particular, these models have been used extensively by my collaborator Angie Wolfgang to constrain the distribution of H/He envelope fractions among *Kepler* candidates on short-period orbits (Wolfgang & Lopez in prep.). This project takes advantage of the tight correlation between planet size and current H/He envelope fraction, for planets >3 $R_{\oplus}$, as discussed in Chapter 4. Using hierarchical Bayesian modeling, it is possible to marginalize over the uncertain mass distribution and derive composition posteriors for *Kepler* candidates, even without individual mass measurements. This is essential since the vast majority of *Kepler* candidates will never have individual mass determinations. Most are

in singly transiting systems around faint stars, making it impossible to determine masses from either TTVs or the Radial Velocity. In particular, Wolfgang & Lopez (in prep) is focused on determining the transition between purely rocky and volatile rich planets for a sample of *Kepler* candidates with orbital periods less than 25 days.

5.2 Future Improvements to the Models

5.2.1 Improved Photo-Evaporation Efficiencies

In order to understand the evolution of highly-irradiated volatile-rich planets, a detailed and reliable planetary evaporation model is needed. A key limitation of our current model is the assumption of a fixed photo-evaporation efficiency. This is an often-used approximation that parametrizes the fraction of the incident XUV energy that is converted into useful work to remove mass from a planet. For super-Earth and sub-Neptune sized planets receiving $\sim$10-1000$\times$ more incident flux than the Earth, this efficiency should typically be $\sim$10% (e.g., Ribas *et al.*, 2005; Sanz-Forcada *et al.*, 2011; Owen and Wu, 2013). Fortunately, this range of parameter space covers most of planets and candiates found by *Kepler*, including those examined in Chapters 2 and 3.

In reality, however, the photo-evaporative efficiency is set by the details of ionization balance and XUV heating and cooling in a planet's thermosphere. For highly irradiated planets in the hydrodynamic limit, the evaporative wind begins at the XUV photosphere, the point at which a planet's upper atmosphere becomes optically thin to photo-ionizing radiation (e.g., Yelle, 2004; Murray-Clay *et al.*, 2009; Owen and Jackson, 2012). Typically, this occurs at

pressures around $\sim$1 nbar (Murray-Clay *et al.*, 2009). Beyond this point the evaporative wind accelerates until it eventually passes through a sonic point and ceases to be in causal contact with the planet (e.g., Yelle, 2004; Murray-Clay *et al.*, 2009; Owen and Jackson, 2012). However, in between the XUV photosphere and the sonic point, much of the incident XUV energy gets re-radiated into space due to recombination cooling and x-ray metal lines, particularly those of carbon and oxygen (Owen and Jackson, 2012). It is this XUV radiative cooling that sets the photo-evaporation efficiency. As a result, the evaporation efficiency should depend sensitively on a planet's level of irradiation, metallicity, and the scale-height in the evaporative wind.

For example, it is known that on extremely irradiated orbits (orbital periods $\sim$3 days or less), the efficiency should decrease significantly due to a sharp rise in recombination cooling (e.g., Murray-Clay *et al.*, 2009; Owen and Jackson, 2012). Likewise as a planet ages and its gravity increases, the efficiency should decrease due to the decreasing scale height in the planet's upper atmosphere (Owen and Wu, 2013).

Thus far, most photo-evaporation models have either focused either on the early Solar System or on large hot Jupiters with solar composition atmospheres. However, solar composition may be a poor approximation, since low-mass planets like sub-Neptunes may have atmospheres that are highly enriched in astrophysical metals (Fortney *et al.*, 2013). Indeed, in the Solar System the atmospheres of Uranus and Neptune are known to be $\sim$100$\times$ more abundant in carbon than in than the Sun (Fortney *et al.*, 2011b). Some planets, like 55 Cnc e and Kepler-11b, may even have pure steam atmospheres (Lopez *et al.*, 2012). The effects of such metal-rich atmospheres on evaporation are not yet well understood. In general, the mass loss efficiency should decrease in metal-rich atmospheres due to a decrease in scale height and an

increase in cooling by carbon and oxygen (Owen and Jackson, 2012). Modeling these effects in detail will be a major focus of future work.

5.2.2 Including Tidal Evolution

If some planets form far from their current orbits, then they must somehow migrate in to their current highly irradiated orbits. One possibility is that planets migrate in on circular orbits due to torques raised in the proto-planetary disk (e.g., Ida and Lin, 2010; Mordasini *et al.*, 2009). Alternatively, planets may scatter onto highly eccentric orbits due to multi-planet interactions (e.g., Wu and Lithwick, 2011).

Close-in planets on eccentric orbits will experience enormous tidal interactions with their host stars (e.g., Jackson *et al.*, 2010). Over time this will cause a planet's orbit to circularize; however, in the process an enormous amount of heat, comparable to the planet's binding energy, can be deposited deep in a planet's interior, significantly inflating a planet's size (Jackson *et al.*, 2010). This increased radius will, in turn, translate into a larger photo-evaporative mass loss rate. Thus, if planets typically scatter in on eccentric orbits, then they should be significantly more vulnerable to photo-evaporation than if they had migrated in on circular orbits.

Moreover, since the strength of tidal heating is a strong function of orbital period, tidal heating should steepen the period dependence of the photo-evaporation threshold in Chapter 2. This means that we might be able to use the period dependence of photo-evaporation to constrain the initial eccentricity distribution of the *Kepler* candidates and therefore whether they underwent planet-planet scattering.

Likewise, the tidal history of a planet will depend strongly on its thermal evolution.

At young ages, the rocky cores of sub-Neptunes will be fully molten due to the initial heat from formation (Lopez and Fortney, 2013b; Henning *et al.*, 2009). These initially molten cores will have a low viscosity leading to long tidal evolution timescales and relatively little tidal heating (Henning *et al.*, 2009). Eventually, however, a sub-Neptune's rocky core will cool enough for the mantle to begin to solidify (Lopez and Fortney, 2013b; Henning *et al.*, 2009). When this happens the mantle viscosity will increase by orders of magnitude, leading to rapid circularization and much higher tidal heating rates (Henning *et al.*, 2009). This tidal heating will in turn feed back into the thermal evolution, delaying the solidification of the mantle. As result, there should be continual feedback between the thermal, tidal, and evaporative evolution of short-period sub-Neptunes. We plan on exploring these effects by coupling our photo-evaporation and thermal evolution models with the visco-elastic tidal heating models of Henning *et al.* (2009).

5.3 Prospects and Challenges for the Future

Below we examine the future prospects for understanding the compositions and origins of sub-Neptune and super-Earths. We discuss the role of new transiting planet discovery missions like *K2*, *TESS*, and *PLATO*. We examine the opportunities and pitfalls of characterizing exoplanet atmospheres with transmission spectroscopy. Finally, we examine the strength of population studies and the possibility of combining our planet evolution models with statistically modeling (e.g., Wolfgang & Lopez in prep.). We re-examine the evaporation valley found in Chapter 3, and discuss the resources that will be needed to find and interpret this feature. In particular, we discuss the need for more accurate stellar parameters for the *Kepler* target stars

and the need for a systematic determination the mass *distribution* of low-mass planets from radial velocity surveys.

5.3.1 New Instruments for Discovering Sub-Neptunes

Over the next decade a suite of new transiting exoplanet survey missions are scheduled to be launched in order to build and expand upon the legacy of *Kepler*. These efforts may begin later this year with the proposed *K2* mission concept. *K2* is a proposed extended mission currently under NASA Senior Review that would re-purpose the *Kepler* spacecraft to perform a new two to three year survey of stars near the ecliptic plane (Howell *et al.*, 2014).

Next in 2017 NASA plans to launch the *Transiting Exoplanet Survey Satellite* (*TESS*), an all-sky survey that will complete the census of hot sub-Neptune and larger planets around nearby G & K dwarfs brighter than 12th magnitude (Deming *et al.*, 2009; Ricker *et al.*, 2010). Unlike the original *Kepler* mission, *TESS* will only monitor each field for $\sim$30 days, focusing on the discovery of nearby short-period planets, rather than on long-term planet monitoring or on the statistics of planets in the habitable zone (Deming *et al.*, 2009; Ricker *et al.*, 2010). However, because *TESS* is an all-sky survey it will cover $\sim 400\times$ the area of *Kepler*, enabling it to find many more planets around nearby bright stars that can be characterized with both ground and space-based follow-up observations (Deming *et al.*, 2009; Ricker *et al.*, 2010).

K2 meanwhile, represents an excellent middle-ground between the primary *Kepler* mission and *TESS*. By observe multiple $\sim$100 sq. degree fields for 75 days each, *K2* will find smaller and longer period planets than TESS while still observing enough of the sky to provide some candidates around bright stars suitable for follow-up observations. Moreover, due to its

balance between coverage area and depth of detection *K2* is particularly well-suited to finding small short-period planets around M-dwarfs (Howell *et al.*, 2014). Such planets are particularly valuable because their frequent transits and favorable planet-to-star size ratios make it much easier to obtain high quality transmission spectra (e.g., Miller-Ricci *et al.*, 2009; Charbonneau *et al.*, 2009).

Finally, in 2024 ESA plans to launch the *Planetary Transits and Oscillations of stars* (*PLATO*) mission. With 34 separate small aperture refracting telescopes, *PLATO* will have a truly enormous field of view, observing 2232 sq. degrees per pointing (Rauer *et al.*, 2013). This is over $20\times$ larger than the original *Kepler field* and represent over 5% of the entire sky. Through a combination of multi-year long pointings and "step-and-stare" short pointings, *PLATO* will observe over one million stars, with particular focus on finding small, potentially rocky planets around bright, magnitude 4-11, sun-like stars (Rauer *et al.*, 2013). Moreover, *PLATO* will observe its entire field on a 25-32 second candence (Rauer *et al.*, 2013), compared to *Kepler*'s $\sim$30 minute cadence (Borucki *et al.*, 2010). Combined with the brightness of the target stars, this means that *PLATO* will be able to obtain highly accurate stellar properties from asteroseismology for the vast majority of its sample (Rauer *et al.*, 2013).

5.3.2 Observational Opportunities for Characterizing Atmospheres

One of the key limitations of the primary *Kepler* mission was that in order to obtain a sufficiently large sample size it was forced to limit itself to observing a single field in the thick disk of the galaxy (Borucki *et al.*, 2010). As a result, the target sample is almost entirely an old stellar population, with very few stars $\lesssim$1 Gyr old (Huber *et al.*, 2014). By performing all-

sky or ecliptic plane surveys these future missions will include a much larger fraction of young stars in the galactic plane or in nearby open clusters. This opens up the possibility of catching young low-mass planets in the midst of undergoing catastrophic evaporation. Moreover, since these planets will be around relatively bright, nearby targets it may be possible to characterize evaporative outflows with instruments like HST CoS and STIS; something that has so far only been possible for hot Jupiters (e.g., Lecavelier des Etangs *et al.*, 2004; Vidal-Madjar *et al.*, 2003; Ehrenreich *et al.*, 2012).

These upcoming transit surveys will also provide a wealth of new targets for obtaining high quality spectra of the atmospheres of low-mass exoplanets (Deming *et al.*, 2009). As discussed in Chapters 2 and 4, it is difficult to constrain the compositions of sub-Neptunes by measuring masses and radii due to degeneracies between the amounts of rock, iron, water, and H/He in a planet's interior. Although planetary radii can be used to constrain the fraction of a planet's mass in it's H/He envelope (Chapter 4), mass and radius alone cannot constrain the fraction of a planet's mass in water or other volatile ices. Transmission and emission spectroscopy are excellent tools to break this degeneracy and help constrain the compositions of exoplanetary atmospheres (e.g., Miller-Ricci *et al.*, 2009). The depth of atmospheric absorption features is primarily determined by the scale height and therefore the mean molecular weight of the atmosphere (Miller-Ricci *et al.*, 2009). As a result, spectroscopy is potentially an excellent way to determine the composition of sub-Neptune atmospheres (Miller-Ricci *et al.*, 2009; Miller-Ricci and Fortney, 2010), which in turn provides constraints on the bulk compositions of those planets.

High signal-to-noise transmission and emission spectra have historically been lim-

ited to hot Jupiters (e.g., Charbonneau *et al.*, 2002; Deming *et al.*, 2005; Knutson *et al.*, 2008; Stevenson *et al.*, 2013). Recently, Wide Field Camera 3 (WFC3) on the Hubble Space Telescope has significantly improved the quality and resolution of these spectra (e.g., Deming *et al.*, 2013; Ranjan *et al.*, 2014). Moreover, future instruments like the Near InfraRed Spectrograph(NIRSpec, Posselt *et al.*, 2004) aboard the James Webb Space Telescope (Gardner *et al.*, 2006) promise the opportunity to achieve high S/N medium resolution spectra for even Earth-sized exoplanets (Deming *et al.*, 2009). Nonetheless, GJ 1214b (Charbonneau *et al.*, 2009) and HD 97658b (Dragomir *et al.*, 2013b) are currently the only sub-Neptune sized planets with a observed transmission spectra (e.g., Bean *et al.*, 2011; Désert *et al.*, 2011; Croll *et al.*, 2011; Berta *et al.*, 2012; Kreidberg *et al.*, 2014; Knutson *et al.*, 2014b). Rather than a lack of observing facilities, the field is currently limited by a lack of targets around sufficiently bright nearby targets. Correcting this mismatch is one of the primary goals of upcoming surveys like *TESS* and *K2* (Deming *et al.*, 2009; Howell *et al.*, 2014).

5.3.3 Challenges in Interpreting Spectra

Unfortunately, even with access to high quality atmospheric spectra, it can be difficult to constrain atmospheric abundances. High altitude clouds or photochemical hazes can completely flatten planetary transmission spectra, mimicking the effects of high mean molecular weight (e.g., Morley *et al.*, 2013; Fortney *et al.*, 2013; Knutson *et al.*, 2014a; Kreidberg *et al.*, 2014). At equilibrium temperatures from $\sim 500-2000$ K there are a wide range sulfide, metal, and silicate clouds that can condense in the observable region of a planet's atmosphere (Fortney, 2005; Morley *et al.*, 2012, 2013). Likewise it is possible that complex organic hazes may form

high up in many exoplanetary atmospheres due to UV photolysis of methane (e.g, Miller-Ricci Kempton *et al.*, 2012b; Morley *et al.*, 2013). High altitude clouds or hazes must be present in GJ 1214b (Miller-Ricci Kempton *et al.*, 2012b; Howe and Burrows, 2012; Morley *et al.*, 2013; Berta *et al.*, 2012; Kreidberg *et al.*, 2014), where despite an enormous community effort it is not possible to determine the atmospheric composition (Berta *et al.*, 2012; Kreidberg *et al.*, 2014).

Moreover, even in the absence of clouds, abundance retrieval from low-resolution spectra or broadband photometry can be highly degenerate (e.g., Line *et al.*, 2012, 2014; Hansen *et al.*, 2014). In the near infrared CH_4, NH_3, CO, CO_2, H_2O can all be important and this degeneracy is further complicated by the possibility of thermal inversions, non-Solar C/O ratios, or disequilibrium chemistry (e.g., Line *et al.*, 2012, 2014).

5.3.4 Harnessing The Power of Planet Population Studies

These challenges mean that for individual sub-Neptune planets, it will often be difficult or impossible to constrain their bulk water abundance and therefore their origin with either atmospheric spectra or mass and radius measurements. Rather than simply examining systems on an individual basis, this difficulty points to the importance of identifying diagnostic trends in the overall population of low-mass exoplanets.

In Chapter 3 we identified one such key diagnostic trend. In Section 3.5.1 we discussed the predicted "evaporation valley" in which planets should be relatively rare between the population of H/He rich sub-Neptunes, and the population of stripped rocky super-Earths. This occurrence valley corresponds to planets that have $\sim$0.1-1% of their mass in a H/He envelope. Although such tenuous envelopes are easily lost to photo-evaporation, they significantly in-

crease a planet's radius (Lopez *et al.*, 2012; Lopez and Fortney, 2013a,b; Owen and Wu, 2013). Consequently, planets should quickly shrink by $\sim$0.5 Earth radii as they lose the last few kbars of H/He from their envelopes (Lopez and Fortney, 2013a; Owen and Wu, 2013). However, this evaporation valley will only occur if most close-in planets contain relatively little water. If most hot Neptunes and sub-Neptunes form far from their current orbits, then water and other volatile ices should dominate their mass (e.g., Rogers *et al.*, 2011). Moreover, not all planets will contain the same amount of water. This will produce a range of core radii, smearing out any trends with radius and filling in the valley (Chapter 3). As a result, the depth of the evaporation valley can be used to diagnose whether or not most Neptunes and sub-Neptunes form in situ. If most Kepler planets form close to current orbits, then there should be a clear valley in the joint radius-flux distribution. On the other hand, if most of these planets form beyond the snowline then the valley should be filled in (Chapter 3).

In principle, it should be possible to directly fit for the depth of this evaporation valley as a way to constrain the initial distribution of water fraction among the *Kepler* sub-Neptunes and super-Earths (Lopez and Fortney, 2013a; Owen and Wu, 2013). This could be done using Bayesian statistical modeling tools similar to those used in Wolfgang & Lopez (in prep.), as discussed above in Section 5.1. Although this would not tell us the composition and origin of any individual planets, it could determine whether the population as whole primarily formed in situ with little or no volatile ices or if they formed and migrated from beyond the snowlines.

In practice, however, there are a number of issues that make these sort of statistical comparisons difficult. First and foremost is the need to correct the radius distribution of *Kepler* candidates for selection effects and pipeline completeness (e.g., Petigura *et al.*, 2013b,a;

Christiansen *et al.*, 2013). Although some biases like the geometric probability of transit are easy to correct for, others like the detection efficiency of the light-curve reduction pipeline are extremely difficult to characterize and usually require injection studies on synthetic populations (e.g., Petigura *et al.*, 2013b,a; Christiansen *et al.*, 2013).

Likewise, it is critical that transiting surveys and their follow-up observations establish a precise, reliable, and homogeneous set of stellar parameters. Transiting planet measurements only measure the size of a planet in relation to the size of its parent star. Given the close relationship between planet radius and H/He envelope fraction (Chapter 4), the uncertainty in stellar radius is typically the greatest source of uncertainty in deriving planetary compositions (Chapter 4). Unfortunately, the initial stellar parameters from the Kepler Input Catalog (KIC) included large uncertainties, typically $\gtrsim$10% in stellar radius (e.g., Huber *et al.*, 2014; Batalha *et al.*, 2013b). Moreover these stellar classifications were sometimes unreliable and contained systematic biases, particularly for later spectral types (e.g., Muirhead *et al.*, 2012). In some cases the KIC even confused low-mass M-Dwarfs with evolved red giants (e.g., Muirhead *et al.*, 2012; Huber *et al.*, 2013). Fortunately, there is a large on going community effort to obtain precise accurate stellar parameters for all the planet-hosting *Kepler* stars (e.g, Huber *et al.*, 2014). However, if we truly wish to understand the detection efficiency then it is important to obtain accurate stellar parameters for the entire target sample and not just those with detected transits. This will be easier for future surveys like *TESS* and *PLATO* since their rapid cadence and brighter target stars will make easier to obtain stellar parameters from stellar spectra and asteroseismology (Deming *et al.*, 2009; Ricker *et al.*, 2010; Rauer *et al.*, 2013); however, it will still require an enormous community effort.

Finally, it is also critical that the community obtain a careful understanding of the mass distribution of short-period sub-Neptune and super-Earth mass planets from radial-velocity surveys. Without mass determinations it is possible to constrain the present-day H/He envelope fractions of many planets (Wolfgang & Lopez in prep., Chapter 4). However, the photo-evaporation history of a planet depends sensitively on the mass of its core (Chapter 3). Therefore, if we wish to understand the original compositions of these planets after formation, it is essential that we understand their mass distribution. In general, however, radial velocity surveys have been optimized for maximizing the rate of individual planet discoveries rather than in understanding the overall mass radius distribution (Marcy *et al.*, 2014a,b).

Typically when a possible planet is first detected it is given high priority until a reliable mass is determined; meanwhile stars that fail to yield any planets are monitored less frequently. Often this decision process is entirely subjective. This introduces strong selection biases that are difficult to characterize and make it nearly impossible to determine the overall mass distribution of radial velocity planets. There is a need for a careful systematic radial velocity survey of Sun-like stars for relatively short period, $\lesssim$50 days, planets from $\sim$2-20 $M_{\oplus}$. This survey would need clear and reproducible target selection criteria, consistent monitoring of all targets, a well characterized reduction pipeline, and to include non-detection and marginal detections as well as confirmed planets.

Determining the nature and origin of *Kepler*'s sub-Neptunes and super-Earths will require a large collaborative effort. We will need careful thermal and photo-evaporative evolution models, combined with powerful statistical modeling and accurate and precise radius, mass, and period distributions that have been corrected for selection biases. Ultimately, we will

then be able to combine all of these disparate pieces together to determine the current and past compositions and directly constrain the formation of this exciting new class of planets.

Bibliography

Adams, F. C. Magnetically Controlled Outflows from Hot Jupiters. *ApJ* **730**, 27 (2011).

Agol, E.; Steffen, J.; Sari, R. and Clarkson, W. On detecting terrestrial planets with timing of giant planet transits. *MNRAS* **359**, 567 (2005).

Alfè, D.; Price, G. D. and Gillan, M. J. Iron under Earth's core conditions: Liquid-state thermodynamics and high-pressure melting curve from ab initio calculations. *Physical Review B* **65**, 165118 (2002).

Alibert, Y.; Mordasini, C. and Benz, W. Migration and giant planet formation. *A&A* **417**, L25 (2004).

Alibert, Y.; Mordasini, C. and Benz, W. Extrasolar planet population synthesis. III. Formation of planets around stars of different masses. *A&A* **526**, A63 (2011).

Anders, E. and Grevesse, N. Abundances of the elements - Meteoritic and solar. *Geochimica et Cosmochimica Act* **53**, 197 (1989).

Baraffe, I.; Alibert, Y.; Chabrier, G. and Benz, W. Birth and fate of hot-Neptune planets. *A&A* **450**, 1221 (2006).

Baraffe, I.; Chabrier, G.; Barman, T. S.; Selsis, F.; Allard, F. and Hauschildt, P. H. Hot-Jupiters and hot-Neptunes: A common origin? *A&A* **436**, L47 (2005).

Baraffe, I.; Selsis, F.; Chabrier, G.; Barman, T. S.; Allard, F.; Hauschildt, P. H. and Lammer, H. The effect of evaporation on the evolution of close-in giant planets. *A&A* **419**, L13 (2004).

Barclay, T.; Rowe, J. F.; Lissauer, J. J.; Huber, D.; Fressin, F.; Howell, S. B.; Bryson, S. T.; Chaplin, W. J.; Désert, J.-M.; Lopez, E. D.; Marcy, G. W.; Mullally, F.; Ragozzine, D.; Torres, G.; Adams, E. R.; Agol, E.; Barrado, D.; Basu, S.; Bedding, T. R.; Buchhave, L. A.; Charbonneau, D.; Christiansen, J. L.; Christensen-Dalsgaard, J.; Ciardi, D.; Cochran, W. D.; Dupree, A. K.; Elsworth, Y.; Everett, M.; Fischer, D. A.; Ford, E. B.; Fortney, J. J.; Geary, J. C.; Haas, M. R.; Handberg, R.; Hekker, S.; Henze, C. E.; Horch, E.; Howard, A. W.; Hunter, R. C.; Isaacson, H.; Jenkins, J. M.; Karoff, C.; Kawaler, S. D.; Kjeldsen, H.; Klaus, T. C.; Latham, D. W.; Li, J.; Lillo-Box, J.; Lund, M. N.; Lundkvist, M.; Metcalfe, T. S.; Miglio, A.; Morris, R. L.; Quintana, E. V.; Stello, D.; Smith, J. C.; Still, M. and Thompson, S. E. A sub-Mercury-sized exoplanet. *Nature* **494**, 452 (2013).

Batalha, N. M.; Borucki, W. J.; Bryson, S. T.; Buchhave, L. A.; Caldwell, D. A.; Christensen-Dalsgaard, J.; Ciardi, D.; Dunham, E. W.; Fressin, F.; Gautier, III, T. N.; Gilliland, R. L.; Haas, M. R.; Howell, S. B.; Jenkins, J. M.; Kjeldsen, H.; Koch, D. G.; Latham, D. W.; Lissauer, J. J.; Marcy, G. W.; Rowe, J. F.; Sasselov, D. D.; Seager, S.; Steffen, J. H.; Torres, G.; Basri, G. S.; Brown, T. M.; Charbonneau, D.; Christiansen, J.; Clarke, B.; Cochran, W. D.; Dupree, A.; Fabrycky, D. C.; Fischer, D.; Ford, E. B.; Fortney, J.; Girouard, F. R.; Holman, M. J.; Johnson, J.; Isaacson, H.; Klaus, T. C.; Machalek, P.; Moorehead, A. V.; Morehead,

R. C.; Ragozzine, D.; Tenenbaum, P.; Twicken, J.; Quinn, S.; VanCleve, J.; Walkowicz, L. M.; Welsh, W. F.; Devore, E. and Gould, A. Kepler's First Rocky Planet: Kepler-10b. *ApJ* **729**, 27 (2011).

Batalha, N. M.; Rowe, J. F.; Bryson, S. T.; Barclay, T.; Burke, C. J.; Caldwell, D. A.; Christiansen, J. L.; Mullally, F.; Thompson, S. E.; Brown, T. M.; Dupree, A. K.; Fabrycky, D. C.; Ford, E. B.; Fortney, J. J.; Gilliland, R. L.; Isaacson, H.; Latham, D. W.; Marcy, G. W.; Quinn, S. N.; Ragozzine, D.; Shporer, A.; Borucki, W. J.; Ciardi, D. R.; Gautier, III, T. N.; Haas, M. R.; Jenkins, J. M.; Koch, D. G.; Lissauer, J. J.; Rapin, W.; Basri, G. S.; Boss, A. P.; Buchhave, L. A.; Carter, J. A.; Charbonneau, D.; Christensen-Dalsgaard, J.; Clarke, B. D.; Cochran, W. D.; Demory, B.-O.; Desert, J.-M.; Devore, E.; Doyle, L. R.; Esquerdo, G. A.; Everett, M.; Fressin, F.; Geary, J. C.; Girouard, F. R.; Gould, A.; Hall, J. R.; Holman, M. J.; Howard, A. W.; Howell, S. B.; Ibrahim, K. A.; Kinemuchi, K.; Kjeldsen, H.; Klaus, T. C.; Li, J.; Lucas, P. W.; Meibom, S.; Morris, R. L.; Prša, A.; Quintana, E.; Sanderfer, D. T.; Sasselov, D.; Seader, S. E.; Smith, J. C.; Steffen, J. H.; Still, M.; Stumpe, M. C.; Tarter, J. C.; Tenenbaum, P.; Torres, G.; Twicken, J. D.; Uddin, K.; Van Cleve, J.; Walkowicz, L. and Welsh, W. F. Planetary Candidates Observed by Kepler. III. Analysis of the First 16 Months of Data. *ApJS* **204**, 24 (2013a).

Batalha, N. M.; Rowe, J. F.; Bryson, S. T.; Barclay, T.; Burke, C. J.; Caldwell, D. A.; Christiansen, J. L.; Mullally, F.; Thompson, S. E.; Brown, T. M.; Dupree, A. K.; Fabrycky, D. C.; Ford, E. B.; Fortney, J. J.; Gilliland, R. L.; Isaacson, H.; Latham, D. W.; Marcy, G. W.; Quinn, S. N.; Ragozzine, D.; Shporer, A.; Borucki, W. J.; Ciardi, D. R.; Gautier, III, T. N.;

Haas, M. R.; Jenkins, J. M.; Koch, D. G.; Lissauer, J. J.; Rapin, W.; Basri, G. S.; Boss, A. P.; Buchhave, L. A.; Carter, J. A.; Charbonneau, D.; Christensen-Dalsgaard, J.; Clarke, B. D.; Cochran, W. D.; Demory, B.-O.; Desert, J.-M.; Devore, E.; Doyle, L. R.; Esquerdo, G. A.; Everett, M.; Fressin, F.; Geary, J. C.; Girouard, F. R.; Gould, A.; Hall, J. R.; Holman, M. J.; Howard, A. W.; Howell, S. B.; Ibrahim, K. A.; Kinemuchi, K.; Kjeldsen, H.; Klaus, T. C.; Li, J.; Lucas, P. W.; Meibom, S.; Morris, R. L.; Prša, A.; Quintana, E.; Sanderfer, D. T.; Sasselov, D.; Seader, S. E.; Smith, J. C.; Steffen, J. H.; Still, M.; Stumpe, M. C.; Tarter, J. C.; Tenenbaum, P.; Torres, G.; Twicken, J. D.; Uddin, K.; Van Cleve, J.; Walkowicz, L. and Welsh, W. F. Planetary Candidates Observed by Kepler. III. Analysis of the First 16 Months of Data. *ApJS* **204**, 24 (2013b).

Bean, J. L.; Désert, J.-M.; Kabath, P.; Stalder, B.; Seager, S.; Miller-Ricci Kempton, E.; Berta, Z. K.; Homeier, D.; Walsh, S. and Seifahrt, A. The Optical and Near-infrared Transmission Spectrum of the Super-Earth GJ 1214b: Further Evidence for a Metal-rich Atmosphere. *ApJ* **743**, 92 (2011).

Berta, Z. K.; Charbonneau, D.; Désert, J.-M.; Miller-Ricci Kempton, E.; McCullough, P. R.; Burke, C. J.; Fortney, J. J.; Irwin, J.; Nutzman, P. and Homeier, D. The Flat Transmission Spectrum of the Super-Earth GJ1214b from Wide Field Camera 3 on the Hubble Space Telescope. *ApJ* **747**, 35 (2012).

Bodenheimer, P.; Hubickyj, O. and Lissauer, J. J. Models of the in Situ Formation of Detected Extrasolar Giant Planets. *Icarus* **143**, 2 (2000).

Bodenheimer, P. and Pollack, J. B. Calculations of the accretion and evolution of giant planets The effects of solid cores. *Icarus* **67**, 391 (1986).

Bonfils, X.; Gillon, M.; Udry, S.; Armstrong, D.; Bouchy, F.; Delfosse, X.; Forveille, T.; Jehin, E.; Lendl, M.; Lovis, C.; Mayor, M.; McCormac, J.; Neves, V.; Pepe, F.; Perrier, C.; Pollaco, D.; Queloz, D. and Santos, N. C. A hot Uranus transiting the nearby M dwarf GJ3470. Detected with HARPS velocimetry. Captured in transit with TRAPPIST photometry. *ArXiv e-prints* (2012).

Borucki, W. J.; Agol, E.; Fressin, F.; Kaltenegger, L.; Rowe, J.; Isaacson, H.; Fischer, D.; Batalha, N.; Lissauer, J. J.; Marcy, G. W.; Fabrycky, D.; Désert, J.-M.; Bryson, S. T.; Barclay, T.; Bastien, F.; Boss, A.; Brugamyer, E.; Buchhave, L. A.; Burke, C.; Caldwell, D. A.; Carter, J.; Charbonneau, D.; Crepp, J. R.; Christensen-Dalsgaard, J.; Christiansen, J. L.; Ciardi, D.; Cochran, W. D.; DeVore, E.; Doyle, L.; Dupree, A. K.; Endl, M.; Everett, M. E.; Ford, E. B.; Fortney, J.; Gautier, T. N.; Geary, J. C.; Gould, A.; Haas, M.; Henze, C.; Howard, A. W.; Howell, S. B.; Huber, D.; Jenkins, J. M.; Kjeldsen, H.; Kolbl, R.; Kolodziejczak, J.; Latham, D. W.; Lee, B. L.; Lopez, E.; Mullally, F.; Orosz, J. A.; Prsa, A.; Quintana, E. V.; Sanchis-Ojeda, R.; Sasselov, D.; Seader, S.; Shporer, A.; Steffen, J. H.; Still, M.; Tenenbaum, P.; Thompson, S. E.; Torres, G.; Twicken, J. D.; Welsh, W. F. and Winn, J. N. Kepler-62: A Five-Planet System with Planets of 1.4 and 1.6 Earth Radii in the Habitable Zone. *Science* **340**, 587 (2013).

Borucki, W. J.; Koch, D.; Basri, G.; Batalha, N.; Brown, T.; Caldwell, D.; Caldwell, J.; Christensen-Dalsgaard, J.; Cochran, W. D.; DeVore, E.; Dunham, E. W.; Dupree, A. K.;

Gautier, T. N.; Geary, J. C.; Gilliland, R.; Gould, A.; Howell, S. B.; Jenkins, J. M.; Kondo, Y.; Latham, D. W.; Marcy, G. W.; Meibom, S.; Kjeldsen, H.; Lissauer, J. J.; Monet, D. G.; Morrison, D.; Sasselov, D.; Tarter, J.; Boss, A.; Brownlee, D.; Owen, T.; Buzasi, D.; Charbonneau, D.; Doyle, L.; Fortney, J.; Ford, E. B.; Holman, M. J.; Seager, S.; Steffen, J. H.; Welsh, W. F.; Rowe, J.; Anderson, H.; Buchhave, L.; Ciardi, D.; Walkowicz, L.; Sherry, W.; Horch, E.; Isaacson, H.; Everett, M. E.; Fischer, D.; Torres, G.; Johnson, J. A.; Endl, M.; MacQueen, P.; Bryson, S. T.; Dotson, J.; Haas, M.; Kolodziejczak, J.; Van Cleve, J.; Chandrasekaran, H.; Twicken, J. D.; Quintana, E. V.; Clarke, B. D.; Allen, C.; Li, J.; Wu, H.; Tenenbaum, P.; Verner, E.; Bruhweiler, F.; Barnes, J. and Prsa, A. Kepler Planet-Detection Mission: Introduction and First Results. *Science* **327**, 977 (2010).

Borucki, W. J.; Koch, D. G.; Basri, G.; Batalha, N.; Brown, T. M.; Bryson, S. T.; Caldwell, D.; Christensen-Dalsgaard, J.; Cochran, W. D.; DeVore, E.; Dunham, E. W.; Gautier, III, T. N.; Geary, J. C.; Gilliland, R.; Gould, A.; Howell, S. B.; Jenkins, J. M.; Latham, D. W.; Lissauer, J. J.; Marcy, G. W.; Rowe, J.; Sasselov, D.; Boss, A.; Charbonneau, D.; Ciardi, D.; Doyle, L.; Dupree, A. K.; Ford, E. B.; Fortney, J.; Holman, M. J.; Seager, S.; Steffen, J. H.; Tarter, J.; Welsh, W. F.; Allen, C.; Buchhave, L. A.; Christiansen, J. L.; Clarke, B. D.; Das, S.; Désert, J.-M.; Endl, M.; Fabrycky, D.; Fressin, F.; Haas, M.; Horch, E.; Howard, A.; Isaacson, H.; Kjeldsen, H.; Kolodziejczak, J.; Kulesa, C.; Li, J.; Lucas, P. W.; Machalek, P.; McCarthy, D.; MacQueen, P.; Meibom, S.; Miquel, T.; Prsa, A.; Quinn, S. N.; Quintana, E. V.; Ragozzine, D.; Sherry, W.; Shporer, A.; Tenenbaum, P.; Torres, G.; Twicken, J. D.; Van Cleve, J.; Walkowicz, L.; Witteborn, F. C. and Still, M. Characteristics of Planetary

Candidates Observed by Kepler. II. Analysis of the First Four Months of Data. *ApJ* **736**, 19 (2011).

Boué, G.; Figueira, P.; Correia, A. C. M. and Santos, N. C. Orbital migration induced by anisotropic evaporation. Can hot Jupiters form hot Neptunes? *A&A* **537**, L3 (2012).

Calvet, N.; D'Alessio, P.; Hartmann, L.; Wilner, D.; Walsh, A. and Sitko, M. Evidence for a Developing Gap in a 10 Myr Old Protoplanetary Disk. *ApJ* **568**, 1008 (2002).

Calvet, N.; Hartmann, L. and Strom, S. E. Evolution of Disk Accretion. *Protostars and Planets IV* p. 377 (2000).

Carter, J. A.; Agol, E.; Chaplin, W. J.; Basu, S.; Bedding, T. R.; Buchhave, L. A.; Christensen-Dalsgaard, J.; Deck, K. M.; Elsworth, Y.; Fabrycky, D. C.; Ford, E. B.; Fortney, J. J.; Hale, S. J.; Handberg, R.; Hekker, S.; Holman, M. J.; Huber, D.; Karoff, C.; Kawaler, S. D.; Kjeldsen, H.; Lissauer, J. J.; Lopez, E. D.; Lund, M. N. L.; Lundkvist, M.; Metcalfe, T. S.; Miglio, A.; Rogers, L. A.; Stello, D.; Borucki, W. J.; Bryson, S.; Christiansen, J. L.; Cochran, W. D.; Geary, J. C.; Gilliland, R. L.; Haas, M. R.; Hall, J.; Howard, A. W.; Jenkins, J. M.; Klaus, T.; Koch, D. G.; Latham, D.; MacQueen, P. J.; Sasselov, D.; Steffen, J.; Twicken, J. D. and Winn, J. N. Kepler-36: A pair of planets with neighboring orbits and dissimilar densities. *Science* **337**, 556 (2012).

Cassan, A.; Kubas, D.; Beaulieu, J.-P.; Dominik, M.; Horne, K.; Greenhill, J.; Wambsganss, J.; Menzies, J.; Williams, A.; Jørgensen, U. G.; Udalski, A.; Bennett, D. P.; Albrow, M. D.; Batista, V.; Brillant, S.; Caldwell, J. A. R.; Cole, A.; Coutures, C.; Cook, K. H.; Dieters, S.;

Prester, D. D.; Donatowicz, J.; Fouqué, P.; Hill, K.; Kains, N.; Kane, S.; Marquette, J.-B.; Martin, R.; Pollard, K. R.; Sahu, K. C.; Vinter, C.; Warren, D.; Watson, B.; Zub, M.; Sumi, T.; Szymański, M. K.; Kubiak, M.; Poleski, R.; Soszynski, I.; Ulaczyk, K.; Pietrzyński, G. and Wyrzykowski, Ł. One or more bound planets per Milky Way star from microlensing observations. *Nature* **481**, 167 (2012).

Chambers, J. E. and Wetherill, G. W. Making the Terrestrial Planets: N-Body Integrations of Planetary Embryos in Three Dimensions. *Icarus* **136**, 304 (1998).

Charbonneau, D.; Berta, Z. K.; Irwin, J.; Burke, C. J.; Nutzman, P.; Buchhave, L. A.; Lovis, C.; Bonfils, X.; Latham, D. W.; Udry, S.; Murray-Clay, R. A.; Holman, M. J.; Falco, E. E.; Winn, J. N.; Queloz, D.; Pepe, F.; Mayor, M.; Delfosse, X. and Forveille, T. A super-Earth transiting a nearby low-mass star. *Nature* **462**, 891 (2009).

Charbonneau, D.; Brown, T. M.; Noyes, R. W. and Gilliland, R. L. Detection of an Extrasolar Planet Atmosphere. *ApJ* **568**, 377 (2002).

Chiang, E. and Laughlin, G. The minimum-mass extrasolar nebula: in situ formation of close-in super-Earths. *MNRAS* **431**, 3444 (2013).

Christiansen, J. L.; Clarke, B. D.; Burke, C. J.; Jenkins, J. M.; Barclay, T. S.; Ford, E. B.; Haas, M. R.; Sabale, A.; Seader, S.; Claiborne Smith, J.; Tenenbaum, P.; Twicken, J. D.; Kamal Uddin, A. and Thompson, S. E. Measuring Transit Signal Recovery in the Kepler Pipeline. I. Individual Events. *ApJS* **207**, 35 (2013).

Ciardi, D. R.; Fabrycky, D. C.; Ford, E. B.; Gautier, III, T. N.; Howell, S. B.; Lissauer, J. J.; Ragozzine, D. and Rowe, J. F. On the Relative Sizes of Planets within Kepler Multiple-candidate Systems. *ApJ* **763**, 41 (2013).

Cochran, W. D.; Fabrycky, D. C.; Torres, G.; Fressin, F.; Désert, J.-M.; Ragozzine, D.; Sasselov, D.; Fortney, J. J.; Rowe, J. F.; Brugamyer, E. J.; Bryson, S. T.; Carter, J. A.; Ciardi, D. R.; Howell, S. B.; Steffen, J. H.; Borucki, W. J.; Koch, D. G.; Winn, J. N.; Welsh, W. F.; Uddin, K.; Tenenbaum, P.; Still, M.; Seager, S.; Quinn, S. N.; Mullally, F.; Miller, N.; Marcy, G. W.; MacQueen, P. J.; Lucas, P.; Lissauer, J. J.; Latham, D. W.; Knutson, H.; Kinemuchi, K.; Johnson, J. A.; Jenkins, J. M.; Isaacson, H.; Howard, A.; Horch, E.; Holman, M. J.; Henze, C. E.; Haas, M. R.; Gilliland, R. L.; Gautier, III, T. N.; Ford, E. B.; Fischer, D. A.; Everett, M.; Endl, M.; Demory, B.-O.; Deming, D.; Charbonneau, D.; Caldwell, D.; Buchhave, L.; Brown, T. M. and Batalha, N. Kepler-18b, c, and d: A System of Three Planets Confirmed by Transit Timing Variations, Light Curve Validation, Warm-Spitzer Photometry, and Radial Velocity Measurements. *ApJS* **197**, 7 (2011).

Croll, B.; Albert, L.; Jayawardhana, R.; Miller-Ricci Kempton, E.; Fortney, J. J.; Murray, N. and Neilson, H. Broadband Transmission Spectroscopy of the Super-Earth GJ 1214b Suggests a Low Mean Molecular Weight Atmosphere. *ApJ* **736**, 78 (2011).

Davis, T. A. and Wheatley, P. J. Evidence for a lost population of close-in exoplanets. *MNRAS* **396**, 1012 (2009).

Deming, D.; Seager, S.; Richardson, L. J. and Harrington, J. Infrared radiation from an extra-solar planet. *Nature* **434**, 740 (2005).

Deming, D.; Seager, S.; Winn, J.; Miller-Ricci, E.; Clampin, M.; Lindler, D.; Greene, T.; Charbonneau, D.; Laughlin, G.; Ricker, G.; Latham, D. and Ennico, K. Discovery and Characterization of Transiting Super Earths Using an All-Sky Transit Survey and Follow-up by the James Webb Space Telescope. *PASP* **121**, 952 (2009).

Deming, D.; Wilkins, A.; McCullough, P.; Burrows, A.; Fortney, J. J.; Agol, E.; Dobbs-Dixon, I.; Madhusudhan, N.; Crouzet, N.; Desert, J.-M.; Gilliland, R. L.; Haynes, K.; Knutson, H. A.; Line, M.; Magic, Z.; Mandell, A. M.; Ranjan, S.; Charbonneau, D.; Clampin, M.; Seager, S. and Showman, A. P. Infrared Transmission Spectroscopy of the Exoplanets HD 209458b and XO-1b Using the Wide Field Camera-3 on the Hubble Space Telescope. *ApJ* **774**, 95 (2013).

Demory, B.-O.; Gillon, M.; Deming, D.; Valencia, D.; Seager, S.; Benneke, B.; Lovis, C.; Cubillos, P.; Harrington, J.; Stevenson, K. B.; Mayor, M.; Pepe, F.; Queloz, D.; Ségransan, D. and Udry, S. Detection of a transit of the super-Earth 55 Cancri e with warm Spitzer. *A&A* **533**, A114 (2011).

Désert, J.-M.; Bean, J.; Miller-Ricci Kempton, E.; Berta, Z. K.; Charbonneau, D.; Irwin, J.; Fortney, J.; Burke, C. J. and Nutzman, P. Observational Evidence for a Metal-rich Atmosphere on the Super-Earth GJ1214b. *ApJL* **731**, L40 (2011).

Doyle, L. R.; Carter, J. A.; Fabrycky, D. C.; Slawson, R. W.; Howell, S. B.; Winn, J. N.; Orosz, J. A.; Prsa, A.; Welsh, W. F.; Quinn, S. N.; Latham, D.; Torres, G.; Buchhave, L. A.; Marcy, G. W.; Fortney, J. J.; Shporer, A.; Ford, E. B.; Lissauer, J. J.; Ragozzine, D.; Rucker, M.; Batalha, N.; Jenkins, J. M.; Borucki, W. J.; Koch, D.; Middour, C. K.; Hall, J. R.; McCauliff,

S.; Fanelli, M. N.; Quintana, E. V.; Holman, M. J.; Caldwell, D. A.; Still, M.; Stefanik, R. P.; Brown, W. R.; Esquerdo, G. A.; Tang, S.; Furesz, G.; Geary, J. C.; Berlind, P.; Calkins, M. L.; Short, D. R.; Steffen, J. H.; Sasselov, D.; Dunham, E. W.; Cochran, W. D.; Boss, A.; Haas, M. R.; Buzasi, D. and Fischer, D. Kepler-16: A Transiting Circumbinary Planet. *Science* **333**, 1602 (2011).

Dragomir, D.; Matthews, J. M.; Eastman, J. D.; Cameron, C.; Howard, A. W.; Guenther, D. B.; Kuschnig, R.; Moffat, A. F. J.; Rowe, J. F.; Rucinski, S. M.; Sasselov, D. and Weiss, W. W. MOST Detects Transits of HD 97658b, a Warm, Likely Volatile-rich Super-Earth. *ApJL* **772**, L2 (2013a).

Dragomir, D.; Matthews, J. M.; Eastman, J. D.; Cameron, C.; Howard, A. W.; Guenther, D. B.; Kuschnig, R.; Moffat, A. F. J.; Rowe, J. F.; Rucinski, S. M.; Sasselov, D. and Weiss, W. W. MOST Detects Transits of HD 97658b, a Warm, Likely Volatile-rich Super-Earth. *ApJL* **772**, L2 (2013b).

Ehrenreich, D.; Bourrier, V.; Bonfils, X.; Lecavelier des Etangs, A.; Hébrard, G.; Sing, D. K.; Wheatley, P. J.; Vidal-Madjar, A.; Delfosse, X.; Udry, S.; Forveille, T. and Moutou, C. Hint of a transiting extended atmosphere on 55 Cancri b. *A&A* **547**, A18 (2012).

Ehrenreich, D. and Désert, J.-M. Mass-loss rates for transiting exoplanets. *A&A* **529**, A136 (2011).

Elkins-Tanton, L. T. and Seager, S. Ranges of Atmospheric Mass and Composition of Super-Earth Exoplanets. *ApJ* **685**, 1237 (2008).

Erkaev, N. V.; Kulikov, Y. N.; Lammer, H.; Selsis, F.; Langmayr, D.; Jaritz, G. F. and Biernat, H. K. Roche lobe effects on the atmospheric loss from "Hot Jupiters". *A&A* **472**, 329 (2007).

Fabrycky, D. C.; Ford, E. B.; Steffen, J. H.; Rowe, J. F.; Carter, J. A.; Moorhead, A. V.; Batalha, N. M.; Borucki, W. J.; Bryson, S.; Buchhave, L. A.; Christiansen, J. L.; Ciardi, D. R.; Cochran, W. D.; Endl, M.; Fanelli, M. N.; Fischer, D.; Fressin, F.; Geary, J.; Haas, M. R.; Hall, J. R.; Holman, M. J.; Jenkins, J. M.; Koch, D. G.; Latham, D. W.; Li, J.; Lissauer, J. J.; Lucas, P.; Marcy, G. W.; Mazeh, T.; McCauliff, S.; Quinn, S.; Ragozzine, D.; Sasselov, D. and Shporer, A. Transit Timing Observations from Kepler. IV. Confirmation of Four Multiple-planet Systems by Simple Physical Models. *ApJ* **750**, 114 (2012).

Fortney, J. J. The effect of condensates on the characterization of transiting planet atmospheres with transmission spectroscopy. *MNRAS* **364**, 649 (2005).

Fortney, J. J.; Ikoma, M.; Nettelmann, N.; Guillot, T. and Marley, M. S. Self-consistent Model Atmospheres and the Cooling of the Solar System's Giant Planets. *ApJ* **729**, 32 (2011a).

Fortney, J. J.; Ikoma, M.; Nettelmann, N.; Guillot, T. and Marley, M. S. Self-consistent Model Atmospheres and the Cooling of the Solar System's Giant Planets. *ApJ* **729**, 32 (2011b).

Fortney, J. J.; Marley, M. S. and Barnes, J. W. Planetary Radii across Five Orders of Magnitude in Mass and Stellar Insolation: Application to Transits. *ApJ* **659**, 1661 (2007).

Fortney, J. J.; Mordasini, C.; Nettelmann, N.; Kempton, E. M.-R.; Greene, T. P. and Zahnle, K. A Framework for Characterizing the Atmospheres of Low-mass Low-density Transiting Planets. *ApJ* **775**, 80 (2013).

French, M.; Mattsson, T. R.; Nettelmann, N. and Redmer, R. Equation of state and phase diagram of water at ultrahigh pressures as in planetary interiors. *Physical Review B* **79**, 054107 (2009).

Fressin, F.; Torres, G.; Charbonneau, D.; Bryson, S. T.; Christiansen, J.; Dressing, C. D.; Jenkins, J. M.; Walkowicz, L. M. and Batalha, N. M. The False Positive Rate of Kepler and the Occurrence of Planets. *ApJ* **766**, 81 (2013).

Fressin, F.; Torres, G.; Rowe, J. F.; Charbonneau, D.; Rogers, L. A.; Ballard, S.; Batalha, N. M.; Borucki, W. J.; Bryson, S. T.; Buchhave, L. A.; Ciardi, D. R.; Désert, J.-M.; Dressing, C. D.; Fabrycky, D. C.; Ford, E. B.; Gautier, III, T. N.; Henze, C. E.; Holman, M. J.; Howard, A.; Howell, S. B.; Jenkins, J. M.; Koch, D. G.; Latham, D. W.; Lissauer, J. J.; Marcy, G. W.; Quinn, S. N.; Ragozzine, D.; Sasselov, D. D.; Seager, S.; Barclay, T.; Mullally, F.; Seader, S. E.; Still, M.; Twicken, J. D.; Thompson, S. E. and Uddin, K. Two Earth-sized planets orbiting Kepler-20. *Nature* **482**, 195 (2012).

Gardner, J. P.; Mather, J. C.; Clampin, M.; Doyon, R.; Greenhouse, M. A.; Hammel, H. B.; Hutchings, J. B.; Jakobsen, P.; Lilly, S. J.; Long, K. S.; Lunine, J. I.; McCaughrean, M. J.; Mountain, M.; Nella, J.; Rieke, G. H.; Rieke, M. J.; Rix, H.-W.; Smith, E. P.; Sonneborn, G.; Stiavelli, M.; Stockman, H. S.; Windhorst, R. A. and Wright, G. S. The James Webb Space Telescope. *Space Science Reviews* **123**, 485 (2006).

Gautier, III, T. N.; Charbonneau, D.; Rowe, J. F.; Marcy, G. W.; Isaacson, H.; Torres, G.; Fressin, F.; Rogers, L. A.; Désert, J.-M.; Buchhave, L. A.; Latham, D. W.; Quinn, S. N.; Ciardi, D. R.; Fabrycky, D. C.; Ford, E. B.; Gilliland, R. L.; Walkowicz, L. M.; Bryson, S. T.;

Cochran, W. D.; Endl, M.; Fischer, D. A.; Howell, S. B.; Horch, E. P.; Barclay, T.; Batalha, N.; Borucki, W. J.; Christiansen, J. L.; Geary, J. C.; Henze, C. E.; Holman, M. J.; Ibrahim, K.; Jenkins, J. M.; Kinemuchi, K.; Koch, D. G.; Lissauer, J. J.; Sanderfer, D. T.; Sasselov, D. D.; Seager, S.; Silverio, K.; Smith, J. C.; Still, M.; Stumpe, M. C.; Tenenbaum, P. and Van Cleve, J. Kepler-20: A Sun-like Star with Three Sub-Neptune Exoplanets and Two Earth-size Candidates. *ApJ* **749**, 15 (2012).

Gilliland, R. L.; Marcy, G. W.; Rowe, J. F.; Rogers, L.; Torres, G.; Fressin, F.; Lopez, E. D.; Buchhave, L. A.; Christensen-Dalsgaard, J.; Désert, J.-M.; Henze, C. E.; Isaacson, H.; Jenkins, J. M.; Lissauer, J. J.; Chaplin, W. J.; Basu, S.; Metcalfe, T. S.; Elsworth, Y.; Handberg, R.; Hekker, S.; Huber, D.; Karoff, C.; Kjeldsen, H.; Lund, M. N.; Lundkvist, M.; Miglio, A.; Charbonneau, D.; Ford, E. B.; Fortney, J. J.; Haas, M. R.; Howard, A. W.; Howell, S. B.; Ragozzine, D. and Thompson, S. E. Kepler-68: Three Planets, One with a Density between that of Earth and Ice Giants. *ApJ* **766**, 40 (2013).

Gillon, M.; Demory, B.-O.; Benneke, B.; Valencia, D.; Deming, D.; Seager, S.; Lovis, C.; Mayor, M.; Pepe, F.; Queloz, D.; Ségransan, D. and Udry, S. Improved precision on the radius of the nearby super-Earth 55 Cnc e. *A&A* **539**, A28 (2012).

Gladman, B. Dynamics of systems of two close planets. *Icarus* **106**, 247 (1993).

Gorti, U.; Dullemond, C. P. and Hollenbach, D. Time Evolution of Viscous Circumstellar Disks due to Photoevaporation by Far-Ultraviolet, Extreme-Ultraviolet, and X-ray Radiation from the Central Star. *ApJ* **705**, 1237 (2009).

Guillot, T.; Chabrier, G.; Gautier, D. and Morel, P. Effect of Radiative Transport on the Evolution of Jupiter and Saturn. *ApJ* **450**, 463 (1995).

Hansen, B. M. S. and Murray, N. Migration then assembly: Formation of Neptune mass planets inside 1˜AU. *ArXiv e-prints* (2011).

Hansen, B. M. S. and Murray, N. Migration Then Assembly: Formation of Neptune-mass Planets inside 1 AU. *ApJ* **751**, 158 (2012).

Hansen, B. M. S. and Murray, N. Testing in Situ Assembly with the Kepler Planet Candidate Sample. *ApJ* **775**, 53 (2013).

Hansen, C. J.; Schwartz, J. C. and Cowan, N. B. Broadband Eclipse Spectra of Exoplanets are Featureless. *ArXiv e-prints* (2014).

Haswell, C. A.; Fossati, L.; Ayres, T.; France, K.; Froning, C. S.; Holmes, S.; Kolb, U. C.; Busuttil, R.; Street, R. A.; Hebb, L.; Collier Cameron, A.; Enoch, B.; Burwitz, V.; Rodriguez, J.; West, R. G.; Pollacco, D.; Wheatley, P. J. and Carter, A. Near-ultraviolet Absorption, Chromospheric Activity, and Star-Planet Interactions in the WASP-12 system. *ApJ* **760**, 79 (2012).

Hatzes, A. P.; Fridlund, M.; Nachmani, G.; Mazeh, T.; Valencia, D.; Hébrard, G.; Carone, L.; Pätzold, M.; Udry, S.; Bouchy, F.; Deleuil, M.; Moutou, C.; Barge, P.; Bordé, P.; Deeg, H.; Tingley, B.; Dvorak, R.; Gandolfi, D.; Ferraz-Mello, S.; Wuchterl, G.; Guenther, E.; Guillot, T.; Rauer, H.; Erikson, A.; Cabrera, J.; Csizmadia, S.; Léger, A.; Lammer, H.; Weingrill, J.;

Queloz, D.; Alonso, R.; Rouan, D. and Schneider, J. The Mass of CoRoT-7b. *ApJ* **743**, 75 (2011).

Hayashi, C.; Nakazawa, K. and Nakagawa, Y. Formation of the solar system. In Black, D. C. and Matthews, M. S., eds., *Protostars and Planets II* (1985), pp. 1100–1153.

Henning, W. G.; O'Connell, R. J. and Sasselov, D. D. Tidally Heated Terrestrial Exoplanets: Viscoelastic Response Models. *ApJ* **707**, 1000 (2009).

Holman, M. J.; Fabrycky, D. C.; Ragozzine, D.; Ford, E. B.; Steffen, J. H.; Welsh, W. F.; Lissauer, J. J.; Latham, D. W.; Marcy, G. W.; Walkowicz, L. M.; Batalha, N. M.; Jenkins, J. M.; Rowe, J. F.; Cochran, W. D.; Fressin, F.; Torres, G.; Buchhave, L. A.; Sasselov, D. D.; Borucki, W. J.; Koch, D. G.; Basri, G.; Brown, T. M.; Caldwell, D. A.; Charbonneau, D.; Dunham, E. W.; Gautier, T. N.; Geary, J. C.; Gilliland, R. L.; Haas, M. R.; Howell, S. B.; Ciardi, D. R.; Endl, M.; Fischer, D.; Fürész, G.; Hartman, J. D.; Isaacson, H.; Johnson, J. A.; MacQueen, P. J.; Moorhead, A. V.; Morehead, R. C. and Orosz, J. A. Kepler-9: A System of Multiple Planets Transiting a Sun-Like Star, Confirmed by Timing Variations. *Science* **330**, 51 (2010).

Holman, M. J. and Murray, N. W. The Use of Transit Timing to Detect Terrestrial-Mass Extrasolar Planets. *Science* **307**, 1288 (2005).

Howard, A. W.; Marcy, G. W.; Bryson, S. T.; Jenkins, J. M.; Rowe, J. F.; Batalha, N. M.; Borucki, W. J.; Koch, D. G.; Dunham, E. W.; Gautier, III, T. N.; Van Cleve, J.; Cochran, W. D.; Latham, D. W.; Lissauer, J. J.; Torres, G.; Brown, T. M.; Gilliland, R. L.; Buch-

have, L. A.; Caldwell, D. A.; Christensen-Dalsgaard, J.; Ciardi, D.; Fressin, F.; Haas, M. R.; Howell, S. B.; Kjeldsen, H.; Seager, S.; Rogers, L.; Sasselov, D. D.; Steffen, J. H.; Basri, G. S.; Charbonneau, D.; Christiansen, J.; Clarke, B.; Dupree, A.; Fabrycky, D. C.; Fischer, D. A.; Ford, E. B.; Fortney, J. J.; Tarter, J.; Girouard, F. R.; Holman, M. J.; Johnson, J. A.; Klaus, T. C.; Machalek, P.; Moorhead, A. V.; Morehead, R. C.; Ragozzine, D.; Tenenbaum, P.; Twicken, J. D.; Quinn, S. N.; Isaacson, H.; Shporer, A.; Lucas, P. W.; Walkowicz, L. M.; Welsh, W. F.; Boss, A.; Devore, E.; Gould, A.; Smith, J. C.; Morris, R. L.; Prsa, A.; Morton, T. D.; Still, M.; Thompson, S. E.; Mullally, F.; Endl, M. and MacQueen, P. J. Planet Occurrence within 0.25 AU of Solar-type Stars from Kepler. *ApJS* **201**, 15 (2012).

Howard, A. W.; Sanchis-Ojeda, R.; Marcy, G. W.; Johnson, J. A.; Winn, J. N.; Isaacson, H.; Fischer, D. A.; Fulton, B. J.; Sinukoff, E. and Fortney, J. J. A rocky composition for an Earth-sized exoplanet. *Nature* **503**, 381 (2013).

Howe, A. R. and Burrows, A. S. Theoretical Transit Spectra for GJ 1214b and Other "Super-Earths". *ApJ* **756**, 176 (2012).

Howell, S. B.; Sobeck, C.; Haas, M.; Still, M.; Barclay, T.; Mullally, F.; Troeltzsch, J.; Aigrain, S.; Bryson, S. T.; Caldwell, D.; Chaplin, W. J.; Cochran, W. D.; Huber, D.; Marcy, G. W.; Miglio, A.; Najita, J. R.; Smith, M.; Twicken, J. D. and Fortney, J. J. The K2 Mission: Characterization and Early results. *ArXiv e-prints* (2014).

Hubbard, W. B.; Fortney, J. J.; Lunine, J. I.; Burrows, A.; Sudarsky, D. and Pinto, P. Theory of Extrasolar Giant Planet Transits. *ApJ* **560**, 413 (2001).

Hubbard, W. B.; Hattori, M. F.; Burrows, A. and Hubeny, I. A Mass Function Constraint on Extrasolar Giant Planet Evaporation Rates. *ApJ* **658**, L59 (2007a).

Hubbard, W. B.; Hattori, M. F.; Burrows, A.; Hubeny, I. and Sudarsky, D. Effects of mass loss for highly-irradiated giant planets. *Icarus* **187**, 358 (2007b).

Hubbard, W. B.; Nellis, W. J.; Mitchell, A. C.; Holmes, N. C.; McCandless, P. C. and Limaye, S. S. Interior structure of Neptune - Comparison with Uranus. *Science* **253**, 648 (1991).

Huber, D.; Chaplin, W. J.; Christensen-Dalsgaard, J.; Gilliland, R. L.; Kjeldsen, H.; Buchhave, L. A.; Fischer, D. A.; Lissauer, J. J.; Rowe, J. F.; Sanchis-Ojeda, R.; Basu, S.; Handberg, R.; Hekker, S.; Howard, A. W.; Isaacson, H.; Karoff, C.; Latham, D. W.; Lund, M. N.; Lundkvist, M.; Marcy, G. W.; Miglio, A.; Silva Aguirre, V.; Stello, D.; Arentoft, T.; Barclay, T.; Bedding, T. R.; Burke, C. J.; Christiansen, J. L.; Elsworth, Y. P.; Haas, M. R.; Kawaler, S. D.; Metcalfe, T. S.; Mullally, F. and Thompson, S. E. Fundamental Properties of Kepler Planet-candidate Host Stars using Asteroseismology. *ApJ* **767**, 127 (2013).

Huber, D.; Silva Aguirre, V.; Matthews, J. M.; Pinsonneault, M. H.; Gaidos, E.; García, R. A.; Hekker, S.; Mathur, S.; Mosser, B.; Torres, G.; Bastien, F. A.; Basu, S.; Bedding, T. R.; Chaplin, W. J.; Demory, B.-O.; Fleming, S. W.; Guo, Z.; Mann, A. W.; Rowe, J. F.; Serenelli, A. M.; Smith, M. A. and Stello, D. Revised Stellar Properties of Kepler Targets for the Quarter 1-16 Transit Detection Run. *ApJS* **211**, 2 (2014).

Hunten, D. M. Thermal and nonthermal escape mechanisms for terrestrial bodies. *Planetary and Space Science* **30**, 773 (1982).

Ida, S. and Lin, D. N. C. Toward a Deterministic Model of Planetary Formation. I. A Desert in the Mass and Semimajor Axis Distributions of Extrasolar Planets. *ApJ* **604**, 388 (2004).

Ida, S. and Lin, D. N. C. Toward a Deterministic Model of Planetary Formation. VI. Dynamical Interaction and Coagulation of Multiple Rocky Embryos and Super-Earth Systems around Solar-type Stars. *ApJ* **719**, 810 (2010).

Ikoma, M. and Hori, Y. In Situ Accretion of Hydrogen-rich Atmospheres on Short-period Super-Earths: Implications for the Kepler-11 Planets. *ApJ* **753**, 66 (2012).

Jackson, A. P.; Davis, T. A. and Wheatley, P. J. The coronal X-ray-age relation and its implications for the evaporation of exoplanets. *MNRAS* **422**, 2024 (2012).

Jackson, B.; Miller, N.; Barnes, R.; Raymond, S. N.; Fortney, J. J. and Greenberg, R. The roles of tidal evolution and evaporative mass loss in the origin of CoRoT-7 b. *MNRAS* **407**, 910 (2010).

Jontof-Hutter, D.; Lissauer, J. J.; Rowe, J. F. and Fabrycky, D. C. KOI-152's Low Density Planets. *ArXiv e-prints* (2013).

Kasting, J. F. and Pollack, J. B. Loss of water from Venus. I - Hydrodynamic escape of hydrogen. *Icarus* **53**, 479 (1983).

Knudson, M. D.; Desjarlais, M. P.; Lemke, R. W.; Mattsson, T. R.; French, M.; Nettelmann, N. and Redmer, R. Probing the Interiors of the Ice Giants: Shock Compression of Water to 700 GPa and 3.8g/cm^3. *Physical Review Letters* **108**, 091102 (2012).

Knutson, H. A.; Benneke, B.; Deming, D. and Homeier, D. A featureless transmission spectrum for the Neptune-mass exoplanet GJ436b. *Nature* **505**, 66 (2014a).

Knutson, H. A.; Charbonneau, D.; Allen, L. E.; Burrows, A. and Megeath, S. T. The 3.6-8.0 μm Broadband Emission Spectrum of HD 209458b: Evidence for an Atmospheric Temperature Inversion. *ApJ* **673**, 526 (2008).

Knutson, H. A.; Dragomir, D.; Kreidberg, L.; Kempton, E. M.-R.; McCullough, P. R.; Fortney, J. J.; Bean, J. L.; Gillon, M.; Homeier, D. and Howard, A. W. Hubble Space Telescope Near-IR Transmission Spectroscopy of the Super-Earth HD 97658b. *ArXiv e-prints* (2014b).

Kreidberg, L.; Bean, J. L.; Désert, J.-M.; Benneke, B.; Deming, D.; Stevenson, K. B.; Seager, S.; Berta-Thompson, Z.; Seifahrt, A. and Homeier, D. Clouds in the atmosphere of the super-Earth exoplanet GJ1214b. *Nature* **505**, 69 (2014).

Lammer, H.; Selsis, F.; Ribas, I.; Guinan, E. F.; Bauer, S. J. and Weiss, W. W. Atmospheric Loss of Exoplanets Resulting from Stellar X-Ray and Extreme-Ultraviolet Heating. *ApJL* **598**, L121 (2003).

Lecavelier Des Etangs, A. A diagram to determine the evaporation status of extrasolar planets. *A&A* **461**, 1185 (2007).

Lecavelier des Etangs, A.; Bourrier, V.; Wheatley, P. J.; Dupuy, H.; Ehrenreich, D.; Vidal-Madjar, A.; Hébrard, G.; Ballester, G. E.; Désert, J.-M.; Ferlet, R. and Sing, D. K. Temporal variations in the evaporating atmosphere of the exoplanet HD 189733b. *A&A* **543**, L4 (2012).

Lecavelier Des Etangs, A.; Ehrenreich, D.; Vidal-Madjar, A.; Ballester, G. E.; Désert, J.-M.; Ferlet, R.; Hébrard, G.; Sing, D. K.; Tchakoumegni, K.-O. and Udry, S. Evaporation of the planet HD 189733b observed in H I Lyman-α. *A&A* **514**, A72 (2010).

Lecavelier des Etangs, A.; Vidal-Madjar, A.; McConnell, J. C. and Hébrard, G. Atmospheric escape from hot Jupiters. *A&A* **418**, L1 (2004).

Léger, A.; Rouan, D.; Schneider, J.; Barge, P.; Fridlund, M.; Samuel, B.; Ollivier, M.; Guenther, E.; Deleuil, M.; Deeg, H. J.; Auvergne, M.; Alonso, R.; Aigrain, S.; Alapini, A.; Almenara, J. M.; Baglin, A.; Barbieri, M.; Bruntt, H.; Bordé, P.; Bouchy, F.; Cabrera, J.; Catala, C.; Carone, L.; Carpano, S.; Csizmadia, S.; Dvorak, R.; Erikson, A.; Ferraz-Mello, S.; Foing, B.; Fressin, F.; Gandolfi, D.; Gillon, M.; Gondoin, P.; Grasset, O.; Guillot, T.; Hatzes, A.; Hébrard, G.; Jorda, L.; Lammer, H.; Llebaria, A.; Loeillet, B.; Mayor, M.; Mazeh, T.; Moutou, C.; Pätzold, M.; Pont, F.; Queloz, D.; Rauer, H.; Renner, S.; Samadi, R.; Shporer, A.; Sotin, C.; Tingley, B.; Wuchterl, G.; Adda, M.; Agogu, P.; Appourchaux, T.; Ballans, H.; Baron, P.; Beaufort, T.; Bellenger, R.; Berlin, R.; Bernardi, P.; Blouin, D.; Baudin, F.; Bodin, P.; Boisnard, L.; Boit, L.; Bonneau, F.; Borzeix, S.; Briet, R.; Buey, J.-T.; Butler, B.; Cailleau, D.; Cautain, R.; Chabaud, P.-Y.; Chaintreuil, S.; Chiavassa, F.; Costes, V.; Cuna Parrho, V.; de Oliveira Fialho, F.; Decaudin, M.; Defise, J.-M.; Djalal, S.; Epstein, G.; Exil, G.-E.; Fauré, C.; Fenouillet, T.; Gaboriaud, A.; Gallic, A.; Gamet, P.; Gavalda, P.; Grolleau, E.; Gruneisen, R.; Gueguen, L.; Guis, V.; Guivarc'h, V.; Guterman, P.; Hallouard, D.; Hasiba, J.; Heuripeau, F.; Huntzinger, G.; Hustaix, H.; Imad, C.; Imbert, C.; Johlander, B.; Jouret, M.; Journoud, P.; Karioty, F.; Kerjean, L.; Lafaille, V.; Lafond, L.; Lam-Trong, T.; Landiech, P.; Lapeyrere,

V.; Larqué, T.; Laudet, P.; Lautier, N.; Lecann, H.; Lefevre, L.; Leruyet, B.; Levacher, P.; Magnan, A.; Mazy, E.; Mertens, F.; Mesnager, J.-M.; Meunier, J.-C.; Michel, J.-P.; Monjoin, W.; Naudet, D.; Nguyen-Kim, K.; Orcesi, J.-L.; Ottacher, H.; Perez, R.; Peter, G.; Plasson, P.; Plesseria, J.-Y.; Pontet, B.; Pradines, A.; Quentin, C.; Reynaud, J.-L.; Rolland, G.; Rollenhagen, F.; Romagnan, R.; Russ, N.; Schmidt, R.; Schwartz, N.; Sebbag, I.; Sedes, G.; Smit, H.; Steller, M. B.; Sunter, W.; Surace, C.; Tello, M.; Tiphène, D.; Toulouse, P.; Ulmer, B.; Vandermarcq, O.; Vergnault, E.; Vuillemin, A. and Zanatta, P. Transiting exoplanets from the CoRoT space mission. VIII. CoRoT-7b: the first super-Earth with measured radius. *A&A* **506**, 287 (2009).

Lin, D. N. C.; Bodenheimer, P. and Richardson, D. C. Orbital migration of the planetary companion of 51 Pegasi to its present location. *Nature* **380**, 606 (1996).

Lin, D. N. C. and Ida, S. On the Origin of Massive Eccentric Planets. *ApJ* **477**, 781 (1997).

Line, M. R.; Knutson, H.; Wolf, A. S. and Yung, Y. L. A Systematic Retrieval Analysis of Secondary Eclipse Spectra. II. A Uniform Analysis of Nine Planets and their C to O Ratios. *ApJ* **783**, 70 (2014).

Line, M. R.; Zhang, X.; Vasisht, G.; Natraj, V.; Chen, P. and Yung, Y. L. Information Content of Exoplanetary Transit Spectra: An Initial Look. *ApJ* **749**, 93 (2012).

Linsky, J. L.; Yang, H.; France, K.; Froning, C. S.; Green, J. C.; Stocke, J. T. and Osterman, S. N. Observations of Mass Loss from the Transiting Exoplanet HD 209458b. *ApJ* **717**, 1291 (2010).

Lissauer, J. J.; Fabrycky, D. C.; Ford, E. B.; Borucki, W. J.; Fressin, F.; Marcy, G. W.; Orosz, J. A.; Rowe, J. F.; Torres, G.; Welsh, W. F.; Batalha, N. M.; Bryson, S. T.; Buchhave, L. A.; Caldwell, D. A.; Carter, J. A.; Charbonneau, D.; Christiansen, J. L.; Cochran, W. D.; Desert, J.-M.; Dunham, E. W.; Fanelli, M. N.; Fortney, J. J.; Gautier, III, T. N.; Geary, J. C.; Gilliland, R. L.; Haas, M. R.; Hall, J. R.; Holman, M. J.; Koch, D. G.; Latham, D. W.; Lopez, E.; McCauliff, S.; Miller, N.; Morehead, R. C.; Quintana, E. V.; Ragozzine, D.; Sasselov, D.; Short, D. R. and Steffen, J. H. A closely packed system of low-mass, low-density planets transiting Kepler-11. *Nature* **470**, 53 (2011a).

Lissauer, J. J.; Jontof-Hutter, D.; Rowe, J. F.; Fabrycky, D. C.; Lopez, E. D.; Agol, E.; Marcy, G. W.; Deck, K. M.; Fischer, D. A.; Fortney, J. J.; Howell, S. B.; Isaacson, H.; Jenkins, J. M.; Kolbl, R.; Sasselov, D.; Short, D. R. and Welsh, W. F. All Six Planets Known to Orbit Kepler-11 Have Low Densities. *ApJ* **770**, 131 (2013).

Lissauer, J. J.; Ragozzine, D.; Fabrycky, D. C.; Steffen, J. H.; Ford, E. B.; Jenkins, J. M.; Shporer, A.; Holman, M. J.; Rowe, J. F.; Quintana, E. V.; Batalha, N. M.; Borucki, W. J.; Bryson, S. T.; Caldwell, D. A.; Carter, J. A.; Ciardi, D.; Dunham, E. W.; Fortney, J. J.; Gautier, III, T. N.; Howell, S. B.; Koch, D. G.; Latham, D. W.; Marcy, G. W.; Morehead, R. C. and Sasselov, D. Architecture and Dynamics of Kepler's Candidate Multiple Transiting Planet Systems. *ApJS* **197**, 8 (2011b).

Lopez, E. D. and Fortney, J. J. The Role of Core Mass in Controlling Evaporation: The Kepler Radius Distribution and the Kepler-36 Density Dichotomy. *ApJ* **776**, 2 (2013a).

Lopez, E. D. and Fortney, J. J. Understanding the Mass-Radius Relation for Sub-Neptunes: Radius as a Proxy for Composition. *ArXiv e-prints* (2013b).

Lopez, E. D.; Fortney, J. J. and Miller, N. How Thermal Evolution and Mass-loss Sculpt Populations of Super-Earths and Sub-Neptunes: Application to the Kepler-11 System and Beyond. *ApJ* **761**, 59 (2012).

Lyon, S. P. and Johnson, J. D. LANL Rep. LA-UR-92-3407 (Los Alamos: LANL). *LANL Rep. LA-UR-92-3407 (Los Alamos: LANL)* (1992).

Marcus, R. A.; Sasselov, D.; Hernquist, L. and Stewart, S. T. Minimum Radii of Super-Earths: Constraints from Giant Impacts. *ApJL* **712**, L73 (2010).

Marcus, R. A.; Stewart, S. T.; Sasselov, D. and Hernquist, L. Collisional Stripping and Disruption of Super-Earths. *ApJL* **700**, L118 (2009).

Marcy, G. W.; Isaacson, H.; Howard, A. W.; Rowe, J. F.; Jenkins, J. M.; Bryson, S. T.; Latham, D. W.; Howell, S. B.; Gautier, III, T. N.; Batalha, N. M.; Rogers, L.; Ciardi, D.; Fischer, D. A.; Gilliland, R. L.; Kjeldsen, H.; Christensen-Dalsgaard, J.; Huber, D.; Chaplin, W. J.; Basu, S.; Buchhave, L. A.; Quinn, S. N.; Borucki, W. J.; Koch, D. G.; Hunter, R.; Caldwell, D. A.; Van Cleve, J.; Kolbl, R.; Weiss, L. M.; Petigura, E.; Seager, S.; Morton, T.; Johnson, J. A.; Ballard, S.; Burke, C.; Cochran, W. D.; Endl, M.; MacQueen, P.; Everett, M. E.; Lissauer, J. J.; Ford, E. B.; Torres, G.; Fressin, F.; Brown, T. M.; Steffen, J. H.; Charbonneau, D.; Basri, G. S.; Sasselov, D. D.; Winn, J.; Sanchis-Ojeda, R.; Christiansen, J.; Adams, E.; Henze, C.; Dupree, A.; Fabrycky, D. C.; Fortney, J. J.; Tarter, J.; Holman, M. J.; Tenenbaum,

P.; Shporer, A.; Lucas, P. W.; Welsh, W. F.; Orosz, J. A.; Bedding, T. R.; Campante, T. L.; Davies, G. R.; Elsworth, Y.; Handberg, R.; Hekker, S.; Karoff, C.; Kawaler, S. D.; Lund, M. N.; Lundkvist, M.; Metcalfe, T. S.; Miglio, A.; Silva Aguirre, V.; Stello, D.; White, T. R.; Boss, A.; Devore, E.; Gould, A.; Prsa, A.; Agol, E.; Barclay, T.; Coughlin, J.; Brugamyer, E.; Mullally, F.; Quintana, E. V.; Still, M.; Thompson, S. E.; Morrison, D.; Twicken, J. D.; Désert, J.-M.; Carter, J.; Crepp, J. R.; Hébrard, G.; Santerne, A.; Moutou, C.; Sobeck, C.; Hudgins, D.; Haas, M. R.; Robertson, P.; Lillo-Box, J. and Barrado, D. Masses, Radii, and Orbits of Small Kepler Planets: The Transition from Gaseous to Rocky Planets. *ApJS* **210**, 20 (2014a).

Marcy, G. W.; Weiss, L. M.; Petigura, E. A.; Isaacson, H.; Howard, A. W. and Buchhave, L. A. Occurrence and core-envelope structure of 1–4x Earth-size planets around Sun-like stars. *ArXiv e-prints* (2014b).

Marley, M. S.; Fortney, J. J.; Hubickyj, O.; Bodenheimer, P. and Lissauer, J. J. On the Luminosity of Young Jupiters. *ApJ* **655**, 541 (2007).

Masuda, K. Very Low Density Planets around Kepler-51 Revealed with Transit Timing Variations and an Anomaly Similar to a Planet-Planet Eclipse Event. *ApJ* **783**, 53 (2014).

Miller, N. and Fortney, J. J. The Heavy-element Masses of Extrasolar Giant Planets, Revealed. *ApJL* **736**, L29 (2011).

Miller-Ricci, E. and Fortney, J. J. The Nature of the Atmosphere of the Transiting Super-Earth GJ 1214b. *ApJL* **716**, L74 (2010).

Miller-Ricci, E.; Seager, S. and Sasselov, D. The Atmospheric Signatures of Super-Earths: How to Distinguish Between Hydrogen-Rich and Hydrogen-Poor Atmospheres. *ApJ* **690**, 1056 (2009).

Miller-Ricci Kempton, E.; Zahnle, K. and Fortney, J. J. The Atmospheric Chemistry of GJ 1214b: Photochemistry and Clouds. *ApJ* **745**, 3 (2012a).

Miller-Ricci Kempton, E.; Zahnle, K. and Fortney, J. J. The Atmospheric Chemistry of GJ 1214b: Photochemistry and Clouds. *ApJ* **745**, 3 (2012b).

Morbidelli, A.; Lunine, J. I.; O'Brien, D. P.; Raymond, S. N. and Walsh, K. J. Building Terrestrial Planets. *Annual Review of Earth and Planetary Sciences* **40**, 251 (2012).

Mordasini, C. Luminosity of young Jupiters revisited. Massive cores make hot planets. *A&A* **558**, A113 (2013).

Mordasini, C.; Alibert, Y. and Benz, W. Extrasolar planet population synthesis. I. Method, formation tracks, and mass-distance distribution. *A&A* **501**, 1139 (2009).

Mordasini, C.; Alibert, Y.; Benz, W. and Klahr, H. Theory of planet formation and comparison with observation: Formation of the planetary mass-radius relationship. *ArXiv e-prints* (2011).

Mordasini, C.; Alibert, Y.; Georgy, C.; Dittkrist, K.-M.; Klahr, H. and Henning, T. Characterization of exoplanets from their formation. II. The planetary mass-radius relationship. *A&A* **547**, A112 (2012).

Morley, C. V.; Fortney, J. J.; Kempton, E. M.-R.; Marley, M. S.; Vissher, C. and Zahnle, K. Quantitatively Assessing the Role of Clouds in the Transmission Spectrum of GJ 1214b. *ApJ* **775**, 33 (2013).

Morley, C. V.; Fortney, J. J.; Marley, M. S.; Visscher, C.; Saumon, D. and Leggett, S. K. Neglected Clouds in T and Y Dwarf Atmospheres. *ApJ* **756**, 172 (2012).

Morton, T. D. and Swift, J. J. The Radius Distribution of Small Planets Around Cool Stars. *ArXiv e-prints* (2013).

Movshovitz, N.; Bodenheimer, P.; Podolak, M. and Lissauer, J. J. Formation of Jupiter using opacities based on detailed grain physics. *Icarus* **209**, 616 (2010).

Muirhead, P. S.; Hamren, K.; Schlawin, E.; Rojas-Ayala, B.; Covey, K. R. and Lloyd, J. P. Characterizing the Cool Kepler Objects of Interests. New Effective Temperatures, Metallicities, Masses, and Radii of Low-mass Kepler Planet-candidate Host Stars. *ApJL* **750**, L37 (2012).

Murray-Clay, R. A.; Chiang, E. I. and Murray, N. Atmospheric Escape From Hot Jupiters. *ApJ* **693**, 23 (2009).

Nettelmann, N.; Fortney, J. J.; Kramm, U. and Redmer, R. Thermal Evolution and Structure Models of the Transiting Super-Earth GJ 1214b. *ApJ* **733**, 2 (2011).

Nettelmann, N.; Holst, B.; Kietzmann, A.; French, M.; Redmer, R. and Blaschke, D. Ab Initio Equation of State Data for Hydrogen, Helium, and Water and the Internal Structure of Jupiter. *ApJ* **683**, 1217 (2008).

Owen, J. E. and Jackson, A. P. Planetary evaporation by UV & X-ray radiation: basic hydrodynamics. *MNRAS* **425**, 2931 (2012).

Owen, J. E. and Wu, Y. Kepler Planets: A Tale of Evaporation. *ApJ* **775**, 105 (2013).

Pepe, F.; Cameron, A. C.; Latham, D. W.; Molinari, E.; Udry, S.; Bonomo, A. S.; Buchhave, L. A.; Charbonneau, D.; Cosentino, R.; Dressing, C. D.; Dumusque, X.; Figueira, P.; Fiorenzano, A. F. M.; Gettel, S.; Harutyunyan, A.; Haywood, R. D.; Horne, K.; Lopez-Morales, M.; Lovis, C.; Malavolta, L.; Mayor, M.; Micela, G.; Motalebi, F.; Nascimbeni, V.; Phillips, D.; Piotto, G.; Pollacco, D.; Queloz, D.; Rice, K.; Sasselov, D.; Ségransan, D.; Sozzetti, A.; Szentgyorgyi, A. and Watson, C. A. An Earth-sized planet with an Earth-like density. *Nature* **503**, 377 (2013).

Petigura, E. A.; Howard, A. W. and Marcy, G. W. Prevalence of Earth-size planets orbiting Sun-like stars. *Proceedings of the National Academy of Science* **110**, 19273 (2013a).

Petigura, E. A.; Marcy, G. W. and Howard, A. W. A Plateau in the Planet Population below Twice the Size of Earth. *ApJ* **770**, 69 (2013b).

Pollack, J. B.; Hubickyj, O.; Bodenheimer, P.; Lissauer, J. J.; Podolak, M. and Greenzweig, Y. Formation of the Giant Planets by Concurrent Accretion of Solids and Gas. *Icarus* **124**, 62 (1996).

Posselt, W.; Holota, W.; Kulinyak, E.; Kling, G.; Kutscheid, T.; Le Fevre, O.; Prieto, E. and Ferruit, P. NIRSpec: near-infrared spectrograph for the JWST. In Mather, J. C., ed., *Optical*,

Infrared, and Millimeter Space Telescopes (2004), vol. 5487 of *Society of Photo-Optical Instrumentation Engineers (SPIE) Conference Series*, pp. 688–697.

Queloz, D.; Bouchy, F.; Moutou, C.; Hatzes, A.; Hébrard, G.; Alonso, R.; Auvergne, M.; Baglin, A.; Barbieri, M.; Barge, P.; Benz, W.; Bordé, P.; Deeg, H. J.; Deleuil, M.; Dvorak, R.; Erikson, A.; Ferraz Mello, S.; Fridlund, M.; Gandolfi, D.; Gillon, M.; Guenther, E.; Guillot, T.; Jorda, L.; Hartmann, M.; Lammer, H.; Léger, A.; Llebaria, A.; Lovis, C.; Magain, P.; Mayor, M.; Mazeh, T.; Ollivier, M.; Pätzold, M.; Pepe, F.; Rauer, H.; Rouan, D.; Schneider, J.; Segransan, D.; Udry, S. and Wuchterl, G. The CoRoT-7 planetary system: two orbiting super-Earths. *A&A* **506**, 303 (2009).

Ranjan, S.; Charbonneau, D.; Désert, J.-M.; Madhusudhan, N.; Deming, D.; Wilkins, A. and Mandell, A. M. Atmospheric Characterization of Five Hot Jupiters with the Wide Field Camera 3 on the Hubble Space Telescope. *ApJ* **785**, 148 (2014).

Rasio, F. A. and Ford, E. B. Dynamical instabilities and the formation of extrasolar planetary systems. *Science* **274**, 954 (1996).

Rauer, H.; Catala, C.; Aerts, C.; Appourchaux, T.; Benz, W.; Brandeker, A.; Christensen-Dalsgaard, J.; Deleuil, M.; Gizon, L.; Goupil, M.-J.; Güdel, M.; Janot-Pacheco, E.; Mas-Hesse, M.; Pagano, I.; Piotto, G.; Pollacco, D.; Santos, N. C.; Smith, A.; -C., J.; Suárez; Sz-abó, R.; Udry, S.; Adibekyan, V.; Alibert, Y.; Almenara, J.-M.; Amaro-Seoane, P.; Ammler-von Eiff, M.; Asplund, M.; Antonello, E.; Ball, W.; Barnes, S.; Baudin, F.; Belkacem, K.; Bergemann, M.; Bihain, G.; Birch, A. C.; Bonfils, X.; Boisse, I.; Bonomo, A. S.; Borsa, F.; Brandão, I. M.; Brocato, E.; Brun, S.; Burleigh, M.; Burston, R.; Cabrera, J.; Cassisi,

S.; Chaplin, W.; Charpinet, S.; Chiappini, C.; Church, R. P.; Csizmadia, S.; Cunha, M.; Damasso, M.; Davies, M. B.; Deeg, H. J.; D´az, R. F.; Dreizler, S.; Dreyer, C.; Eggenberger, P.; Ehrenreich, D.; Eigmüller, P.; Erikson, A.; Farmer, R.; Feltzing, S.; de Oliveira Fialho, F.; Figueira, P.; Forveille, T.; Fridlund, M.; García, R. A.; Giommi, P.; Giuffrida, G.; Godolt, M.; Gomes da Silva, J.; Granzer, T.; Grenfell, J. L.; Grotsch-Noels, A.; Günther, E.; Haswell, C. A.; Hatzes, A. P.; Hébrard, G.; Hekker, S.; Helled, R.; Heng, K.; Jenkins, J. M.; Johansen, A.; Khodachenko, M. L.; Kislyakova, K. G.; Kley, W.; Kolb, U.; Krivova, N.; Kupka, F.; Lammer, H.; Lanza, A. F.; Lebreton, Y.; Magrin, D.; Marcos-Arenal, P.; Marrese, P. M.; Marques, J. P.; Martins, J.; Mathis, S.; Mathur, S.; Messina, S.; Miglio, A.; Montalban, J.; Montalto, M.; Monteiro, M. J. P. F. G.; Moradi, H.; Moravveji, E.; Mordasini, C.; Morel, T.; Mortier, A.; Nascimbeni, V.; Nelson, R. P.; Nielsen, M. B.; Noack, L.; Norton, A. J.; Ofir, A.; Oshagh, M.; Ouazzani, R.-M.; Pápics, P.; Parro, V. C.; Petit, P.; Plez, B.; Poretti, E.; Quirrenbach, A.; Ragazzoni, R.; Raimondo, G.; Rainer, M.; Reese, D. R.; Redmer, R.; Reffert, S.; Rojas-Ayala, B.; Roxburgh, I. W.; Salmon, S.; Santerne, A.; Schneider, J.; Schou, J.; Schuh, S.; Schunker, H.; Silva-Valio, A.; Silvotti, R.; Skillen, I.; Snellen, I.; Sohl, F.; Sousa, S. G.; Sozzetti, A.; Stello, D.; Strassmeier, K. G.; Švanda, M.; Szabó, G. M.; Tkachenko, A.; Valencia, D.; van Grootel, V.; Vauclair, S. D.; Ventura, P.; Wagner, F. W.; Walton, N. A.; Weingrill, J.; Werner, S. C.; Wheatley, P. J. and Zwintz, K. The PLATO 2.0 Mission. *ArXiv e-prints* (2013).

Ribas, I.; Guinan, E. F.; Güdel, M. and Audard, M. Evolution of the Solar Activity over Time and Effects on Planetary Atmospheres. I. High-Energy Irradiances (1-1700 A). *ApJ* **622**, 680

(2005).

Ricker, G. R.; Latham, D. W.; Vanderspek, R. K.; Ennico, K. A.; Bakos, G.; Brown, T. M.; Burgasser, A. J.; Charbonneau, D.; Clampin, M.; Deming, L. D.; Doty, J. P.; Dunham, E. W.; Elliot, J. L.; Holman, M. J.; Ida, S.; Jenkins, J. M.; Jernigan, J. G.; Kawai, N.; Laughlin, G. P.; Lissauer, J. J.; Martel, F.; Sasselov, D. D.; Schingler, R. H.; Seager, S.; Torres, G.; Udry, S.; Villasenor, J. N.; Winn, J. N. and Worden, S. P. Transiting Exoplanet Survey Satellite (TESS). In *American Astronomical Society Meeting Abstracts #215* (2010), vol. 42 of *Bulletin of the American Astronomical Society*, p. 450.06.

Rogers, L. A.; Bodenheimer, P.; Lissauer, J. J. and Seager, S. Formation and Structure of Low-density exo-Neptunes. *ApJ* **738**, 59 (2011).

Rogers, L. A. and Seager, S. A Framework for Quantifying the Degeneracies of Exoplanet Interior Compositions. *ApJ* **712**, 974 (2010a).

Rogers, L. A. and Seager, S. Three Possible Origins for the Gas Layer on GJ 1214b. *ApJ* **716**, 1208 (2010b).

Sanchis-Ojeda, R.; Fabrycky, D. C.; Winn, J. N.; Barclay, T.; Clarke, B. D.; Ford, E. B.; Fortney, J. J.; Geary, J. C.; Holman, M. J.; Howard, A. W.; Jenkins, J. M.; Koch, D.; Lissauer, J. J.; Marcy, G. W.; Mullally, F.; Ragozzine, D.; Seader, S. E.; Still, M. and Thompson, S. E. Alignment of the stellar spin with the orbits of a three-planet system. *Nature* **487**, 449 (2012).

Sanz-Forcada, J.; Micela, G.; Ribas, I.; Pollock, A. M. T.; Eiroa, C.; Velasco, A.; Solano, E. and García-Álvarez, D. Estimation of the XUV radiation onto close planets and their evaporation.

A&A **532**, A6 (2011).

Sanz-Forcada, J.; Ribas, I.; Micela, G.; Pollock, A. M. T.; García-Álvarez, D.; Solano, E. and Eiroa, C. A scenario of planet erosion by coronal radiation. *A&A* **511**, L8 (2010).

Saumon, D.; Chabrier, G. and van Horn, H. M. An Equation of State for Low-Mass Stars and Giant Planets. *ApJS* **99**, 713 (1995).

Sekiya, M.; Nakazawa, K. and Hayashi, C. Dissipation of the Primordial Terrestrial Atmosphere Due to Irradiation of the Solar EUV. *Progress of Theoretical Physics* **64**, 1968 (1980).

Smith, A. W. and Lissauer, J. J. Orbital stability of systems of closely-spaced planets. *Icarus* **201**, 381 (2009).

Stevenson, K. B.; Bean, J. L.; Seifahrt, A.; Desert, J.-M.; Madhusudhan, N.; Bergmann, M.; Kreidberg, L. and Homeier, D. Transmission Spectroscopy of the Hot-Jupiter WASP-12b from 0.7 to 5 microns. *ArXiv e-prints* (2013).

Swift, J. J.; Johnson, J. A.; Morton, T. D.; Crepp, J. R.; Montet, B. T.; Fabrycky, D. C. and Muirhead, P. S. Characterizing the Cool KOIs. IV. Kepler-32 as a Prototype for the Formation of Compact Planetary Systems throughout the Galaxy. *ApJ* **764**, 105 (2013).

Tanaka, H.; Takeuchi, T. and Ward, W. R. Three-Dimensional Interaction between a Planet and an Isothermal Gaseous Disk. I. Corotation and Lindblad Torques and Planet Migration. *ApJ* **565**, 1257 (2002).

Thompson, S. L. ANEOS—Analytic Equations of State for Shock Physics Codes, Sandia Natl. Lab. Doc. SAND89-2951. *ANEOS—Analytic Equations of State for Shock Physics Codes, Sandia Natl. Lab. Doc. SAND89-2951* (1990).

Valencia, D.; Guillot, T.; Parmentier, V. and Freedman, R. S. Bulk Composition of GJ 1214b and other sub-Neptune exoplanets. *ArXiv e-prints* (2013).

Valencia, D.; Ikoma, M.; Guillot, T. and Nettelmann, N. Composition and fate of short-period super-Earths. The case of CoRoT-7b. *A&A* **516**, A20 (2010).

Valencia, D.; Sasselov, D. D. and O'Connell, R. J. Detailed Models of Super-Earths: How Well Can We Infer Bulk Properties? *ApJ* **665**, 1413 (2007).

Vidal-Madjar, A.; Désert, J.-M.; Lecavelier des Etangs, A.; Hébrard, G.; Ballester, G. E.; Ehrenreich, D.; Ferlet, R.; McConnell, J. C.; Mayor, M. and Parkinson, C. D. Detection of Oxygen and Carbon in the Hydrodynamically Escaping Atmosphere of the Extrasolar Planet HD 209458b. *ApJL* **604**, L69 (2004).

Vidal-Madjar, A.; Lecavelier des Etangs, A.; Désert, J.-M.; Ballester, G. E.; Ferlet, R.; Hébrard, G. and Mayor, M. An extended upper atmosphere around the extrasolar planet HD209458b. *Nature* **422**, 143 (2003).

Watson, A. J.; Donahue, T. M. and Walker, J. C. G. The dynamics of a rapidly escaping atmosphere - Applications to the evolution of earth and Venus. *Icarus* **48**, 150 (1981).

Weiss, L. M.; Marcy, G. W.; Rowe, J. F.; Howard, A. W.; Isaacson, H.; Fortney, J. J.; Miller, N.; Demory, B.-O.; Fischer, D. A.; Adams, E. R.; Dupree, A. K.; Howell, S. B.; Kolbl, R.;

Johnson, J. A.; Horch, E. P.; Everett, M. E.; Fabrycky, D. C. and Seager, S. The Mass of KOI-94d and a Relation for Planet Radius, Mass, and Incident Flux. *ApJ* **768**, 14 (2013).

Winn, J. N.; Matthews, J. M.; Dawson, R. I.; Fabrycky, D.; Holman, M. J.; Kallinger, T.; Kuschnig, R.; Sasselov, D.; Dragomir, D.; Guenther, D. B.; Moffat, A. F. J.; Rowe, J. F.; Rucinski, S. and Weiss, W. W. A Super-Earth Transiting a Naked-eye Star. *ApJL* **737**, L18 (2011).

Wright, J. T.; Fakhouri, O.; Marcy, G. W.; Han, E.; Feng, Y.; Johnson, J. A.; Howard, A. W.; Fischer, D. A.; Valenti, J. A.; Anderson, J. and Piskunov, N. The Exoplanet Orbit Database. *PASP* **123**, 412 (2011).

Wu, Y. and Lithwick, Y. Secular Chaos and the Production of Hot Jupiters. *ApJ* **735**, 109 (2011).

Wu, Y. and Lithwick, Y. Density and Eccentricity of Kepler Planets. *ApJ* **772**, 74 (2013).

Xie, J.-W. Transit Timing Variation of Near-Resonance Planetary Pairs: Confirmation of Twelve Multiple Planet Systems. *ArXiv e-prints* (2012).

Yelle, R. V. Aeronomy of extra-solar giant planets at small orbital distances. *Icarus* **170**, 167 (2004).

Youdin, A. N. The Exoplanet Census: A General Method Applied to Kepler. *ApJ* **742**, 38 (2011).

Zahnle, K. J. and Catling, D. C. The Cosmic Shoreline. In *Lunar and Planetary Institute Science Conference Abstracts* (2013), vol. 44 of *Lunar and Planetary Institute Science Conference Abstracts*, p. 2787.

Zapolsky, H. S. and Salpeter, E. E. The Mass-Radius Relation for Cold Spheres of Low Mass. *ApJ* **158**, 809 (1969).

Appendix A

Tables

Table A.1. Minimum Masses and Densities for Selected KOI Candidates

KOI	KepMag	P (day)	F_p ($F_\oplus$)	R_p ($R_\oplus$)	$M_{p,min}$ ($M_\oplus$)	K_{min} (m s^{-1})
70.01	12.50	10.85	80.3	3.09	3.9	1.21
70.02	12.50	3.69	343.5	1.92	3.9	1.75
85.01	11.02	5.85	403.4	2.35	5.8	1.83
94.02	12.21	10.42	209.9	3.43	7.4	1.92
104.01	12.90	2.50	233.4	3.36	7.5	4.08
105.01	12.87	8.98	130.3	3.35	5.6	1.94
107.01	12.70	7.25	301.7	3.09	7.6	2.29
110.01	12.66	9.94	220.5	2.92	5.9	1.62
115.02	12.79	7.12	409.1	1.88	4.2	1.29

Table A.1 (cont'd)

KOI	KepMag	P (day)	F_p ($F_\oplus$)	R_p ($R_\oplus$)	$M_{p,min}$ ($M_\oplus$)	K_{min} (m s^{-1})
117.02	12.49	4.90	436.9	1.70	3.7	1.25
122.01	12.35	11.52	108.8	2.78	3.9	1.06
123.01	12.37	6.48	461.4	2.64	7.4	2.46
124.01	12.94	12.69	227.8	3.00	6.3	1.65
246.01	10.00	5.39	404.8	2.53	6.5	2.27
257.01	10.87	6.88	308.6	2.61	5.9	1.80
262.02	10.42	9.37	491.8	2.79	8.3	2.20
277.01	11.87	16.23	177.4	3.82	8.0	1.91
280.01	11.07	11.87	154.9	2.52	4.0	1.16

Table A.1 (cont'd)

KOI	KepMag	P (day)	$F_{\rm p}$ ($F_\oplus$)	$R_{\rm p}$ ($R_\oplus$)	$M_{\rm p,min}$ ($M_\oplus$)	$K_{\rm min}$ (m s^{-1})
281.01	11.95	19.55	192.3	3.46	7.2	1.99
285.01	11.57	13.74	180.5	3.38	6.7	1.61
288.01	11.02	10.27	433.9	3.11	9.2	2.14
291.02	12.85	8.12	247.8	2.14	3.9	1.25
295.01	12.32	5.31	339.7	1.77	3.5	1.22
297.01	12.18	5.65	482.1	1.65	3.7	1.25
301.01	12.73	6.00	399.2	1.75	3.7	1.17
323.01	12.47	5.83	166.2	2.17	3.3	1.21
984.01	11.63	4.28	259.7	3.19	7.4	2.91

Table A.1 (cont'd)

KOI	KepMag	P (day)	$F_{\rm p}$ ($F_\oplus$)	$R_{\rm p}$ ($R_\oplus$)	$M_{\rm p,min}$ ($M_\oplus$)	$K_{\rm min}$ (m s^{-1})
987.01	12.55	3.17	404.8	1.28	2.3	1.03
1117.01	12.81	11.08	327.5	2.20	4.7	1.13
1220.01	12.99	6.40	441.4	1.95	4.6	1.52
1241.02	12.44	10.50	485.3	3.84	13.3	3.17
1597.01	12.68	7.79	423.6	2.67	7.2	1.86
1692.01	12.56	5.96	175.9	2.65	4.6	1.61
1781.01	12.23	7.83	61.3	3.29	3.7	1.38
1781.02	12.23	3.00	219.6	1.94	3.2	1.63
1921.01	12.82	16.00	172.9	3.09	5.7	1.28

Table A.1 (cont'd)

KOI	KepMag	P (day)	$F_{\rm p}$ ($F_\oplus$)	$R_{\rm p}$ ($R_\oplus$)	$M_{\rm p,min}$ ($M_\oplus$)	$K_{\rm min}$ (m s^{-1})
1929.01	12.73	9.69	251.7	2.00	3.6	1.11
2067.01	12.58	13.24	347.2	2.97	7.6	1.69

Note. — Minimum masses given by equation (2.7) for KOI candidates selected for being promising targets for RV follow-up. In order to focus on promising candidates we cut the sample to planets with $K_{\rm min} > 1.0\,{\rm m\,s^{-1}}$ around stars with KepMag < 13. We only included planets with $F_{\rm p} < 500\ F_\oplus$ and $R_{\rm p} < 4\ R_\oplus$. This leaves us with 38 high-quality targets, eight of which have $K_{\rm min} > 2.0\,{\rm m\,s^{-1}}$.

Table A.2. Compositions for Transiting Planets with Measured Masses

Planet Name	Mass ($M_\oplus$)	Radius ($R_\oplus$)	H/He Envelope Fraction
Kepler-78b	$1.69\pm^{0.41}_{0.41}$	$1.20\pm^{0.09}_{0.09}$	$> 0.01\%$
Kepler-11b	$1.90\pm^{1.40}_{1.00}$	$1.80\pm^{0.03}_{0.05}$	$0.51\% \pm^{0.43\%}_{1.35\%}$
Kepler-11f	$2.00\pm^{0.80}_{0.90}$	$2.49\pm^{0.04}_{0.07}$	$2.28\% \pm^{1.20\%}_{0.62\%}$
Kepler-11c	$2.90\pm^{2.90}_{1.60}$	$2.87\pm^{0.05}_{0.06}$	$6.10\% \pm^{1.21\%}_{0.99\%}$
Kepler-79e	$4.10\pm^{1.20}_{1.10}$	$3.49\pm^{0.14}_{0.14}$	$7.99\% \pm^{1.05\%}_{1.10\%}$
Kepler-36b	$4.46\pm^{0.30}_{0.30}$	$1.48\pm^{0.03}_{0.03}$	$> 0.04\%$
Kepler-10b	$4.51\pm^{1.24}_{1.24}$	$1.41\pm^{0.03}_{0.03}$	$> 0.01\%$
Kepler-79c	$5.90\pm^{1.90}_{2.30}$	$3.72\pm^{0.08}_{0.08}$	$8.85\% \pm^{0.70\%}_{0.91\%}$
Kepler-79d	$6.00\pm^{2.10}_{1.60}$	$7.16\pm^{0.13}_{0.16}$	$36.7\% \pm^{3.56\%}_{3.43\%}$

Table A.2 (cont'd)

Planet Name	Mass ($M_\oplus$)	Radius ($R_\oplus$)	H/He Envelope Fraction
Kepler-87c	$6.40\pm^{3.20}_{3.20}$	$6.15\pm^{0.09}_{0.09}$	$34.5\% \pm^{2.24\%}_{2.49\%}$
GJ1214b	$6.46\pm^{0.99}_{0.99}$	$2.67\pm^{0.12}_{0.12}$	$3.83\% \pm^{1.30\%}_{7.13\%}$
Kepler-18b	$6.87\pm^{3.48}_{3.48}$	$2.00\pm^{0.09}_{0.09}$	$0.31\% \pm^{0.76\%}_{0.67\%}$
Kepler-11d	$7.30\pm^{0.80}_{1.50}$	$3.12\pm^{0.06}_{0.07}$	$4.57\% \pm^{1.04\%}_{1.00\%}$
CoRoT-7b	$7.42\pm^{1.21}_{1.21}$	$1.67\pm^{0.09}_{0.09}$	$> 0.03\%$
Kepler-68b	$7.59\pm^{2.06}_{2.06}$	$2.30\pm^{0.05}_{0.08}$	$0.35\% \pm^{0.38\%}_{0.82\%}$
Kepler-68b	$7.60\pm^{2.10}_{2.10}$	$2.30\pm^{0.06}_{0.09}$	$0.76\% \pm^{0.31\%}_{0.39\%}$
HD 97658b	$7.86\pm^{0.73}_{0.73}$	$2.34\pm^{0.18}_{0.15}$	$0.99\% \pm^{1.01\%}_{1.80\%}$
Kepler-11e	$8.00\pm^{1.50}_{2.10}$	$4.19\pm^{0.07}_{0.09}$	$15.0\% \pm^{1.70\%}_{1.65\%}$

Table A.2 (cont'd)

Planet Name	Mass ($M_\oplus$)	Radius ($R_\oplus$)	H/He Envelope Fraction
Kepler-36c	$8.10\pm^{0.53}_{0.53}$	$3.67\pm^{0.05}_{0.05}$	$7.80\% \pm^{1.07\%}_{1.03\%}$
55 Cnc e	$8.32\pm^{0.39}_{0.39}$	$1.99\pm^{0.08}_{0.08}$	$0.14\% \pm^{0.21\%}_{0.37\%}$
Kepler-20b	$8.45\pm^{2.12}_{2.12}$	$1.90\pm^{0.11}_{0.20}$	$> 0.28\%$
Kepler-79b	$10.9\pm^{7.40}_{6.00}$	$3.47\pm^{0.07}_{0.07}$	$6.56\% \pm^{0.74\%}_{0.98\%}$
GJ3470b	$13.9\pm^{1.63}_{1.63}$	$4.19\pm^{0.59}_{0.59}$	$12.8\% \pm^{5.15\%}_{5.00\%}$
Kepler-20c	$15.7\pm^{3.31}_{3.31}$	$3.06\pm^{0.19}_{0.30}$	$3.45\% \pm^{1.47\%}_{5.38\%}$
Kepler-18d	$16.3\pm^{1.39}_{1.39}$	$6.97\pm^{0.32}_{0.32}$	$37.5\% \pm^{3.54\%}_{3.67\%}$
Kepler-18c	$17.2\pm^{1.90}_{1.90}$	$5.48\pm^{0.25}_{0.25}$	$23.6\% \pm^{2.72\%}_{3.09\%}$
HAT-P-26b	$18.6\pm^{2.28}_{2.28}$	$6.33\pm^{0.58}_{0.58}$	$31.7\% \pm^{6.20\%}_{6.04\%}$

Table A.2 (cont'd)

Planet Name	Mass ($M_\oplus$)	Radius ($R_\oplus$)	H/He Envelope Fraction
GJ436b	$23.0\pm^{1.01}_{1.01}$	$4.22\pm^{0.09}_{0.10}$	12.0% $\pm^{1.20\%}_{2.12\%}$
Kepler-4b	$24.5\pm^{4.07}_{4.07}$	$4.00\pm^{0.21}_{0.21}$	7.70% $\pm^{1.64\%}_{2.18\%}$
HAT-P-11b	$26.2\pm^{2.86}_{2.86}$	$4.73\pm^{0.15}_{0.15}$	15.1% $\pm^{1.68\%}_{2.57\%}$
WASP-77Ab	$37.9\pm^{6.88}_{6.88}$	$13.5\pm^{0.22}_{0.22}$	100.% $\pm^{0.00\%}_{0.00\%}$
Kepler-35b	$40.3\pm^{6.35}_{6.35}$	$8.16\pm^{0.15}_{0.15}$	47.0% $\pm^{1.96\%}_{2.96\%}$
Kepler-9c	$53.5\pm^{5.52}_{5.52}$	$9.22\pm^{0.75}_{0.75}$	64.9% $\pm^{9.08\%}_{9.11\%}$
HAT-P-18b	$62.6\pm^{4.25}_{4.25}$	$11.1\pm^{0.58}_{0.58}$	87.1% $\pm^{13.3\%}_{7.12\%}$
HAT-P-12b	$66.9\pm^{4.19}_{4.19}$	$10.7\pm^{0.32}_{0.23}$	80.3% $\pm^{4.01\%}_{3.53\%}$
CoRoT-8b	$68.6\pm^{10.8}_{10.8}$	$6.38\pm^{0.22}_{0.22}$	28.6% $\pm^{2.63\%}_{6.24\%}$

Table A.2 (cont'd)

Planet Name	Mass ($M_\oplus$)	Radius ($R_\oplus$)	H/He Envelope Fraction
Kepler-34b	$69.9\pm^{3.49}_{3.17}$	$8.56\pm^{0.15}_{0.13}$	53.2% $\pm^{1.90\%}_{4.09\%}$
WASP-29b	$77.2\pm^{6.39}_{6.39}$	$8.87\pm^{0.62}_{0.39}$	60.0% $\pm^{7.57\%}_{6.07\%}$
Kepler-9b	$79.0\pm^{6.67}_{6.67}$	$9.43\pm^{0.77}_{0.77}$	62.5% $\pm^{8.58\%}_{9.51\%}$
HAT-P-38b	$85.0\pm^{6.42}_{6.42}$	$9.24\pm^{1.03}_{0.70}$	62.8% $\pm^{11.9\%}_{9.35\%}$
WASP-39b	$90.3\pm^{9.97}_{9.97}$	$14.2\pm^{0.44}_{0.44}$	100.% $\pm^{0.00\%}_{0.00\%}$
HAT-P-19b	$92.8\pm^{5.58}_{5.58}$	$12.6\pm^{0.80}_{0.80}$	100.% $\pm^{0.00\%}_{0.00\%}$
WASP-21b	$95.4\pm^{4.25}_{4.25}$	$11.9\pm^{0.67}_{0.67}$	100.% $\pm^{0.00\%}_{16.6\%}$

Table A.2 (cont'd)

Planet Name	Mass ($M_\oplus$)	Radius ($R_\oplus$)	H/He Envelope Fraction

Note. — Confirmed planets with well determined masses less than 100 $M_\oplus$ from exoplanets.org (Wright *et al.*, 2011). Here we list each planets name, mass, radius, and the fraction of its mass in a H/He envelope according to our thermal evolution models. Planets with upper limits correspond to potentially rocky planets.

Table A.3. Low Mass Planet Radii at 100 Myr, Solar Metallicity

Flux ($F_\oplus$)	Mass ($M_\oplus$)	0.1%	0.2%	0.5%	1%	2%	5%	10%	20%
0.1	1	1.21	1.32	1.65	2.17	2.75	4.32	6.81	11.7
0.1	1.5	1.30	1.40	1.71	2.15	2.65	3.97	6.18	10.6
0.1	2.4	1.42	1.53	1.79	2.17	2.58	3.66	5.36	9.05
0.1	3.6	1.54	1.64	1.89	2.21	2.56	3.49	4.93	7.86
0.1	5.5	1.69	1.79	2.01	2.28	2.60	3.37	4.58	6.96
0.1	8.5	1.85	1.95	2.14	2.39	2.67	3.36	4.35	6.32
0.1	13	2.02	2.11	2.30	2.52	2.78	3.41	4.29	5.94
0.1	20	2.20	2.29	2.47	2.67	2.93	3.52	4.32	5.75
10	1	1.31	1.44	1.82	2.40	3.06	4.72	7.13	11.1

Table A.3 (cont'd)

Flux ($F_\oplus$)	Mass ($M_\oplus$)	0.1%	0.2%	0.5%	1%	2%	5%	10%	20%
10	1.5	1.38	1.50	1.84	2.32	2.88	4.31	6.47	10.4
10	2.4	1.50	1.59	1.88	2.26	2.71	3.88	5.67	9.14
10	3.6	1.60	1.71	1.95	2.27	2.64	3.61	5.13	8.11
10	5.5	1.73	1.84	2.05	2.33	2.66	3.46	4.70	7.13
10	8.5	1.89	1.98	2.18	2.43	2.72	3.42	4.43	6.39
10	13	2.05	2.14	2.32	2.55	2.82	3.46	4.35	5.96
10	20	2.23	2.31	2.49	2.69	2.95	3.56	4.37	5.77
1000	1	1.75	1.83	2.30	3.12	3.99	6.21	8.88	11.3
1000	1.5	1.77	1.89	2.31	3.02	3.83	6.01	9.41	14.0

Table A.3 (cont'd)

Flux ($F_\oplus$)	Mass ($M_\oplus$)	0.1%	0.2%	0.5%	1%	2%	5%	10%	20%
1000	2.4	1.81	1.93	2.32	2.90	3.55	5.35	8.59	15.4
1000	3.6	1.87	1.99	2.34	2.81	3.36	4.82	7.27	13.4
1000	5.5	1.96	2.08	2.37	2.76	3.22	4.39	6.25	10.3
1000	8.5	2.08	2.19	2.50	2.76	3.15	4.12	5.56	8.48
1000	13	2.21	2.31	2.58	2.81	3.16	3.99	5.18	7.43
1000	20	2.35	2.45	2.68	2.90	3.21	3.94	4.97	6.80

Note. — Radii of planets, in $R_\oplus$. Column 1 is incident flux on the planet, relative to the solar constant. Column 2 is the total planet mass in $M_\oplus$. Otherwise, column headers indicate the fraction of a planet's mass in the H/He envelope.

Table A.4. Low Mass Planet Radii at 1 Gyr, Solar Metallicity

Flux ($F_\oplus$)	Mass ($M_\oplus$)	0.1%	0.2%	0.5%	1%	2%	5%	10%	20%
0.1	1	1.15	1.28	1.55	1.79	2.13	2.98	4.26	6.74
0.1	1.5	1.26	1.38	1.62	1.82	2.13	2.87	3.96	6.10
0.1	2.4	1.39	1.52	1.72	1.90	2.16	2.81	3.75	5.52
0.1	3.6	1.52	1.65	1.82	1.99	2.23	2.81	3.65	5.21
0.1	5.5	1.67	1.79	1.95	2.11	2.34	2.87	3.62	5.00
0.1	8.5	1.83	1.94	2.10	2.25	2.47	2.97	3.67	4.91
0.1	13	2.00	2.11	2.25	2.40	2.61	3.11	3.77	4.92
0.1	20	2.19	2.30	2.42	2.57	2.78	3.28	3.92	5.00
10	1	1.27	1.47	1.81	2.12	2.58	3.63	5.07	7.45

Table A.4 (cont'd)

Flux ($F_\oplus$)	Mass ($M_\oplus$)	0.1%	0.2%	0.5%	1%	2%	5%	10%	20%
10	1.5	1.36	1.52	1.82	2.08	2.47	3.40	4.68	6.96
10	2.4	1.48	1.63	1.86	2.08	2.41	3.18	4.26	6.24
10	3.6	1.59	1.72	1.93	2.12	2.40	3.07	4.02	5.73
10	5.5	1.72	1.85	2.02	2.19	2.45	3.04	3.86	5.34
10	8.5	1.88	1.99	2.15	2.31	2.54	3.08	3.81	5.09
10	13	2.04	2.15	2.29	2.44	2.67	3.18	3.86	5.02
10	20	2.22	2.32	2.45	2.60	2.82	3.33	3.99	5.07
1000	1	1.77	1.81	2.15	2.50	3.01	4.24	6.04	8.75
1000	1.5	1.78	1.87	2.18	2.50	2.98	4.14	5.91	9.34

Table A.4 (cont'd)

Flux ($F_\oplus$)	Mass ($M_\oplus$)	0.1%	0.2%	0.5%	1%	2%	5%	10%	20%
1000	2.4	1.82	1.93	2.21	2.50	2.91	3.93	5.50	8.76
1000	3.6	1.87	1.99	2.24	2.50	2.87	3.77	5.11	7.86
1000	5.5	1.94	2.10	2.30	2.52	2.85	3.65	4.79	7.00
1000	8.5	2.05	2.19	2.38	2.58	2.88	3.59	4.58	6.39
1000	13	2.19	2.31	2.48	2.66	2.94	3.59	4.48	6.05
1000	20	2.34	2.45	2.61	2.78	3.04	3.65	4.47	5.85

Note. — Radii of planets, in $R_\oplus$. Column 1 is incident flux on the planet, relative to the solar constant. Column 2 is the total planet mass in $M_\oplus$. Otherwise, column headers indicate the fraction of a planet's mass in the H/He envelope.

Table A.5. Low Mass Planet Radii at 10 Gyr, Solar Metallicity

Flux ($F_\oplus$)	Mass ($M_\oplus$)	0.1%	0.2%	0.5%	1%	2%	5%	10%	20%
0.1	1	1.17	1.22	1.37	1.53	1.75	2.25	2.94	4.14
0.1	1.5	1.27	1.31	1.45	1.60	1.81	2.28	2.93	4.05
0.1	2.4	1.40	1.45	1.58	1.71	1.90	2.35	2.95	3.98
0.1	3.6	1.53	1.58	1.70	1.82	2.01	2.44	3.01	3.97
0.1	5.5	1.67	1.75	1.84	1.96	2.15	2.56	3.11	4.03
0.1	8.5	1.84	1.91	2.00	2.13	2.31	2.72	3.25	4.14
0.1	13	2.00	2.09	2.17	2.30	2.48	2.90	3.44	4.31
0.1	20	2.19	2.25	2.36	2.49	2.68	3.10	3.65	4.53
10	1	1.31	1.44	1.68	1.87	2.17	2.84	3.70	5.11

Table A.5 (cont'd)

Flux ($F_\oplus$)	Mass ($M_\oplus$)	0.1%	0.2%	0.5%	1%	2%	5%	10%	20%
10	1.5	1.40	1.49	1.72	1.90	2.19	2.83	3.66	5.03
10	2.4	1.51	1.60	1.78	1.96	2.21	2.80	3.58	4.89
10	3.6	1.62	1.73	1.87	2.03	2.27	2.81	3.53	4.75
10	5.5	1.75	1.85	1.98	2.13	2.35	2.86	3.52	4.64
10	8.5	1.90	1.98	2.11	2.25	2.47	2.95	3.58	4.61
10	13	2.05	2.13	2.26	2.40	2.61	3.07	3.68	4.66
10	20	2.23	2.32	2.43	2.56	2.77	3.23	3.83	4.77
1000	1	1.96	2.01	2.08	2.18	2.31	2.70	3.49	4.88
1000	1.5	1.94	1.99	2.08	2.17	2.33	2.91	3.76	5.36

Table A.5 (cont'd)

Flux ($F_\oplus$)	Mass ($M_\oplus$)	0.1%	0.2%	0.5%	1%	2%	5%	10%	20%
1000	2.4	1.95	2.00	2.08	2.22	2.49	3.10	3.94	5.55
1000	3.6	1.98	2.03	2.12	2.30	2.58	3.20	4.03	5.54
1000	5.5	2.04	2.10	2.21	2.38	2.64	3.26	4.08	5.49
1000	8.5	2.12	2.19	2.31	2.48	2.73	3.31	4.10	5.44
1000	13	2.23	2.34	2.43	2.59	2.83	3.38	4.13	5.40
1000	20	2.36	2.47	2.57	2.72	2.95	3.49	4.20	5.38

Note. — Radii of planets, in $R_\oplus$. Column 1 is incident flux on the planet, relative to the solar constant. Column 2 is the total planet mass in $M_\oplus$. Otherwise, column headers indicate the fraction of a planet's mass in the H/He envelope.

Table A.6. Low Mass Planet Radii at 100 Myr, Enhanced Opacity

Flux ($F_\oplus$)	Mass ($M_\oplus$)	0.1%	0.2%	0.5%	1%	2%	5%	10%	20%
0.1	1	1.24	1.43	1.89	2.57	3.00	4.32	6.81	11.7
0.1	1.5	1.31	1.47	1.93	2.58	3.17	3.97	6.18	10.6
0.1	2.4	1.44	1.60	2.14	2.51	3.11	4.30	5.36	9.05
0.1	3.6	1.57	1.71	2.18	2.51	3.02	4.31	5.57	7.86
0.1	5.5	1.72	1.84	2.23	2.53	2.97	4.09	5.69	7.25
0.1	8.5	1.87	2.00	2.33	2.57	2.95	3.90	5.29	7.73
0.1	13	2.04	2.16	2.45	2.67	3.00	3.81	4.99	7.25
0.1	20	2.23	2.33	2.58	2.79	3.10	3.82	4.82	6.68
10	1	1.35	1.53	2.05	2.79	3.12	4.72	7.13	11.1

Table A.6 (cont'd)

Flux ($F_\oplus$)	Mass ($M_\oplus$)	0.1%	0.2%	0.5%	1%	2%	5%	10%	20%
10	1.5	1.41	1.58	2.07	2.80	3.41	4.31	6.47	10.4
10	2.4	1.51	1.68	2.25	2.67	3.32	4.50	5.67	9.14
10	3.6	1.64	1.77	2.26	2.62	3.17	4.55	5.71	8.11
10	5.5	1.77	1.89	2.30	2.60	3.07	4.27	5.94	7.30
10	8.5	1.92	2.04	2.37	2.63	3.01	4.01	5.50	7.98
10	13	2.08	2.19	2.48	2.70	3.04	3.88	5.12	7.50
10	20	2.25	2.35	2.61	2.82	3.13	3.87	4.90	6.81
1000	1	1.75	1.88	2.42	3.13	3.99	6.21	8.88	11.3
1000	1.5	1.77	1.90	2.46	3.25	3.84	6.01	9.41	14.0

Table A.6 (cont'd)

Flux ($F_\oplus$)	Mass ($M_\oplus$)	0.1%	0.2%	0.5%	1%	2%	5%	10%	20%
1000	2.4	1.81	1.97	2.63	3.13	3.89	5.35	8.59	15.4
1000	3.6	1.87	2.02	2.57	3.01	3.67	5.23	7.27	13.4
1000	5.5	1.96	2.10	2.54	2.90	3.46	4.89	6.68	10.3
1000	8.5	2.08	2.21	2.56	2.86	3.31	4.48	6.23	8.82
1000	13	2.21	2.32	2.63	2.89	3.27	4.22	5.64	8.36
1000	20	2.36	2.47	2.73	2.95	3.30	4.12	5.28	7.38

Note. — Radii of planets, in $R_\oplus$. Column 1 is incident flux on the planet, relative to the solar constant. Column 2 is the total planet mass in $M_\oplus$. Otherwise, column headers indicate the fraction of a planet's mass in the H/He envelope.

Table A.7. Low Mass Planet Radii at 1 Gyr, Enhanced Opacity

Flux ($F_\oplus$)	Mass ($M_\oplus$)	0.1%	0.2%	0.5%	1%	2%	5%	10%	20%
0.1	1	1.15	1.37	1.68	1.98	2.43	3.11	4.26	6.74
0.1	1.5	1.26	1.45	1.74	1.99	2.38	3.27	3.96	6.10
0.1	2.4	1.39	1.60	1.82	2.05	2.38	3.22	4.23	5.52
0.1	3.6	1.52	1.71	1.90	2.10	2.42	3.15	4.25	5.62
0.1	5.5	1.67	1.85	2.02	2.19	2.47	3.16	4.13	5.84
0.1	8.5	1.84	1.99	2.15	2.32	2.57	3.19	4.09	5.74
0.1	13	2.01	2.15	2.30	2.46	2.70	3.28	4.11	5.58
0.1	20	2.21	2.32	2.46	2.62	2.86	3.42	4.17	5.56
10	1	1.27	1.50	1.84	2.20	2.72	3.63	5.07	7.45

Table A.7 (cont'd)

Flux ($F_\oplus$)	Mass ($M_\oplus$)	0.1%	0.2%	0.5%	1%	2%	5%	10%	20%
10	1.5	1.36	1.56	1.87	2.16	2.60	3.58	4.68	6.96
10	2.4	1.48	1.68	1.92	2.17	2.54	3.47	4.52	6.24
10	3.6	1.59	1.77	1.98	2.20	2.54	3.34	4.53	5.85
10	5.5	1.72	1.90	2.07	2.27	2.56	3.31	4.36	6.14
10	8.5	1.89	2.03	2.20	2.37	2.64	3.31	4.27	5.99
10	13	2.05	2.18	2.34	2.50	2.76	3.37	4.24	5.76
10	20	2.24	2.36	2.49	2.65	2.90	3.49	4.27	5.68
1000	1	1.77	1.85	2.20	2.60	3.09	4.24	6.04	8.75
1000	1.5	1.78	1.88	2.24	2.59	3.10	4.14	5.91	9.34

Table A.7 (cont'd)

Flux ($F_\oplus$)	Mass ($M_\oplus$)	0.1%	0.2%	0.5%	1%	2%	5%	10%	20%
1000	2.4	1.82	1.96	2.26	2.57	3.02	4.13	5.50	8.76
1000	3.6	1.87	2.02	2.27	2.54	2.96	3.94	5.34	7.86
1000	5.5	1.94	2.11	2.32	2.54	2.90	3.80	5.05	7.13
1000	8.5	2.05	2.21	2.39	2.59	2.90	3.68	4.81	6.84
1000	13	2.19	2.32	2.49	2.67	2.96	3.65	4.65	6.41
1000	20	2.34	2.46	2.61	2.78	3.06	3.70	4.57	6.14

Note. — Radii of planets, in $R_\oplus$. Column 1 is incident flux on the planet, relative to the solar constant. Column 2 is the total planet mass in $M_\oplus$. Otherwise, column headers indicate the fraction of a planet's mass in the H/He envelope.

Table A.8. Low Mass Planet Radii at 10 Gyr, Enhanced Opacity

Flux ($F_\oplus$)	Mass ($M_\oplus$)	0.1%	0.2%	0.5%	1%	2%	5%	10%	20%
0.1	1	1.17	1.24	1.37	1.53	1.75	2.32	2.97	4.14
0.1	1.5	1.27	1.34	1.46	1.61	1.82	2.33	3.04	4.05
0.1	2.4	1.40	1.47	1.57	1.71	1.92	2.40	3.07	4.13
0.1	3.6	1.53	1.59	1.70	1.83	2.01	2.49	3.12	4.23
0.1	5.5	1.67	1.76	1.85	1.97	2.16	2.59	3.22	4.27
0.1	8.5	1.84	1.88	2.02	2.14	2.32	2.75	3.34	4.37
0.1	13	2.00	2.10	2.18	2.30	2.50	2.93	3.50	4.51
0.1	20	2.19	2.27	2.37	2.49	2.69	3.13	3.71	4.66
10	1	1.31	1.39	1.55	1.75	2.02	2.72	3.70	5.11

Table A.8 (cont'd)

Flux ($F_\oplus$)	Mass ($M_\oplus$)	0.1%	0.2%	0.5%	1%	2%	5%	10%	20%
10	1.5	1.40	1.48	1.62	1.79	2.05	2.66	3.57	5.03
10	2.4	1.51	1.58	1.70	1.85	2.10	2.65	3.44	4.89
10	3.6	1.62	1.69	1.80	1.94	2.15	2.69	3.41	4.67
10	5.5	1.75	1.84	1.93	2.07	2.27	2.75	3.44	4.61
10	8.5	1.90	1.98	2.08	2.21	2.41	2.86	3.51	4.62
10	13	2.05	2.14	2.23	2.36	2.56	3.02	3.63	4.70
10	20	2.23	2.31	2.41	2.54	2.74	3.21	3.81	4.81
1000	1	1.96	2.01	2.08	2.16	2.29	2.60	3.49	4.88
1000	1.5	1.94	1.99	2.05	2.15	2.28	2.83	3.72	5.36

Table A.8 (cont'd)

Flux ($F_\oplus$)	Mass ($M_\oplus$)	0.1%	0.2%	0.5%	1%	2%	5%	10%	20%
1000	2.4	1.95	1.99	2.05	2.14	2.36	3.01	3.89	5.55
1000	3.6	1.98	2.02	2.09	2.18	2.42	3.10	3.97	5.48
1000	5.5	2.04	2.09	2.15	2.31	2.54	3.14	4.01	5.47
1000	8.5	2.12	2.15	2.28	2.43	2.67	3.21	4.01	5.40
1000	13	2.23	2.28	2.40	2.55	2.79	3.33	4.05	5.35
1000	20	2.36	2.45	2.55	2.69	2.92	3.45	4.15	5.32

Note. — Radii of planets, in $R_\oplus$. Column 1 is incident flux on the planet, relative to the solar constant. Column 2 is the total planet mass in $M_\oplus$. Otherwise, column headers indicate the fraction of a planet's mass in the H/He envelope.